11-10-2010

Voltage Stability Impact of Grid-Tied Photovoltaic Systems Utilizing Dynamic Reactive Power Control

Adedamola Omole
University of South Florida

Voltage Stability Impact of Grid-Tied Photovoltaic Systems

Utilizing Dynamic Reactive Power Control

by

Adedamola Omole

A dissertation submitted in partial fulfillment
of the requirements for the degree of
Doctor of Philosophy
Department of Electrical Engineering
College of Engineering
University of South Florida

Major Professor: Alex Domijan, Ph.D.
Sanjukta Bhanja, Ph.D.
Lingling Fan, Ph.D.
Jim Mihelcic, Ph.D.
Tom Crisman, Ph.D.

Date of Approval:
November 10, 2010

Keywords: Renewable Energy, Smart Grid, Bifurcation, Decentralization, Voltage Sag

ACKNOWLEDGMENTS

I would like to take this opportunity to thank my supervisor Dr. Alex Domijan for his valuable guidance and support throughout my doctoral program. I would like to thank my committee members, Dr. Sanjukta Bhanja, Dr. Lingling Fan, Dr. Jim Mihelcic and Dr. Tom Crisman for their generous advice and interest.

I would also like to thank the academic and administrative staff in the Department of Electrical Engineering and the wonderful people at the Power Center for Utility Explorations (PCUE).

Finally, I would like to thank my mom and dad for supporting me in countless ways every step of the way; my older sister and her family for their prayers and comfort over oceans; my little sister for her invaluable advice and perspective; and the relatives and friends who made this a wonderfully gratifying experience.

TABLE OF CONTENTS

LIST OF TABLES

LIST OF FIGURES

ABSTRACT

Photovoltaic (PV) DGs can be optimized to provide reactive power support to the grid, although this feature is currently rarely utilized as most DG systems are designed to operate with unity power factor and supply real power only to the grid. In this work, the voltage stability of a power system embedded with PV DG is examined in the context of the high reactive power requirement after a voltage sag or fault. A real-time dynamic multi-function power controller that enables renewable source PV DGs to provide the reactive power support necessary to maintain the voltage stability of the microgrid, and consequently, the wider power system is proposed.

The loadability limit necessary to maintain the voltage stability of an interconnected microgrid is determined by using bifurcation analysis to test for the singularity of the network Jacobian and load differential equations with and without the contribution of the DG. The maximum and minimum real and reactive power support permissible from the DG is obtained from the loadability limit and used as the limiting factors in controlling the real and reactive power contribution from the PV source. The designed controller regulates the voltage output based on instantaneous power theory at the point-of-common coupling (PCC) while the reactive power supply is controlled by means of the power factor and reactive current droop method. The control method is implemented in a modified IEEE 13-bus test feeder system using PSCAD® power system

analysis software and is applied to the model of a Tampa Electric® PV installation at Lowry Park Zoo in Tampa, FL.

This dissertation accomplishes the systematic analysis of the voltage impact of a PV DG-embedded power distribution system. The method employed in this work bases the contribution of the PV resource on the voltage stability margins of the microgrid rather than the commonly used loss-of-load probability (LOLP) and effective load-carrying capability (ELCC) measures. The results of the proposed method show good improvement in the before-, during-, and post-start voltage levels at the motor terminals. The voltage stability margin approach provides the utility a more useful measure in sizing and locating PV resources to support the overall power system stability in an emerging smart grid.

1. INTRODUCTION

The current electric grid is designed mainly to operate in a radial manner, with big centralized power stations supplying power over long distances to distribution networks. However, it is undergoing dramatic evolution as smaller decentralized generators are gradually being added to the power distribution system. Over the last few decades, and particularly in the 2000's, renewable energy has constituted a large part of that new distributed generation. Renewable energy sources such as solar, wind, biomass, hydro and fuel cell have shown great potential for viable utilization in distributed generation systems [1]. The production of power from renewable energies is both desirable and beneficial as it provides a sustainable alternative that significantly reduces the rate of environmental pollution in comparison with production from fossil fuels.

Traditionally, utilities have had to build new power stations in order to sufficiently meet peak demand. Utilities are required to have enough installed capacity to supply the maximum load demand at all times in order to forestall power system instabilities, such as voltage collapse, but the demand often exhibits severe fluctuations within the day and over the course of a year. In areas with warm weather, peak demand is usually much higher during the summer than during the winter due to the use of air

conditioning equipment [2]. Thus, a utility that has the required capacity to meet peak demand during the summer will operate with much less efficiency, as a result of idle capacity, during the winter. Also, the demand in the morning of a hot summer day is much less than the demand at noon and in the evening [3] and the utility is forced to operate inefficiently during the early and late hours of the day.

Photovoltaic microgrids are increasingly being integrated into the power distribution network, and they are well suited to augment the power supply during peak load demand, particularly in areas with warm weather, since the peak demand during the summer normally coincides with periods of high solar incidence [4]. The utility is therefore able to augment grid supply by generating pollution-free and comparatively cheaper electricity during the period of the day when electricity consumption costs are highest. However, the photovoltaic array experiences large variations in its power output depending on weather conditions [4, 5] and in the case where the PV-based microgrid is connected to the main grid, it may cause improper operation of the grid [5]. Some of the issues include voltage regulation, frequency deviation, and unintentional islanding. In particular, overvoltage at the point of common coupling (PCC) between the PV-microgrid and main grid can result in the PV resource being taken offline at critical times [6, 7, 8]. Therefore, the PV-based microgrid must be designed so as to always operate within acceptable voltage limits and ensure that it does not have a detrimental effect on grid operation. Additionally, the PV-microgrid can be used to enhance the voltage stability and reliability of the power system by operating it in a non-traditional manner to provide dynamic reactive power compensation to the grid.

This work examines the effect of the increasing rate of DG penetration on the power system voltage stability. The impact of the microgrid on the power system voltage stability at the PCC between the microgrid and the utility supply is investigated using models of the various power system components. Based on the simulation results, a method to determine the proximity of DG microgrids to voltage instability using bifurcation theory is presented and a real-time dynamic reactive power controller that operates the PV DG to supply reactive power to support the grid voltage is proposed. The controller reconfigures the PV resource to rapidly supply the reactive power deficit, within capacity limits, that is necessary to maintain the voltage at the PCC within acceptable limits. The operation of PV-based microgrids in this manner will significantly enhance the adoption of renewable DG resources into the power distribution system and can offer several advantages over the current modes of operation since the utility is able to keep renewable energy resources online during peak demand and utilize its reactive power capability to maintain the system voltage stability.

1.1 Overview of Alternative Energy Distributed Generation Systems

The primary source of energy for the majority of current electric power systems are fossil fuels such as crude oil and coal. These non-renewable forms of energy are ultimately finite sources of energy that cannot be deemed sustainable in the long term, while they can also be quite harmful to the environment through the burning of oil and coal in the process of conversion to electricity. Over the past few decades there has

been a lot of interest in alternative sources of energy and several approaches have been suggested to upgrade and replace existing energy sources. Renewable energy sources like solar and wind have shown remarkable promise as possible environmentally-friendly and cost efficient alternatives to fossil fuels for use in distributed generation [1].

Distributed power generation includes the application of small-to-medium size generators, generally less than 15MW, scattered across a power system to supply electrical power needed by customers. When generating stations are located far away from the consumer, power has to be transmitted over long distances and there are usually non-negligible associated power losses as a result of the transmission and distribution of the electric power. By locating generating stations close to consumers, distributed generation provides advantages in efficiency and flexibility over traditional large-scale, capital-intensive centralized power plants.

Apart from the adverse environmental effects of current fossil fuel-based power supply, the finite global supply of recoverable fossil fuels implies that at some point in the future, alternative sources of energy will become the primary source of energy to meet global demand. Solar and wind power represent promising alternatives that will likely initially supplement fossil fuel based energy supply, and eventually replace the fossil fuel energy sources as the availability of the latter declines. When compared to fossil fuels, solar power is a relatively untapped source of energy [9], thus there still remains a lot of work to be done to make solar power as efficient and reliable as possible.

1.2 Power System Voltage Stability

The power system voltage stability is affected by the ability of generating sources to supply sufficient real and reactive power to the loads. The primary responsibility of utilities is to supply electric power to the consumer, but the electrical load profile of the consumer can vary greatly over the course of the day, throughout the week and from season to season. Thus, in order for the utility to meet the consumers energy requirement at all times, and avoid load shedding, the utility is forced to invest scarce resources into increasing the generating capacity to meet the highest electrical load demand expected throughout the year. This peak demand may only occur for a few hours each day and for a few months over the entire year but the utility must be prepared to meet this demand should it occur. Recent cases of voltage collapse and similar power system instabilities have been linked to imbalances between the load demand and power supply [10, 11, 12].

In sunny regions, the peak demand can be expected during the mid-afternoon of summer months as a result of air conditioning use during the day [2]. During the winter, the peak demand is much less than during the summer causing the utility to be saddled with idle capacity and to operate inefficiently for extended periods. Some utilities have adopted tiered-pricing policies to offset the huge investment outlay required to build peaker plants [2, 13], but this approach negatively impacts the customer. A solution that is gaining more prominence, as a result of government incentives and advances in technology, is the use of photovoltaic microgrids as peaker plants [13]. Photovoltaic

power plants are suitable for use as peaker plants, especially in sunny regions, since the peak power output of the PV coincides with the peak load demand during summer. The challenge is to mitigate the impact of the fluctuating nature of the PV source on the power system stability and utilize the potential of distributed resources to enhance the overall system reliability.

1.3 Research Objectives

The research presented in this work has been performed as part of a pilot project supported by the Power Center for Utility Explorations (PCUE) at the University of South Florida (USF) and Tampa Electric Company (TECO) to study the impact of connecting PV microgrids to the power distribution system. This research focuses on addressing the challenges in utilizing PV microgrids to provide reactive power support to the grid as a result of the fluctuating nature of the energy source and the impact the 'missing' capacity has on the power system stability when the solar resource is unavailable. The project involves implementing multiple small-to-medium size (15 kW – 150 kW) size PV DG as peaker plants at various points in the power distribution system to supplement grid supply during peak demand. Furthermore, the project aims to address research activities related to IEEE 1547 standards including grid/DG monitoring and control, understanding voltage regulation and stability, and establishing a basis for renewable DG penetration and aggregation.

The objectives of this research are thus –

- To study and implement various power system components using Matlab/Simulink and PSCAD software.
- To investigate the influence of interconnected renewable source microgrids on power system voltage stability.
- To investigate the impact the shift in bifurcation point of a PV-based industrial microgrid, having mainly induction motor loads, has on the short- and long-term voltage stability of the power system.
- To investigate the impact of implementing PV microgrids reconfigured with real-time dynamic reactive power controllers on the power system stability.

1.4 Contribution of the Dissertation

This research is unique as it examines the impact of operating DGs with fluctuating power sources on the power system voltage stability, in the case where there is a significant penetration of DGs that are dynamically controlled to independently supply active and reactive power to the grid to maintain the local area voltage during peak demand. The modeling, simulations and analysis are performed using a combination of power system tools including Matlab/Simulink™, PSCAD™, and EDSA™. The main contributions of the dissertation are summarized as follows:

- Standard mathematical models of various power system components, including PV source, inverter module, induction motor and synchronous generator have been studied. The studied models are initially implemented in Matlab/Simulink to understand the mathematical basis of operation, then in PSCAD software to observe the transient response of the models.
- The implemented PSCAD models of the various power system components have been integrated to investigate the contributing effect of fluctuating power sources to momentary interruptions that adversely affect equipment and the voltage stability of an interconnected grid.
- The loadability limit necessary to forestall voltage instability in grid-connected microgrids has been determined using bifurcation analysis.
- A method to reconfigure grid-tied renewable energy sources to mitigate voltage sags using a real-time dynamic reactive power control has been developed.

1.5 Publications

A. Omole, "Analysis, modeling, and simulation of optimal power tracking of multiple-modules of paralleled solar cell systems," *Thesis submitted to Electrical Engineering Dept.,* Florida State University, Tallahassee, August 2006.

A. Domijan, A. Islam, M. Islam, A. Antonio, A. Omole, H. Algarra, "Price-responsive customer screening using load curve with inverted price-tier," *International Journal of Power & Energy Systems,* Accepted for publication July 2010.

1.6 Outline of Dissertation

This dissertation consists of seven chapters, with the first chapter introducing the current applications of interconnected renewable DG systems as well as the challenges associated with the rapid penetration and deployment of DG resources. The motivation for conducting this research and the goals of the study are discussed. The first chapter also gives an overview of the impact of peak load demand on the power system stability and highlights ongoing research activities related to DG penetration.

Chapter 2 presents the literature review on the voltage stability of a microgrid-embedded power system including the impact the operating characteristic of the PV source has on the power system voltage stability. The effect of momentary interruptions and voltage sags on the power system stability and reliability is also examined, while the various methods currently used to mitigate voltage sags are reviewed.

Chapter 3 identifies the reasons for the static and dynamic voltage instability of the power system. Standard mathematical models of various power system components, including the synchronous generator and PV source, are described and implemented in Matlab/Simulink. The models are used to investigate the impact of typical grid-

connected PV sources on the local voltage regulation and power system reliability. Based on the simulation results, remedial action to prevent overvoltages and unintentional islanding are explored and presented.

Chapter 4 presents an analytical approach to determine the voltage stability limits of an interconnected microgrid. The mathematical models of the short- and long-term dynamics of the generator and load are used to determine the power system load equilibrium point. Bifurcation theory is then applied to find the singularity point of the network Jacobian that leads to voltage instability, and Matlab/Simulink simulations are used to evaluate the minimum margin between the load equilibrium point and the loadability limit. The margin which prevents the stalling of motors during disturbances is used to determine the size and suitability of DGs in the power distribution system. Remedial action to restore the load equilibrium point when a power system exceeds the loadability limit is also explored.

In Chapter 5, the voltage impact of operating PV-based microgrids to independently supply active/reactive power during peak demand is examined. A real-time dynamic reactive power controller (DRPC) that regulates the output voltage of the PV DG and controls the reactive power flow using instantaneous power theory and a “voltage vs. reactive current droop” control method is proposed and implemented in PSCAD. The impact of the controller implementation on grid voltage stability is analyzed and the grid overvoltage protection function is demonstrated.

Chapter 6 presents a case study for a peak load shaving PV system in Tampa, FL (USA). The environmental data and load characteristics of the site are provided, as is the electrical components data. Slight modifications are made to the distribution network of the study site to approximate it to the IEEE 13-bus test feeder system used for power flow analysis. The study system is implemented in EDSA to investigate the steady-state power flow and the effect of source and load variations on the long-term voltage stability of the PV microgrid. Based on the investigations, the sizing and location of PV microgrids as a function of the maximum load demand at the PCC bus is proposed.

The final chapter concludes the dissertation with a look on the future development of this work. The references and appendices are attached at the end of the dissertation.

2. LITERATURE REVIEW

The structure of the power system is undergoing a paradigm shift as DG and other forms of renewable energy are added to the grid. The aim is to optimize the efficiency of the emerging power system. This has led to the term “smart grid” being used to describe the scenario where the power system is completely addressable and the power flow can be efficiently managed between central generators, microgrids, DGs and loads at the distribution level. The configuration of the emerging microgrid-embedded power system is reviewed at the beginning of this chapter. An emphasis is placed on photovoltaic DGs and how the fluctuating nature of the output can adversely affect power system stability. Momentary interruptions and voltage sags, both major causes of power system voltage instability, are described and the cost to industry of these forms of power system instability is presented. The various methods that have been employed to minimize the occurrence of voltage sags and momentary interruptions are discussed while noting there has only been a minimal effort to employ photovoltaic DGs for voltage stability enhancement.

2.1 Microgrid-Embedded Power Distribution System

The power system can experience many problems when DGs are added to the existing distribution network, mainly because the existing power system was designed to operate in a radial manner where the power flow is unidirectional, i.e., big centralized generating plants supplying power to loads downstream through long transmission lines as shown in Fig. 2.1. The power grid as it is currently designed is still able to function properly when small amounts of DGs are added to the system, but there is a limit to the amount of new DGs that can be added to the grid before it is necessary to modify or change some of the existing power system equipment and protection. Without proper design and planning, the implementation of DGs in the distribution network will likely lead to power quality problems, degradation in system reliability, reduced efficiency, overvoltages and other safety issues [14].

The addition of DGs to the grid often results in bidirectional power flow, which can cause problems on the existing grid configuration. So, although the application of interconnected DGs across the power distribution system can have many positive effects, such as grid reliability improvement through backup generation, voltage support, as well as reducing the power losses associated with transmitting power over long distances, it also complicates the protection schemes and associated control equipment. For instance, the addition of DGs can adversely impact on the power quality due to poor voltage regulation, voltage flickers, and introducing harmonics into the power system [15]. Similarly, the reliability of the power system may be degraded if the

DGs are not properly coordinated with the power system protection. As a result, it is critical to assess such impacts prior to deploying DG infrastructure in order to avoid lowering the system reliability and the consequent degradation of service.

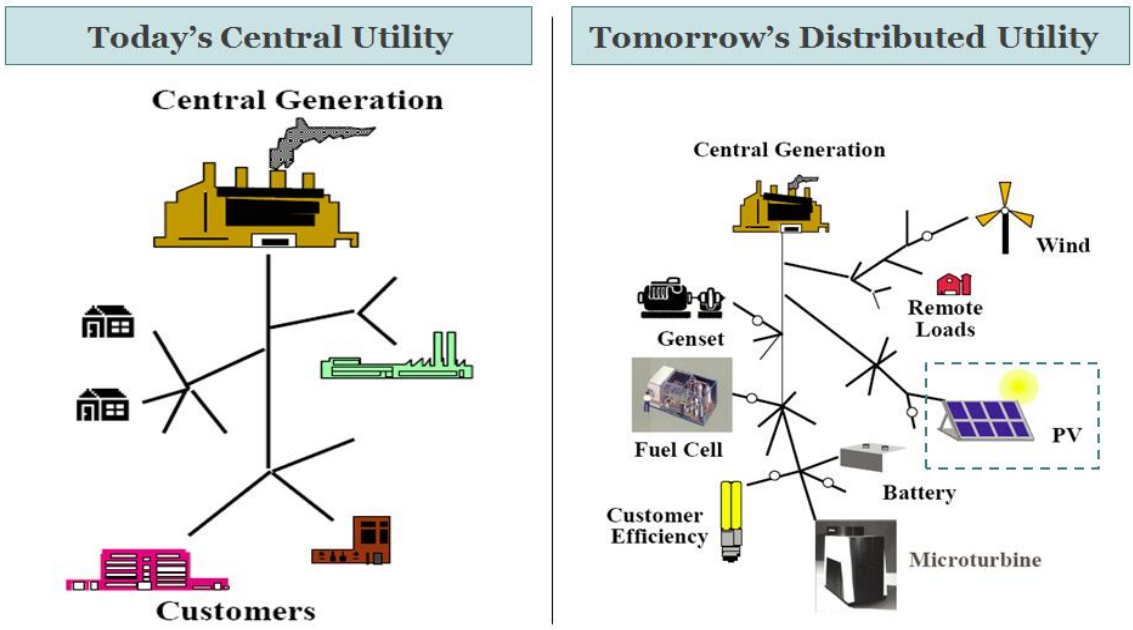

Fig. 2.1 Central vs. distributed generation power system

To address the challenges associated with DG integration, standards for interconnecting distributed resources (DR) with the grid were established in 2003. The IEEE 1547 (2003) Interconnection Standard was established to provide interconnection technical specifications and requirements of connecting DGs to the power system [16]. The IEEE 1547 Std. does not directly address the specific energy sources used for DGs but it is important to address the impact of adding DGs with fluctuating sources such as solar and wind to the power distribution system. In the case of solar generation, the addition of a photovoltaic DG to the grid increases the voltage at the point-of-common coupling

(PCC) between the DG and the utility grid [17, 18]. The increase in voltage can rise to unacceptable levels if the maximum power generation of the PV coincides with light load demand on the grid. This can lead to power system instability or cause damage to downstream equipment. The addition of PV DGs to the grid influences the grid voltage during normal (steady-state) operation and the voltage response during abnormal (transient) operation [18, 19, 20].

2.2 Photovoltaic Energy Systems

The peak output of PV systems in sunny regions often coincides with the peak load demand during the summer time, mainly as a result of A/C use. The hourly average PV output and the hourly average temperature for a PV system located at USF, St. Pete is shown in Figs. 2.2a and 2.2b. The solar radiation-dependent PV output profile closely matches the temperature profile, and considering that the energy consumed by HVAC systems can be up to 40% of the total energy use [21], effectively harnessing solar energy during peak load demand can be of great environmental and economic benefit.

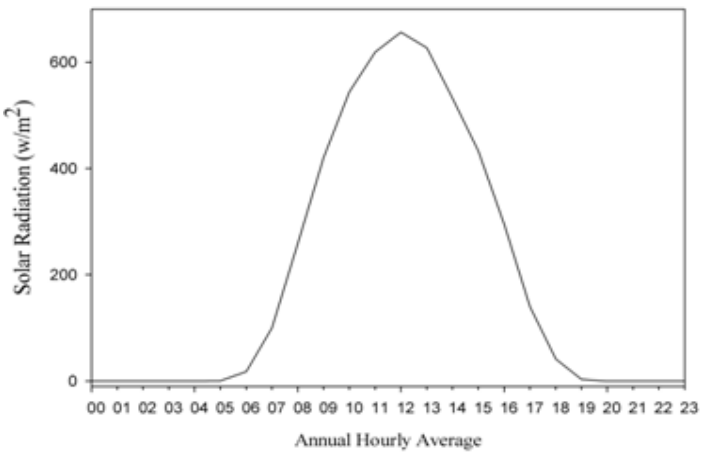

Fig. 2.2a Annual hourly average solar radiation at USF, St. Pete

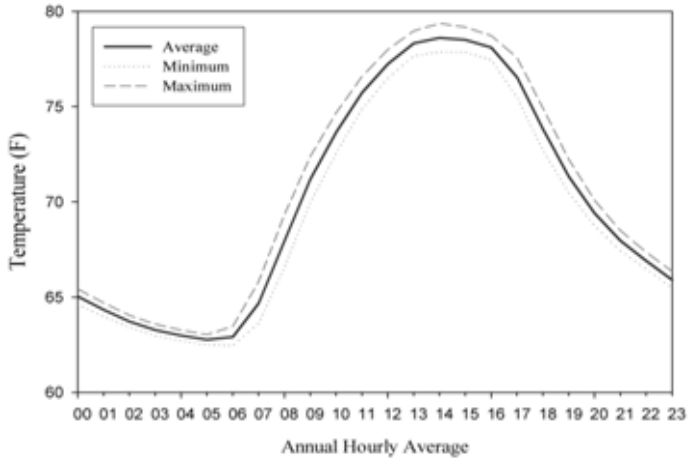

Fig. 2.2b Annual hourly average temperature at USF, St. Pete

The main component of the photovoltaic (PV) system is the solar panels that generate electric power by the direct conversion of the sun's energy into electricity. The solar panels are mostly made with semiconductor material, with Silicon (Si) being widely used. More recently other materials such as Aluminum (Al) and Gallium (Ga) with better conversion properties are increasingly being used [22, 23]. The balance of components

of the PV system includes the electronic devices that interface the PV output and the AC or DC loads.

A major challenge in utilizing solar cells for power generation is improving cell efficiency and optimizing energy extraction. The solar cell is able to generate the maximum power at a specific operating point, but that operating point varies depending on the ambient conditions. This varying output effect limits the ability of utilities to predict the expected power output at a given time for that location and thus schedule their generation accordingly. The I-V (current-to-voltage) characteristic of the solar cell is used to determine the operating point at which the cell generates the maximum power.

The solar cell is made of a p-n junction fabricated in a thin layer of semiconductor. The amount of sunlight energy, referred to as photons, absorbed by the semi-conductor material determines the output power of the solar cell. The output power is dependent on the highly non-linear current-voltage characteristic of the semi-conductor material shown in Fig. 2.3. The maximum power point (MPP) where the solar cell outputs the most power can be determined from the I-V curve. The MPP power is determined by calculating the product of the voltage and output current. The solar cell is typically operated at or very close to the MPP in order to obtain the most power. This point is located around the 'bend' or 'knee' of the I-V characteristic as shown at point A in Fig. 2.3.

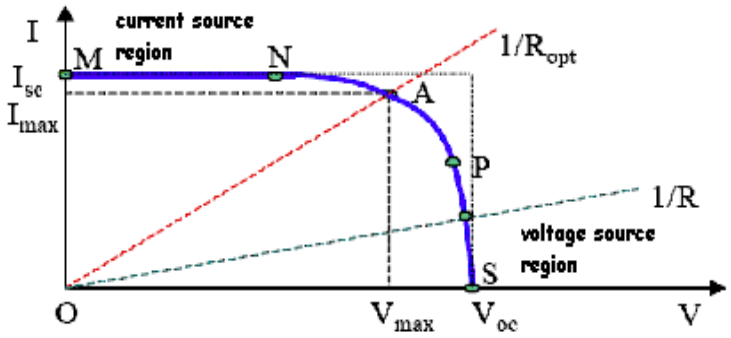

Fig. 2.3 Typical I-V characteristic of a solar cell in steady-state operation [24]

The operating characteristic of a solar cell has two distinct regions: the current source region and the voltage source region. The solar cell has high internal impedance in the current source region while the internal impedance is low in the voltage source region. The output current remains almost constant as the terminal voltage varies in the current source region, while the terminal voltage varies only minimally over a wide range of output current in the voltage source region.

According to the maximum power transfer theory, the power delivered to the load is maximum when the source internal impedance matches the load impedance [25]. The solar cell is operated at the MPP by matching the internal impedance of the solar cell to the input impedance of the load. The internal impedance of the solar cell is a function of the cell voltage and current, and so the maximum power operating point can be maintained by controlling either the output voltage or current or both. However, maintaining the operating point at the MPP becomes unpredictable as constantly changing ambient conditions such as irradiance and temperature vary the maximum

operating point and thus the output power. Generating the maximum power becomes a task of tracking the MPP taking into account the varying ambient conditions. A maximum power point tracker (MPPT) is used to accomplish the task. Most MPPT controllers are based on the buck converter (step-down), boost converter (step-up) or Cuk converter (buck-boost) setup [26].

Two significant factors that affect the output power of the solar cell are irradiation and temperature. Irradiance is a characteristic related to sun radiation, and under ideal conditions is measured as 1000 W/m^2 at the equator. The I-V characteristic of a solar cell including the effects of irradiance is shown in Fig. 2.4. The irradiance at any location is strongly dependent on the orientation and inclination angles of the solar panel. Orientation is usually measured relative to the south in northern latitudes and vice versa while the inclination angle is measured relative to the horizontal. Using these two parameters, the irradiation at any location can be determined from data that is widely available for many sites globally.

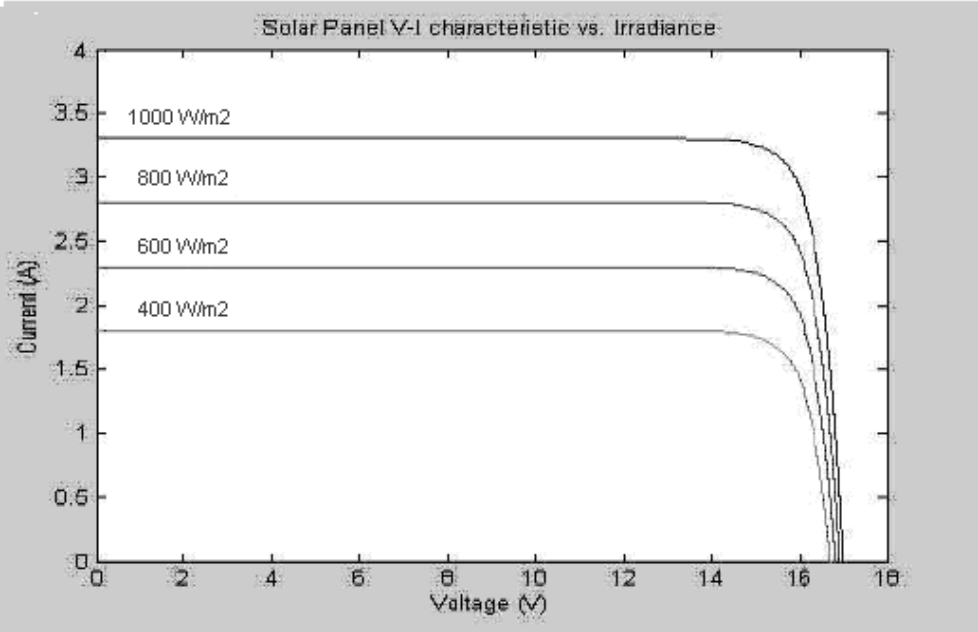

Fig. 2.4 Typical solar cell I-V characteristic showing effect of irradiance [24]

Fig. 2.4 shows that the output power is directly proportional to the irradiance. However, it is only the output current that is affected by the irradiance. This makes sense since by the principle of operation of the solar cell the generated current is proportional to the flux of photons [27]. The flux of photons is greater when the sun is bright and the light intensity is high, therefore more current is generated as the light intensity increases. The change in voltage is minimal with varying irradiance, and for most practical applications, the change is considered negligible [28].

Temperature also has a significant effect on the output power of the solar module. Whereas the irradiance mainly affects the output current, the temperature mainly affects the terminal voltage. A plot of I-V characteristic with varying temperature is shown in Fig. 2.5.

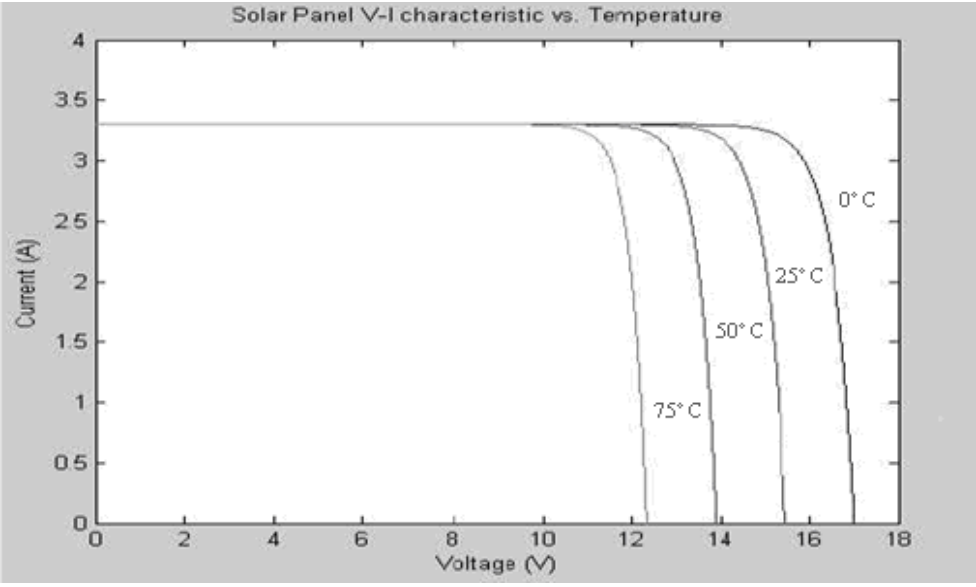

Fig. 2.5 Typical solar cell I-V characteristic showing effect of temperature [24]

Fig. 2.5 shows that the terminal voltage increases with decreasing temperature and vice versa. This is somewhat surprising since it would seem that the solar panel should operate more efficiently as temperature increases. However, the electron and hole mobility of the semiconductor material is responsible for the observed behavior. As temperature increases, the electron and hole mobility in the semiconductor material decreases significantly which results in a lower terminal voltage [27]. Another factor responsible for the observed effect is the band gap energy of semiconductor materials which also varies with temperature [29]. Irradiance and temperature are only two of the several factors that affect the output power of a solar cell but they represent the two most significant external factors. Inclination, location, and time of the year are also factors that affect the efficiency and output power of solar cells [30].

A major component in converting the power generated by the solar cell into useful electricity is the inverter. The solar cell generates DC power while most residential, industrial and commercial loads require AC power. Since the majority of loads are AC loads, the DC output of the solar panels must be converted into AC voltage at system frequency for grid-connected PV systems. An inverter is used to convert the DC power generated by the solar cell into AC power by use of power electronic switches. The solar cell constant current region up to the short-circuit limit makes the current output of the solar cell ideal for current-source inverters (CSI). However, due to the fluctuating nature of the sun and the operation of power electronic switches, a rather large reactor is required for smoothing and blocking reverse currents [31]. As a result, voltage-source inverters (VSI) are the most commonly used in the PV industry [32]. The voltage source inverter can be controlled by either a voltage or current method [31 - 35], whose target output is to output a certain voltage or current respectively.

For power system stability studies, a PV model that sufficiently represents the significant factors that affect the dynamic output of solar cells is required to properly study the effect of PV microgrid penetration on power system stability and reliability. In [36], a model of PV generation system that is suitable for stability analysis is presented. The model presented is a grid-connected system that incorporates the effect of temperature, irradiance, and grid AC voltage in the output power and voltage of the PV. The tracking technique implemented for the PV MPPT control in [36] is the commonly used perturb & observe (P & O) method, but there the PV current is continuously adjusted instead of the PV voltage as is typically the case. The PV model presented in

[36] is implemented in this research but with a modified tracking and control method. Where as the model in [36] tracked the maximum power output by continuously perturbing the operating point and comparing it to the previous iteration, with the aim of outputting the most power based on the current grid and ambient conditions, the control system proposed in this research controls the output power of the PV and the output voltage of the inverter by using a deterministic method to dynamically determine the optimal PV power and inverter voltage based on the current grid voltage and stability margins.

2.3 Power System Stability and Reliability

Power system stability is usually classified in terms of the steady-state, dynamic or transient stability. The steady-state stability refers to the response of the system to a gradually increasing load; the system is said to experience steady-state instability if it is unable to return to a state of equilibrium after a small disturbance. Gradually exceeding the power limits of the system will cause steady-state instability [37]. The second class of power system stability refers to the dynamic behavior of the system to oscillations. Small disturbances regularly occur on the power system, often producing oscillations, and the manner of those oscillations characterize the dynamic stability of the system. Oscillations that are of successively smaller magnitudes indicate that the system is dynamically stable, whereas if the oscillations continue to increase in magnitude, the system experiences dynamic instability [38]. The third classification of the power system

stability is the transient stability. A power system is described as transiently stable, if after a disturbance, it is able to return to equilibrium [38]. A large fault can cause a sudden system disturbance and the ability of the power system to withstand the shock of the large change that occurs characterizes its transient stability. Large disturbances tend to cause large changes in rotor speed and significantly affect voltage and frequency stability. Therefore, power system stability is usually classified in terms of the *rotor angle*, *voltage*, and *frequency* stabilities as shown in Fig. 2.6.

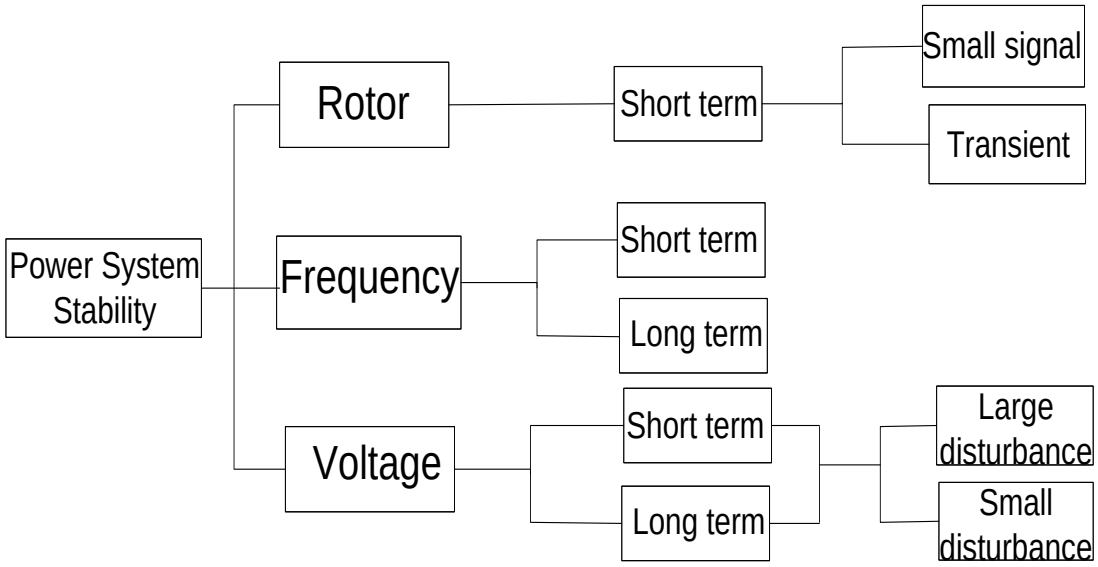

Fig. 2.6 Power system stability classification [37]

Rotor angle stability refers to the ability of synchronous machines of an interconnected power system to remain in synchronism after being subjected to a disturbance; it is influenced by the balance of the mechanical torque and the magnetic forces holding each machine in synchronism. Instability occurs in the form of increasing angular swings of some generators, which leads to loss of synchronism with other generators [37].

There are two types of rotor angle instability, depending on the size of the disturbance. The small signal disturbance (small disturbance) stability refers to the ability of the power system to maintain synchronism under small disturbances, such as a gradual increase in load while the transient (large disturbance) stability refers to the ability of the system to maintain synchronism under large disturbances, such as a large fault. Small signal stability is usually affected by insufficient damping torque, which results in small disturbances having oscillations of increasing magnitude and a loss of equilibrium. For relatively small disturbances, where the duration of interest is on the order of 10 to 20 seconds post disturbance, it is permissible to analyze the small signal stability using linearized models [38]. On the other hand, transient stability is highly influenced by the non-linear power angle relationship, and linearized models are not suitable for analysis [39]. Instead the analysis is done using non-linear time-domain simulations, where the duration of interest is three to five seconds post disturbance.

Frequency stability refers to the ability of a power system to maintain steady frequency, within acceptable range, following a severe system disturbance that causes significant imbalance between generation and load; it is influenced by the ability of the system to maintain balance between generation and load demand. Instability occurs in the form of sustained frequency swings, leading to generators and/or loads being switched off [37]. Unlike rotor angle and voltage stabilities, frequency stability is not classified based on the size of the system disturbance but rather on the overall response of the system. It can be described as a short or long term phenomenon as shown in Fig. 2.6.

Voltage stability refers to the ability of the system, normally operating, to maintain steady voltages at all buses after being subjected to a disturbance. It is influenced by the balance between load demand and supply. Instability occurs in the form of progressive drop in voltage at some buses. The system experiences voltage instability if at any bus, there is a drop in voltage as the reactive power is increased [38]. Similar to the rotor angle stability, the small signal voltage stability and the large disturbance voltage stability refer to the system's ability to maintain steady voltages at all buses when subjected to small and large disturbances respectively. A small disturbance may be a gradual increase in load or momentary voltage sag while a large sustained system fault would constitute a large disturbance. After a disturbance occurs on the systems, loads tend to be quickly restored on the power system as a result of the operation of automatic controllers such as auto-starters in induction motors. The sudden increase in reactive power consumption by the load worsens the voltage sag caused by the disturbance and the load reacts by further increasing the reactive power consumption. This process continues until the stability limit of the system is exceeded, resulting in voltage collapse or even widespread blackout. Some of the system parameters that influence the stability limit of the power system include the generation capacity and the network transfer capacity [40]. But loads are the primary drivers in voltage instability. The duration of interest in voltage stability studies may run from a few seconds to several minutes after the disturbance. Since voltage stability depends on both linear and non-linear characteristics of the system, a combination of both techniques is used for analysis.

Rotor angle stability can be viewed as a generator stability issue; voltage stability as a load issue; and frequency stability as a combination of generator and load balance. For this reason, the rotor angle stability is primarily influenced by real power transfer while voltage stability is mainly influenced by reactive power flow. A point to note is that it is possible for more than one type of instability to occur on the system at a given time, and therefore power system stability studies should be performed in the context of overall system stability.

Utilities are concerned with both the stability and reliability of the power supplied to customers. The reliability of power supply is measured by reliability indices that are recognized throughout the industry. Utilities are required to report and publish their yearly reliability indices, and they are subject to penalties if their performance fails to meet certain criteria. The indices indicate the annual average performance of the utilities based on the duration and frequency of interruptions to customers. The system performance indices are [41] described below.

The System Average Interruption Duration index (SAIDI) is the average duration of all interruptions per customer over the course of a year. This is the sum of the duration of all customer interruptions divided by the total number of customers for each utility over the period of interest.

$$SAIDI = \frac{sum\ of\ duration\ of\ all\ customer\ interruptions}{total\ number\ of\ customers}$$

The System Average Interruption Frequency Index (SAIFI) is the average number of *sustained* interruptions per customer over the course of a year. This is the total number of customers experiencing sustained interruptions divided by the total number of customers over the course of a year. The duration threshold that defines a sustained interruption varies across different regulatory environments but each interruption must be longer than the set threshold to be counted as a sustained interruption for SAIFI calculation, otherwise it is counted as a *momentary* interruption.

$$SAIFI = \frac{number\ of\ customer\ interruptions}{total\ number\ of\ customers}$$

The Momentary Average Interruption Frequency Index (MAIFI) is the average number of momentary interruptions per customer per year. This is the total number of customers that experience interruptions shorter than a set threshold divided by the total number of customers during the year.

$$MAIFI = \frac{number\ of\ customer\ momentary\ interruptions}{total\ number\ of\ customers}$$

The Customer Average Interruption Duration Index (CAIDI) is the average total duration of sustained interruptions per customer experiencing at least one outage per year.

$$CAIDI = \frac{sum\ of\ duration\ of\ customer\ interruptions}{total\ number\ of\ customers\ experiencing\ at\ least\ one\ outage}$$

These indices are used by the regulator to measure the performance of the utilities' network and ensure a minimum level of service is attained. The regulator may apply fines or suggest remedial action to improve the quality of service.

2.4 Momentary Interruptions and Voltage Sags

Momentary interruptions are brief disruptions in electric service that are usually caused by faults in the power distribution system. These interruptions are more noticeable now due to the increase in the use of sensitive power electronics equipment, while the cost of these interruptions is a major source of concern for utilities and customers. The total annual cost to US electricity customers as a result of interruptions in service is about $250 billion and rising, with momentary interruptions accounting for two-thirds of the overall cost [42]. In general, power quality disturbances refer to the deviations of the voltage and current from their ideal waveforms that can cause interruptions, tripping of equipment or improper power system operation. Voltage variations, such as momentary interruptions and voltage sags cause motors to run hard and overheat quickly, and while not always noticeable, can result in long-term damage to equipment. Voltage sags are characterized by short duration changes in rms voltage magnitude at the receiving end. IEEE Std. 1159 classifies an rms voltage disturbance based upon its duration and voltage magnitude. A magnitude-duration plot used in IEEE Std. 1159 is shown in Fig. 2.7. On the voltage magnitude axis, voltages less than 10% of nominal voltages are classified as interruptions; voltages between 10% and 90% are classified as undervoltages (sags); and

voltages above 110% are classified as overvoltages (surges). On the duration axis, events lasting less than half a cycle are classified as transient; events between half a cycle and 1 minute as short-duration; while events greater than 1 minute are classified as long-duration events.

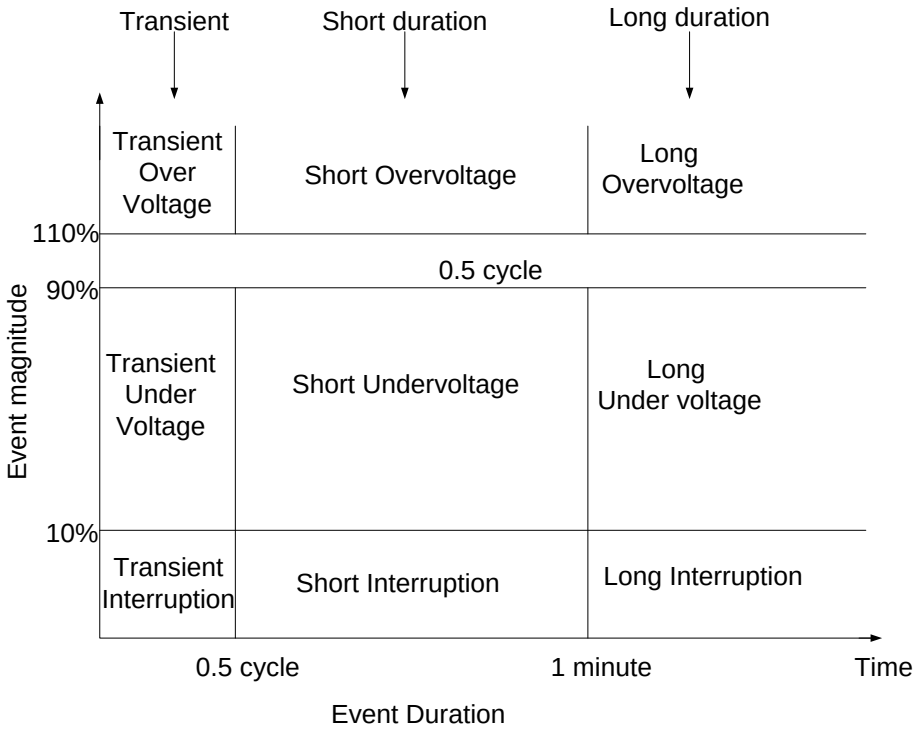

Fig. 2.7 Magnitude-duration plot for power quality events [41]

Of all the power quality phenomena, voltage sags and momentary interruptions are especially worrying for industrial customers because they have numerous loads that are sensitive to such voltage variations. Programmable logic controllers (PLC), robotics, variable-speed drive (VSD) controls, and even motor controllers are susceptible to malfunction under voltage sag conditions [43, 44]. Industrial customers with sensitive

process equipment, such as semi-conductor manufacturing facilities or medical facilities using MRI and CTs machines, often have to restart or reprogram the machine as a result of voltage sags, while work-in-process wafers or scans may need to be scrapped. As a result, there is a concerted effort in industry to reduce the number of momentary interruptions in the power system, measured by the MAIFI index.

2.5 Recent MAIFI Performance Indicators for Florida Utilities

The Florida Public Service Commission (PSC) publishes annual MAIFI scores for the four largest utilities in Florida: Florida Power & Light (FPL), Progress Energy Florida (PEF), Tampa Electric Co. (TECO), and Gulf Power Co. (Gulf) with approximately 4.5 million, 1.6 million, 670,000, and 430,000 customers respectively. The adjusted MAIFI for years 2004 -2008 is shown in Fig. 2.8.

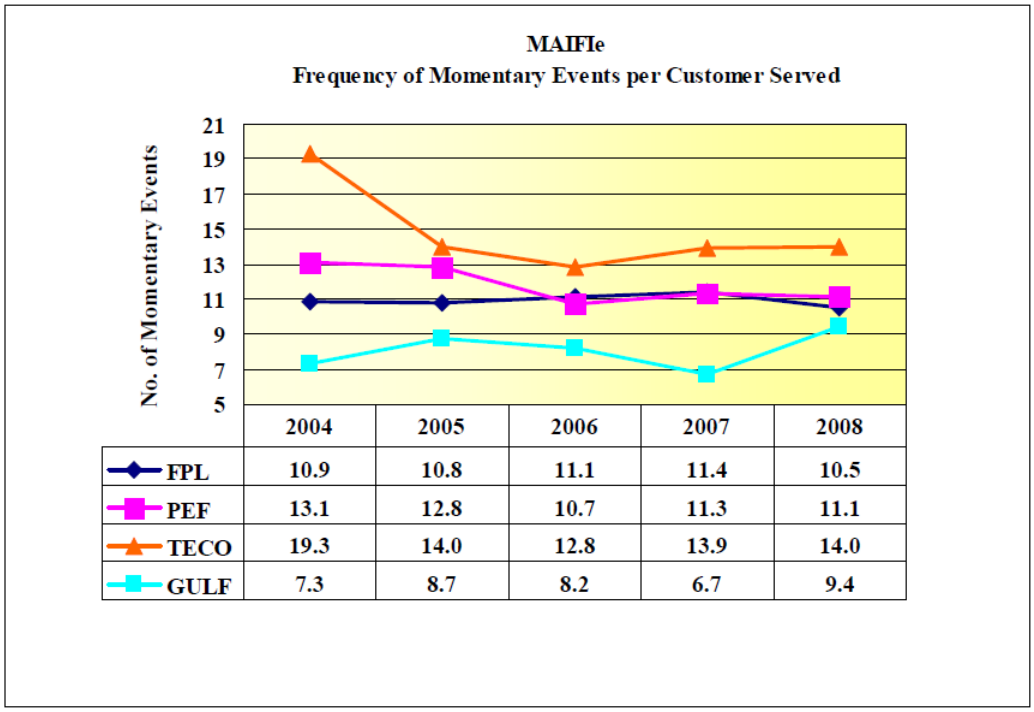

Fig. 2.8 Adjusted MAIFIe for Florida Utilities, 2004 -2008 [45]

The general trend suggests improvements have been made by TECO and PEF over the review period, although TECO showed decreased performance from 2007 to 2008. FPL had a flat performance trend over the period with some improvement made between 2007 and 2008, while Gulf showed remarkable decrease in performance between 2007 and 2008. The service reliability complaints received from customers by the PSC also shows that the quality of service complaints does not exhibit the desired decreasing trend over the period since that category of complaints was established in 2003 [45]. This highlights the need to develop strategies to mitigate the occurrence and impact of voltage sags, even as the power system landscape evolves with the addition of significant amounts of DG sources.

2.6 Various Voltage Sag Mitigation Methods

Voltage sags and momentary interruptions adversely affect the power quality experienced by electricity customers. Increased load sensitivity and production automation are two of the major factors driving interest and concerted efforts to mitigate the occurrence and impact of voltage sags [46]. The methods applied to mitigate the problem occur at the utility, customer and equipment manufacturers' levels. Sensitive electronic equipment are designed with a greater tolerance to voltage sags while the customer can install voltage regulating equipment such as uninterrupted power supply (UPS), dynamic voltage restorer (DVR) or coil hold-in devices near sensitive loads to protect the equipment. The utility is primarily focused on maintaining the stability of the overall power system, thus the utility attempts to first maintain a balance between demand and supply, then ensure that the voltage at all buses in the power system are maintained within a desired range. In the case where the demand exceeds the supply, the utility is forced to shed non-critical loads in order to avoid power system instability and voltage collapse [47].

The criteria for voltage stability margin for load shedding purposes proposed in [47] only deals with load shedding at the sub-station after the system has experienced a severe disturbance leading to voltage collapse. In order to forestall voltage collapse, the utility installs reactive power compensation devices such as shunt capacitors, STATCOMs, SVCs and FACTS devices in the power distribution system to support the voltage at weak buses [48]. However, there is a limit to the number of locations where these devices can

be reasonably installed mainly due to the associated cost and low utilization factor. Devices deployed at locations that require voltage compensation during peak hours only can remain idle for up to 20 hours each day, therefore costly SVCs and FACTS devices are usually only deployed at critical locations where quick voltage regulation is required [49].

Recently, distribution generation has been explored as a solution to mitigate voltage sags in the low-voltage distribution network [50]. The impact of grid-connected DG units during voltage sags is investigated in [51] for asynchronous generators, synchronous generators and converter-connected DG units. The impact of commercially available converter-connected DG is reported to be negligible since most converters operate at unity power factor and the current injected into the grid is limited to the nominal current of the inverter [51]. A method to control the converter-connected units to obtain a better voltage sag ride-through capability is presented in [52]. The controller employs damping resistance to prevent premature shutdown of the converter due to excessive bus voltage when the injected power is increased to counter the voltage sag. However, this approach has limited application for deep voltage sags at buses containing a high number of induction motors where the converter shuts down due to excessive bus voltage, since only the active power injection is regulated and the voltage at the PCC exceeds acceptable limits before the voltage at the motor terminals recover.

A method to operate grid-tied DGs to individually regulate both the active and reactive power injection into the load bus is presented in this work. The impact of such

converter-connected DGs during voltage sags is investigated and the outcome is compared to the results obtained in [51]. The method improves on the approach presented in [52] by dynamically regulating the reactive power injection of the converter during voltage sags thus preventing the excessive bus voltage that results primarily from the active power injection at the load.

3. MICROGRID IMPACT ON POWER SYSTEM VOLTAGE STABILITY

The power system generally experiences voltage instability when there is a real and/or reactive power imbalance between the generators and the loads. The reasons for the static and dynamic voltage instability of a power system are investigated in this chapter. The basic concepts related to voltage instability are illustrated by firstly considering the characteristics of the transmission and distribution systems and then examining how the phenomenon is influenced by the behavior of generators, loads, and reactive power compensation equipment. The voltage stability behavior of the power system changes significantly when distributed resources are added to the grid as a result of the reconfiguration of the power flow. Therefore, prior to deploying DGs in the power system, it is necessary to properly model and analyze the impact of adding DGs at different locations in the grid. The standard mathematical models of the various power system components, including the synchronous generator and photovoltaic source, are presented and implemented in Matlab/Simulink. The implemented models are used to determine the effect of grid-connected PV sources on local voltage regulation and power system reliability. Some remedial actions such as dynamic voltage regulation and active anti-islanding that can be implemented to prevent overvoltages and nuisance fuse operation are explored and presented.

3.1 Power Flow in Radial Power Systems

The power system can experience instability when there is an imbalance between the load demand and the capacity of the power system to provide sufficient power to the loads from the generation and transmission ends. However, the power flow in the emerging DG-embedded power system varies significantly from the power flow in the traditional radial power system since the sources and loads are much closer in proximity in the former than in the latter. With the shifting paradigm, the effect of the new configuration of the power system on voltage stability at the distribution level needs to be investigated to ensure the proper design and optimal placement of microgrids in the power system. The power flow in a short transmission line is used to illustrate the power flow in the existing radial power system. The single line diagram and equivalent circuit are shown in Figs. 3.1 and 3.2.

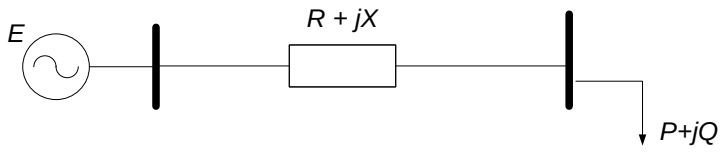

Fig. 3.1 Two-bus short transmission line power system

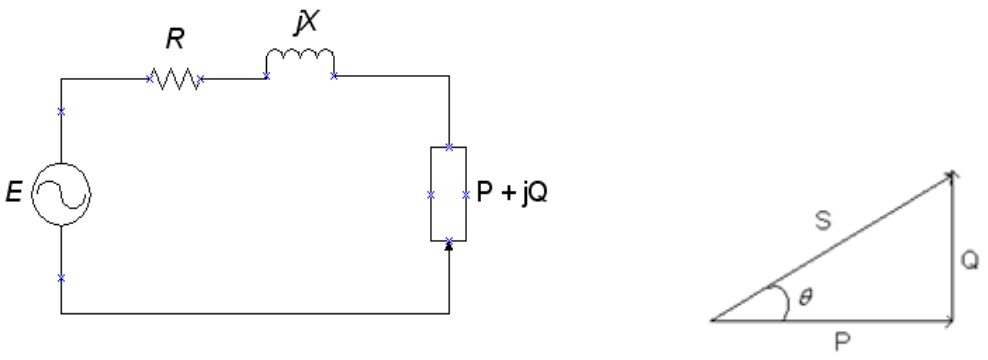

(a) (b)

Fig. 3.2 a) Equivalent circuit of a short transmission system and, b) phasor relationship between source and load voltage

We assume the transmission line shown has negligible resistance and the series impedance is jX Ω/phase. The source and load side voltages are E_S and V_L respectively. It is known that V_L lags E_S as shown in Fig. 3.2.

The real and reactive power and reactive power at the source and load can be determined using the phasor relationship:

The total power S is given by

$$S = P + jQ \quad \text{[VA]} \tag{3.1}$$

At the source,

$$S_S = P_S + jQ_S \text{ [VA]} \tag{3.2}$$

In the short transmission system shown in Fig. 3.1,

$$I = \frac{1}{jX}(E_S - V_L) \qquad \text{[A]} \tag{3.3}$$

$$I^* = \frac{1}{-jX}(E_S^* - V_L^*) \qquad \text{[A]} \tag{3.4}$$

where *I** is the complex conjugate of *I*

Substitute (3.4) into (3.2),

$$S_S = \frac{E_S}{-jX} \qquad \text{[VA]} \tag{3.5}$$

Now,

$$V_L = V_L^* = |V_L| \qquad \text{since } V_L = |V_L|\angle 0^\circ$$

$$E_S = |E_S|\angle\theta = |E_S|e^{j\theta}$$

Eq. (3.4) becomes

$$S_S = \frac{|E_S|^2 - |V_L||E_S|e^{j\theta}}{-jX} \text{ [VA]} \tag{3.6}$$

and since

$$S_S = P_S + jQ_S \text{ , and } \quad e^{j\theta} = \sin\theta + \cos\theta$$

$$P_S = \frac{1}{X}(|E_S||V_L|\sin\theta) \qquad \text{[W]} \tag{3.7}$$

$$Q_S = \frac{1}{X}(|E_S|^2 - |E_S||V_L|\cos\theta) \qquad \text{[VAR]} \tag{3.8}$$

$$P_L = \frac{1}{X}(|E_S||V_L|\sin\theta) \qquad \text{[W]} \tag{3.9}$$

$$Q_L = \frac{1}{X}(|E_S||V_L|\cos\theta - |V_L|^2) \qquad \text{[VAR]} \tag{3.10}$$

It is seen that the transfer of real power depends primarily on the power angle, ϑ, as opposed to a DC system, where the power flow depends entirely on the magnitude of the end voltages and the power always flows in the direction of the lower voltage.

From eqs. (3.7) and (3.9), it is clear the maximum power transfer occurs when $\vartheta = 90°$.

$$P_S = \frac{1}{X}(|E_S||V_L|) \qquad \text{[W]} \tag{3.11}$$

while eqs. (3.8) and (3.10) show that the reactive power will flow in the direction of the lower voltage.

If the source and the load voltages are assumed to be in phase, i.e. $\vartheta = 0°$, then the average reactive power flow is

$$Q_{avg} = \frac{1}{2}(Q_S + Q_L) = \frac{1}{2X}(|E_S|^2 - |V_L|^2) \qquad \text{[VAR]} \tag{3.12}$$

From (3.12), it is seen that the average reactive power flow is strongly dependent on the difference in voltages at the two ends.

If the I^2R losses in the transmission lines are considered,

$$P_{line} = |I|^2R = \left(\frac{P^2-Q^2}{|V|^2}\right) \times R \text{ [W]} \tag{3.13}$$

Eq. (3.13) shows that the power loss in the transmission line is dependent on both real and reactive power. The simplified transmission line shown in Fig. 3.1 shows the effect of the reactive power flow when transferring power from one end of the transmission system to the other in a typical vertical power system. This dependence of the reactive power flow on voltage magnitudes allows the bus voltage to be maintained at a desired level by controlling the flow of reactive power to the bus.

3.2 Impact of Voltage Regulating Devices

Four of the most common methods currently used to control the amount of reactive power in the system, and thus regulate the voltage, include –

- adjusting synchronous generators or motor field excitation
- using shunt capacitors
- using FACTS devices
- using load-tap-changing (LTC) transformers

Synchronous generators are the main source of reactive power in the power system, and thus are largely responsible for maintaining a good voltage profile across the power system. In order to maintain system stability, all the synchronous generators must remain in synchronism [53]. The equation governing the rotor motion of the generator is given as [54]:

$$\frac{2H}{\omega_0}\ddot{\delta} = T_m - T_e \tag{3.14}$$

where H is the inertia constant, T_m and T_e are the mathematical and electrical torques respectively, and δ is the electrical angle between the machine quadrature axis and a synchronously rotating reference axis.

For a given constant speed of the rotating synchronous reference, the *swing equation* is given as [54]:

$$\frac{2H}{\omega_0}\ddot{\delta} + \frac{D}{\omega_0}\dot{\delta} = P_m - P_e \tag{3.15}$$

where D is the damping coefficient, and P_m and P_e are the mechanical and electrical powers produced by the machine.

The block diagram representation of the swing equation of the synchronous generator is shown in Fig. 3.3.

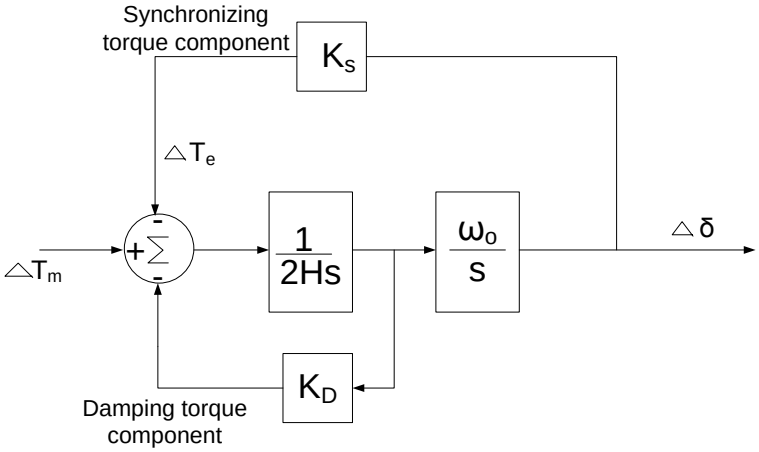

Fig. 3.3 Synchronous generator swing equation block diagram [37]

Each synchronous generator is equipped with an Automatic Voltage Regulator (AVR) and an excitation control system to regulate the output voltage and protect the generator from losing synchronism respectively. The underexcitation limiter prevents overheating of the stator end region due to excessive reduction in machine excitation while the overexcitation limiter prevents the field winding from overheating due to excessive current [55]. The AVR is used to regulate the voltage point at the generator to ensure the proper sharing of reactive power produced by multiple generators connected to the same bus. The block diagram of the AVR model is shown in Fig. 3.4.

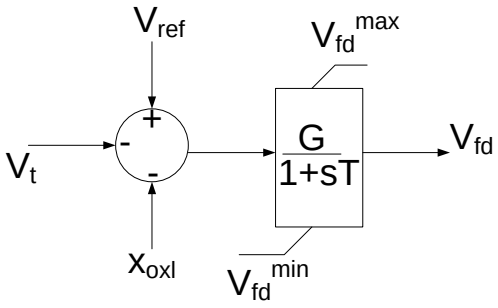

Fig. 3.4 Synchronous generator AVR block diagram [54]

The operation of the AVR model is governed by the following equations:

$$\dot{v}_{fd} = 0 \text{ if } v_{fd} = v_{fd}^{max} \; and \; G\left(V_{ref} - E_g - X_{oxl}\right) - v_{fd} > 0$$

$$\dot{v}_{fd} = 0 \text{ if } v_{fd} = v_{fd}^{min} \; and \; G\left(V_{ref} - E_g - X_{oxl}\right) - v_{fd} < 0 \quad (3.16)$$

$$\dot{v}_{fd} = \frac{G\left(V_{ref} - E_g - X_{oxl}\right) - v_{fd}}{T} \qquad \text{otherwise}$$

where v_{fd}^{min} and v_{fd}^{max} are the minimum and maximum field voltages respectively. E_g and V_{ref} are the generator and AVR reference voltages respectively. *G* and *T* are the AVR gain and time constants respectively while X_{oxl} is the output of the overexcitation limiter.

The set of differential equations that govern the dynamics of the synchronous generator is given as [56]:

$$\dot{\delta} = \omega \tag{3.17}$$

$$\dot{\omega} = -\frac{D}{2H}\omega + \frac{\omega_0}{2H}(P_m - P_e) \tag{3.18}$$

$$\dot{E}'_q = \frac{-E'_q + v_{fd} - (X_d - X'_d)i_d}{T'_{do}} \tag{3.19}$$

where $\dot{E}'_q$ is the voltage behind the transient reactance, v_{fd} is the field voltage at the armature, T'_{do} is the open circuit time constant, and i_d is the direct-axis armature current. X_d and X'_d are the direct axis reactance and transient reactance respectively.

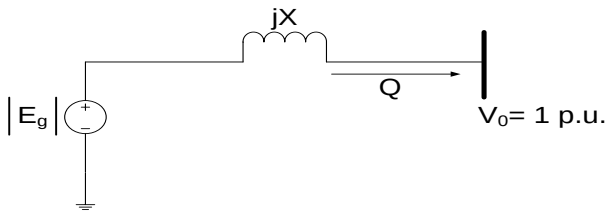

Fig. 3.5 Increase in synchronous generator field excitation

Increasing the field excitation on a synchronous generator will result in an increase in the magnitude of the generator voltage, $|E_g|$, as shown in Fig. 3.5. The generator is assumed to be connected to a bus operating at a voltage of $1\angle 0°$ p.u. The magnitude of generator $|E_g|$ can be increased or decreased by raising or lowering the generator or motor field current. If the real power flow is neglected and only the reactive power flow is considered, then the average power flow is proportional to $\left(|E_g|^2 - 1^2\right)$. Therefore, for a synchronous generator or unloaded synchronous motor, increasing the field excitation will result in reactive power flow into the system bus as shown in Fig. 3.5. This causes an increase in the voltage at the bus.

Shunt capacitors are used to control the bus voltage by supplying reactive power to the bus at which the capacitor banks are connected. The shunt capacitors supply reactive power to the load thereby reducing the inductive reactance seen at the generator by way of power factor correction. This reduces the line current necessary to supply the load, resulting in lower voltage drop and I^2R losses in the line. However, this approach to reactive power control becomes counterproductive if too much capacitance is added as the line current leads the voltage and the VARs begin to rise again. The static on/off switching of capacitors can also introduce significant harmonics and in-rush currents into the load, and therefore switching capacitors around extremely sensitive equipment often require additional design complexity.

Flexibles alternating current transmission system (FACTS) devices such as Static VAR compensators (SVC) and static synchronous compensators (STATCOM) involve using

electronically switched inductors and capacitors to control the reactive power flow in a similar manner to shunt capacitors. Typically, thyristor switching helps to quickly provide VARs in response to transient events, damping the reactive power demand and minimizing the voltage drop in the line. However, in contrast to the operation of shunt capacitors which typically correct the steady state power factor at the distribution end, FACTS devices are used in the transmission system to compensate for transient reactive power imbalance, usually for a very short period, in order to maintain the power system voltage within acceptable limits and prevent the system from dropping critical loads.

Regulating or load-tap-changing (LTC) transformers are used to control the flow of real or reactive power, since they are able to regulate the magnitude and phase angles of line voltages. Regulating transformers are primarily designed to adjust the voltage magnitude along a line or provide a change in phase. LTC transformers have taps on their windings that vary the turns ratio slightly in the range up to ±10 %, with a ratio change of ~ 0.625 % per step as shown in Fig. 3.6.

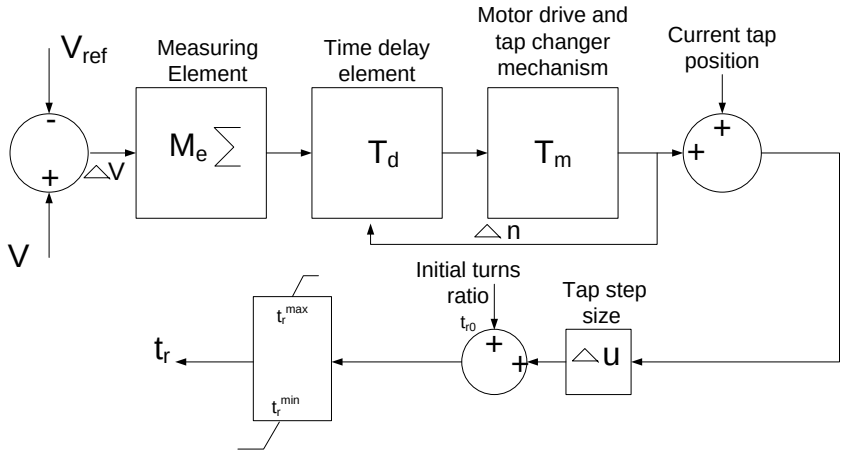

Fig. 3.6 Load-tap-changing (LTC) block diagram [57]

Normally, the taps are located on the primary side of the transformer since there is less current to be switched by the tap changers than on the secondary side. The tap changing is sometimes done on no load, but the LTC transformers usually operate in conjunction with motors and relays for automatic tap changing.

All of the methods described above to balance the reactive power demand at the load are each limited in some manner – the synchronous generator is limited by the reactive power transfer capacity of the line; the shunt capacitor is limited by the amount of stored VARs; FACTS devices are generally very expensive and are usually only deployed at critical locations; and the LTC is only able to regulate the reactive power already on the system [57 - 60]. Another possible method to balance the reactive power flow, though seldom utilized, is to use the reactive power capability of grid-tied DGs to support the reactive power demand at the loads.

Most DGs are typically operated with a power factor at or close to unity [51, 61, 62], but this mode of operation leaves the DG under-utilized since no reactive power is being generated to support the load bus voltage. DGs are usually connected at the distribution level and sited close to the loads (e.g. customer premises), thus any reactive power generated does not have to travel a great distance to the load and the line losses are minimized. This is similar to the operation of shunt capacitors and static VAR compensators except the DG can also be used to supply active power when required (often the “normal” operating mode). Grid-tied DGs tend to raise the voltage at the point-of common-coupling (PCC) [17 – 20, 63], and the need to limit this voltage rise is

the limiting factor in the reactive power capacity of the DG [64]. In the next sections, the circuit model of the PV source is used to investigate the impact the fluctuating nature of the PV output has on the power system voltage stability and then additional impacts of adding DGs to the power distribution system are discussed.

3.3 Photovoltaic Modeling and Simulation

The photovoltaic module consists of solar cells that produce electricity when exposed to sunlight. The solar cells are primarily made of semiconductor material whose properties determine how much of the sun's energy can be captured and successfully converted to electrical energy [23]. A solar module comprises of a series and/or parallel combination of solar cells connected so as to deliver a desired output voltage and current. Solar cell manufacturers usually provide some key parameters of a solar module in their Data Sheet including the output power, the open-circuit voltage and the short-circuit current among others. The output power is given in W_p (Watt peak), which means the module was rated at Standard Test Conditions (STC). The STC are an illumination level of 1000 W/m^2 (bright sunshine), a spectrum equivalent to AM 1.5 and 25℃ module temperature at the test. The short circuit current is the current produced when the output voltage is zero, and the open circuit voltage is the voltage across the output terminals when there is no current flowing in the cell.

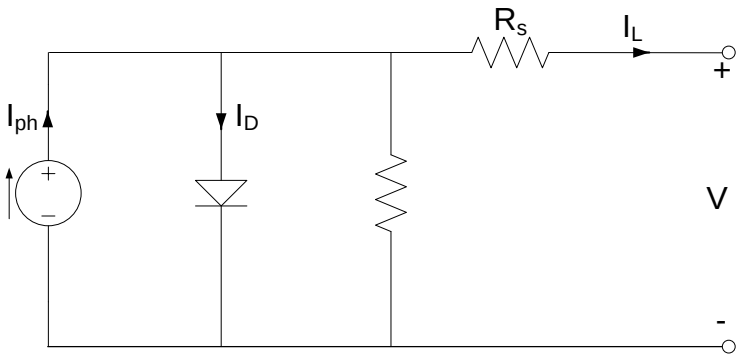

Fig. 3.7 Five-parameter equivalent circuit of a solar cell

The five-parameter equivalent circuit shown in Fig. 3.7 is commonly used to represent a solar cell [65]. A simplified four-parameter equivalent circuit is shown in Fig. 3.8 and it consists of a diode and a current source which are switched in parallel and a series resistance. The parallel resistance R_p in the five-parameter equivalent circuit is normally very large and has been neglected in the four-parameter equivalent circuit. The photocurrent generated when the sunlight hits the solar panels can be represented with a current source and the p-n transition area of the solar cell can be represented with a diode.

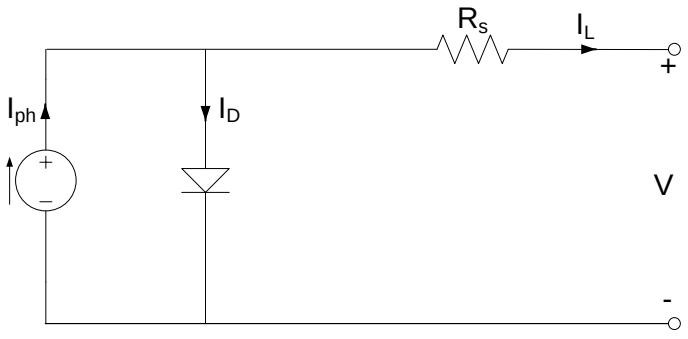

Fig. 3.8 Simplified four-parameter equivalent circuit of solar cell

The voltage and current relationship of the simplified solar cell is derived from Kirchhoff's current law. According to Kirchhoff's current law, all currents entering and leaving a node add up to zero.

Thus,

$$I = I_{ph} - I_D = I_{ph} - I_s \left[e^{\left(\frac{V}{mV_T}\right)} - 1 \right] \tag{3.20}$$

where I_{ph} is the photocurrent generated by the solar cell, I_D and I_s are the diode forward and reverse saturation currents respectively, m is the diode ideal factor and V_T is the thermal voltage (25.7mV at 25°C).

The mathematical model of the solar module can be used to determine the voltage and current at which the maximum power is extracted from the solar cell.

The current through the solar cell is derived from

$$I = I_s \left[e^{\left(\frac{V}{V_T}\right)} - 1 \right] - I_{ph} \tag{3.21}$$

This expression is a simplified form of the equation provided earlier as it does not include the diode ideal factor, essentially ignoring the recombination of the electrons and holes in the depletion region of the semiconductor material. The photocurrent I_{ph} is assumed to be independent of applied voltage.

The short circuit current I_{sc} is the current with no voltage applied and equals

$$I_{sc} = -I_{ph} \tag{3.22}$$

The open circuit voltage V_{oc} is the voltage with zero current and equals

$$V_{oc} = V_T \ln\left(\frac{I_{ph}}{I_s} + 1\right) \approx V_T \ln\frac{I_{ph}}{I_s} \tag{3.23}$$

The total power dissipated equals

$$P = V \times I = I_s V\left(e^{\frac{V}{V_T}} - 1\right) - I_{ph}V \tag{3.24}$$

Considering that the maximum power occurs when $\frac{dP}{dV} = 0$, it is possible to derive the maximum voltage point V_m and the maximum current point I_m as

$$\frac{dP}{dV} = 0 = I_s\left(e^{\frac{V_m}{V_T}} - 1\right) - I_{ph} + \frac{I_s V_m}{V_T} e^{\frac{V_m}{V_T}} \tag{3.25}$$

At the maximum power point, the equation can be rewritten as

$$V_m = V_{oc} - V_T \ln\left(1 + \frac{V_m}{V_T}\right) \tag{3.26}$$

V_m is calculated by solving the transcendent equation above provided V_{oc} is known. The maximum current point I_m is

$$I_m = I - I_0\left(e^{\frac{V_m}{V_T}} - 1\right) \tag{3.27}$$

The maximum power can be approximated by

$$P_m = I_m \times V_m \approx -I_{ph}\left(1 - \frac{V_T}{V_m}\right)\left[V_{oc} - V_T \ln\left(1 + \frac{V_m}{V_T}\right)\right] \tag{3.28}$$

$$P_m \approx -I_{ph}\left[V_{oc} - V_T \ln\left(1 + \frac{V_m}{V_T}\right) - \frac{V_{oc}V_T}{V_m}\right] \tag{3.29}$$

The mathematical model of the PV module is implemented in Matlab/Simulink to observe the effect of temperature and irradiance on the output power. From the electrical characteristics of the solar cell, it is apparent that the solar cell is a non-linear device and therefore a non-linear modeling approach is required. One approach to handling non-linear circuits in Simulink is to define modules for the main blocks. Using modules to model the solar cell is helpful when connecting several solar cells in series or in parallel to obtain a specific output.

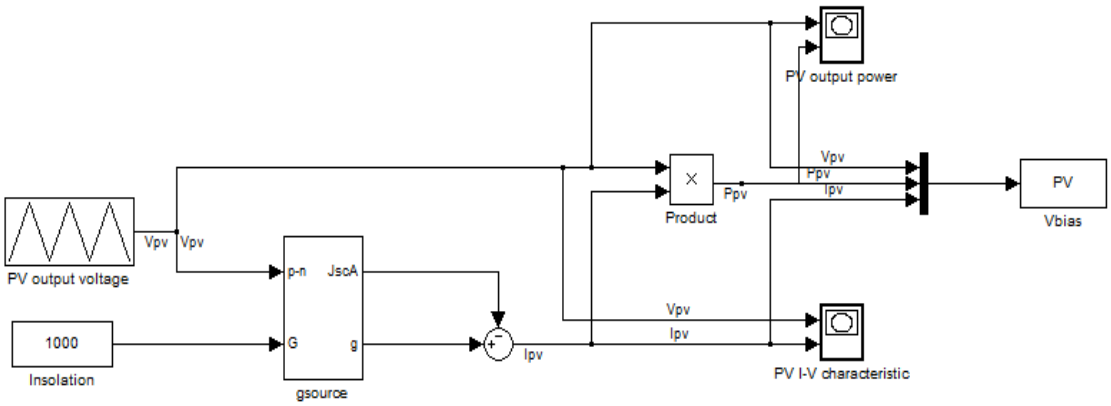

Fig. 3.9 Simulink block diagram of solar cell

The Simulink block diagram of a single solar cell is shown in Fig. 3.9. The model of an ideal solar cell is the circuit representation of the current equation shown in eq. (3.21). The short

circuit current is proportional to the incident irradiance on the solar cell and this is implemented in Simulink by assigning the value of the short circuit current to a voltage-controlled current source. The voltage-controlled current source used is named 'g_{source}' and is given by

$$g_{source} = \frac{J_{sc}A}{1000}G \tag{3.30}$$

where A is the solar cell surface area, J_{sc} is the short-circuit current density under standard conditions (AM1.5G, 1000 W/m^2, 25 ºC cell temperature), and G is the value of the irradiance in W/m^2.

The above equation gives the value of the short circuit current at any irradiance value G, so long as the proportionality between irradiance and short circuit current holds. The solar cell module is connected to an external measurement circuit in order to obtain the I-V characteristic. The external circuit includes a DC bias voltage source which is swept from 0 V to 600 mV and the simulated I-V characteristic is shown in Fig. 3.10. The parameters of the solar cell are taken from [24].

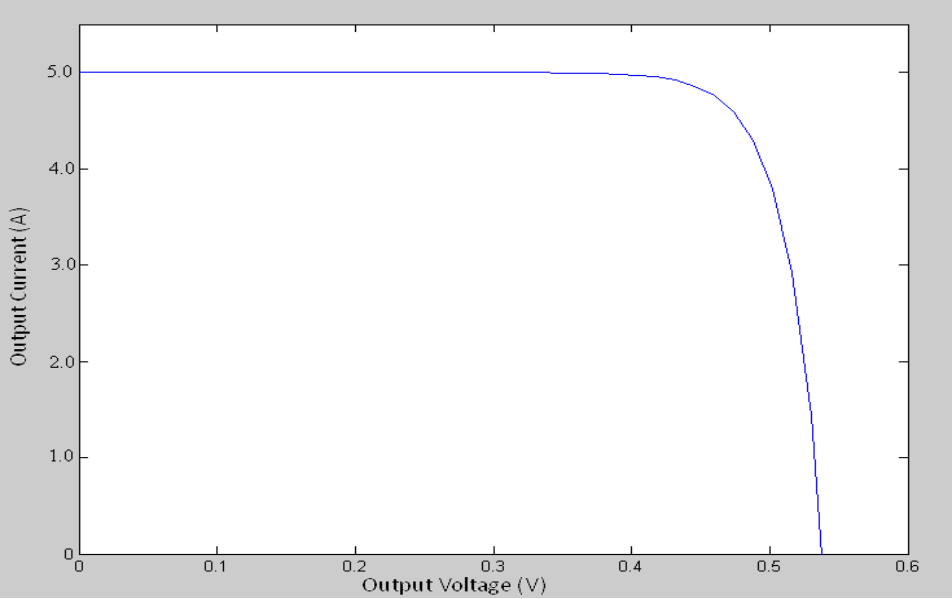

Fig. 3.10 I-V characteristic for a single solar cell

From the equation of the open circuit voltage in eq. (3.23), the value of the open circuit voltage depends logarithmically on the $\frac{I_{ph}}{I_s}$ ratio. Thus, under constant temperature the value of the open circuit voltage scales logarithmically with the short circuit current, and since the short circuit current scales linearly with irradiance, the open circuit voltage is logarithmically dependent on the irradiance. This important relationship indicates that the effect of irradiance is much larger in the short circuit current that in the open circuit voltage value.

The I-V characteristic of a solar module consisting of 36 identical solar cells connected in series, with each assumed to have the same irradiance value, will have the same short circuit current point as a single solar cell characteristic while the voltage drop for the solar module is 36 times the voltage drop for one solar cell. The output power of the solar

module is the product of the output current delivered to the load and the voltage across the series-connected solar cells. The power at any point of the I-V characteristic is given by eq. (3.24), where there is no power generated at either the short-circuit point or open-circuit point since there is zero voltage and current at the y-axis and x-axis respectively. The maximum power is generated at some point between the short-circuit point and the open-voltage point and is usually referred to as the maximum power point (MPP). The effects of irradiance and temperature on the output power of the solar module are shown in Fig. 3.11 and 3.12 respectively.

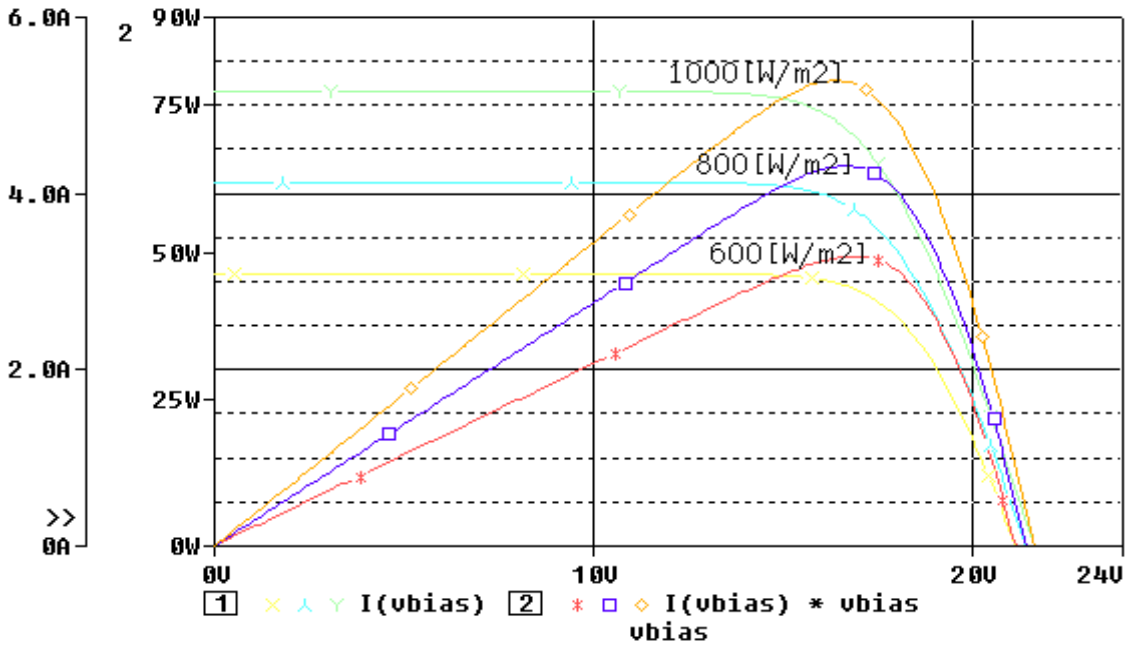

Fig. 3.11 Variation of output power due to changing irradiance [24]

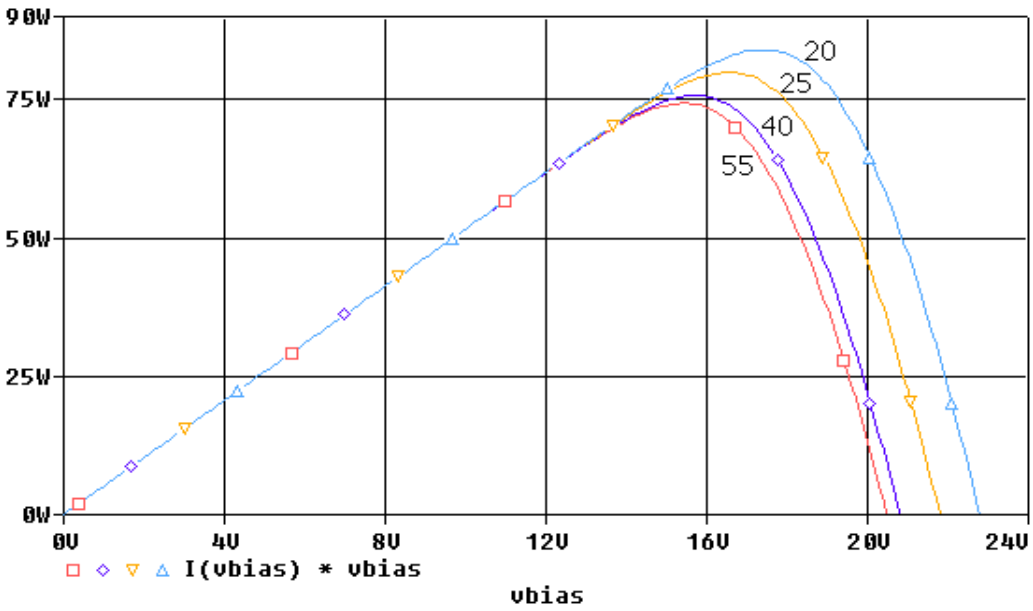

Fig. 3.12 Variation of output power due to changing temperature [24]

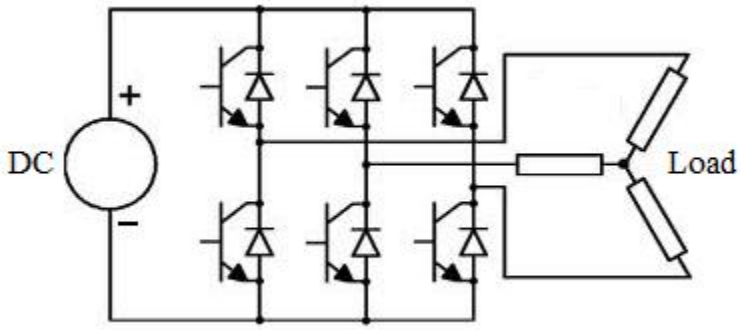

Fig. 3.13 Equivalent circuit of a three-phase inverter

The DC output power of the PV is converted into useful AC power by an inverter. The equivalent circuit of a three-phase inverter is shown in Fig. 3.13. The switches shown can be basic on/off switches that are controlled to generate a basic square wave, or in the case of AC loads and grid-connected PV systems, a pulse-width-modulation (PWM) switching scheme used to generate an almost pure sine wave. The switching devices can

be any number of semiconductor devices such as transistors, Thyristors, Gate-Turn-Off (GTO) devices, Insulated-Gate-Bridge-Thyristor (IGBT). The IGBT is the most commonly used switch in three-phase inverters.

Various switching techniques can be used to control the inverter to produce both active and/or reactive power by controlling the switching angles of each of the IGBT switches [34]. However, the inverter is only able to convert as much power as the solar panels and MPPT can produce and thus the operation of grid-tied PV inverters can adversely affect the power system stability due to the fluctuating nature of the sun [5, 37]. As such the output real or reactive power that can be generated by a PV system is dependent on the instantaneous ambient conditions and the operation method of the inverter module. In the next chapter, the analytical method of bifurcation theory is used to determine the maximum DG capacity at a distribution network location based on the impact on the power system voltage stability. The inverter control method that is used to dynamically regulate the desired real or reactive power injection to enhance the voltage stability of the power system is developed in Chapter 5.

3.4 Microgrid Impacts on Power Distribution Systems

It is sometimes possible to add small amounts of DG to the power distribution system without significantly modifying the existing system, provided there is proper grounding, transformer capacity, and adequate protection, but when the addition of DGs go

beyond the limit of what the already designed system can support, it is necessary to modify the existing system equipment and protection to facilitate the safe integration of new DGs [66]. The addition of new equipment may include larger switchgears, reconfigured protection systems, improved dynamic voltage regulation systems and revised grounding.

Some of the benefits that may be derived from addition of DGs include reduction in T&D losses, enhanced service reliability and quality, improved voltage regulation and relieved T&D system congestion [67]. However, interconnecting DGs to the grid could alternatively worsen the performance of the power system leading to negative consequences [14, 15, 17]. In fact, the reliability of the power system may be reduced if the DG is not properly coordinated with the existing power system protection and leads to the unnecessary tripping of protection devices or exceeding the safe operating limit for power system equipment. The addition of DGs may also introduce voltage harmonics and flickers due to poor voltage regulation which can seriously impact on the operation and performance of the electric power system and lead to equipment damage at downstream loads.

To address the challenges related to connecting DGs to the existing power system, standards for interconnecting DGs with electric power systems were established in 2003. The IEEE 1547 (2003) interconnection standard was established to provide interconnection technical specifications and requirements and test specifications and requirements. Before examining the major technical and test specifications and

requirements , it is important to note that IEEE 1547 is limited to DGs with up to 10 MVA aggregate DR capacity, interconnection at typical primary (~2.4 kV to 34.5 kV) or secondary (<600V) voltage levels, with the main emphasis being on radial systems. The interconnection technical specifications and requirements focuses on general interconnection requirements, response to area electric power system (EPS) abnormal conditions, power quality, and islanding phenomenon. Also, the interconnection test specifications and requirements address design tests, production tests, interconnection installation evaluations and commissioning tests.

Prior to deploying DGs in the field, design and production tests are required to be carried out to determine if certain IEEE 1547 requirements have been met. The design tests on interconnection equipment include testing the response of the equipment to abnormal voltage and frequency, testing the interconnect integrity, detection of harmonics, and use of active techniques to detect unintentional islanding [16]. The installation design evaluation examines the impact on Area EPS system voltage, grounding integration, isolation device, Area EPS fault sensing, reclosing coordination, flicker, and passive techniques to detect unintentional islanding [16].

Although IEEE 1547 standard covers a broad range of interconnect issues, not all technical issues are currently addressed by the standard. Some of the technical issues that are not addressed but need to be investigated include impact on Area EPS overcurrent protection scheme, DG penetration limits, redundancy, and dynamic character of distribution system (loads change and frequent configuration changes).

During normal Area EPS operation, the DG impact of greatest concern is the voltage regulation, as this impacts most on the stability of the overall power system [68]. Specifically, IEEE 1547 states that the DG shall not actively regulate the voltage at the point of common coupling (PCC) nor cause the Area EPS service voltage at other local EPS's to go outside the requirements of ANSI (84.1-1995, Range A) [16].

3.4.1 Islanding Phenomenon

Another technical issue of great concern resulting from one or more DGs being connected to the power system is unintentional islanding, which occurs when a portion of the distribution system becomes electrically isolated from the grid, yet continues to be energized by the DG connected to the isolated subsystem. Sometimes it is desirable to operate in an island mode, such as when DG is used as on-site backup generation, but in general, unintentional islanding is an undesirable situation.

DG is sometimes used to provide backup power to a facility, or to supply power to remote loads. In the former case, the DG is designed to maintain continuous power supply to the facility when a fault occurrence leads to disconnection from the main grid. In the latter case, the DG is designed to operate in a stand- alone mode and is used to supply power to loads that are inaccessible to grid supply. An example of such application is the operation of DG to power mobile telecommunications base stations in remote regions. In the case where the DG is used to provide backup power, the DG

supplies the load demand until grid supply is restored. Proper safety and protection measures must be taken to ensure that the DG is not inadvertently feeding power to the grid, as this can pose a major safety risk. A section of the distribution network containing a DG providing backup power may be de-energized from the grid but still pose a safety risk to maintenance personal working in the area if the DG is of sufficient capacity and inadvertently feeds power back into the de-energized portion of the grid. More recently, DG microgrids are becoming more prominent where the loads are served concurrently by the DG and the main grid.

The phenomenon where a DG inadvertently supplies power to a de-energized section of the grid is described as unintentional islanding. The occurrence of unintentional islands in the distribution network is one of the major issues in interconnected systems with the rapid growth of DG deployment [69]. With an ever increasing level of DG penetration in the distribution network, it is expected that the likelihood of unintentional islanding has substantially increased along with the concerns associated with the phenomenon. This is particularly the case among utilities and network operators [69, 70]. The main hazards associated with unintentional islanding include supplying power that exceeds the acceptable limits for voltage, frequency, flickers and other power quality parameters; un-cleared faults due to unearthed operation leading to sustained fault currents; out-of-phase reclosing of circuit breakers; and electric shock as a result of touching live conductors assumed to be de-energized. Thus, unintentional islanding may cause malfunction or damage of network and customer equipment, or in the case of electric shock, lead to serious bodily injuries. Unintentional islanding occurs when the DG

interconnected to the grid does not realize loss-of-mains and continues to supply power to the grid [70]. It is necessary to have a means of detecting when unintentional islanding has occurred. If unintentional islanding is detected, it is necessary to disconnect the DG in order to prevent sustained operations under the undesired conditions.

Basically, there are two main types of anti- islanding detection methods - active anti-islanding detection and passive anti-islanding detection techniques. An Island occurs, and theoretically, remains undetectable if the Island's load is constant and exactly equal to real and reactive power output provided by the islands DG [71]. In practice, this scenario is unrealistic as loads are not constant and exact balance between DG supply and demand is unlikely. If there is a significant mismatch between the real and reactive power output of the DG and the island load demand, the voltage and frequency changes rapidly [71]. The island operation is terminated when the voltage and/or frequency reach preset under/over-voltage or frequency trip points. In general, the greater the difference between the DG supply and island load, the quicker the voltage or frequency deviation approaches the trip point [72]. Other characteristics that determine the time required to reach the trip point include the DG control characteristics, the voltage demand characteristics of the island's loads, and the mechanical inertia of the loads. When the DG is equipped with under and over-voltage and frequency relays, it is considered to employ basic passive anti-islanding techniques.

When it is not sufficient to base island detection on the imbalance between DG supply and island load demand, for example, in cases where the DG supply roughly matches load demand, then active anti-islanding methods are required. Active anti-islanding techniques have been developed to accelerate the resulting frequency and voltage deviations, such that the trip points are reached more rapidly [71, 72]. These active anti-islanding techniques modulate the real and reactive power output of the DG in response to changes in frequency and voltage magnitude. Active anti-islanding employing these techniques use positive feedback destabilizing control, where any randomly occurring changes in voltage or frequency is amplified. Under normal operating conditions, when the DG is interconnected with the grid, the output of the DG is small relative to the grid, and the invariance of the grid voltage and frequency will maintain stability. Once the grid is disconnected (loss-of-mains), the active anti-islanding makes the island inherently unstable and the DG is driven to the trip point.

3.4.2 Interconnection at the Point-of-Common Coupling

Voltage sags or momentary reductions in the rms voltage magnitude lasting between half a cycle and several seconds are usually caused by fault conditions on the power distribution system [73]. The starting of induction motors can also cause voltage sags on the power system although the effect of motor starts by itself should not pose any significant problems on a properly designed system. However, the combination of a fault condition on the system with the effect of motors starting or restarting can

significantly impact on the voltage stability of the power distribution system [74]. It is useful to briefly examine the dominant types of fault in terms of their magnitudes and durations.

A power system can either experience a short circuit fault or an open circuit fault. The short circuit fault occurs when a low impedance path is formed between phases or between a phase or phases and ground. This may result from insulation failure causing the current carrying conductor to be exposed to ground or other conductors. The low impedance path causes very high currents to flow which affects the voltage magnitude and may damage equipment. There are four different types of short-circuit faults that can occur on a three-phase system – three-phase, line-to-line, line-to-ground, and the double line-to-ground faults. Only the three-phase fault shown in Fig. 3.14 produces balanced voltages and currents. Open circuit faults typically result from fuse operation in one or more phases of a fuse-protected three-phase circuit. In this case, part of the system continues to operate in an unbalanced manner.

The primary reason to determine fault magnitudes and duration is to size protective devices; therefore it is only necessary to consider the fault type that produces the largest fault current, i.e. the worst case scenario. In most cases, the worst case is the three-phase fault [75], and as such, the three phase fault will be primarily considered in this work. It is important to point out that while the three-phase fault is often the most severe case, this assumption does not always apply [75, 76]. For power system planning

and design, all fault types should be analyzed to determine which produces the largest current when sizing protective devices.

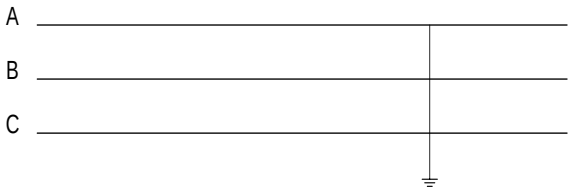

Fig. 3.14 Three-phase short circuit fault

The impact of the additional fault current supplied by each DG on the protective devices of nearby loads must be considered in determining the capacity of the DG. The effect of a nearby PV DG can damage protective equipment during a fault occurrence as illustrated in Fig. 3.15 where the circuit breaker on the load line exceeds its current limit and has to be replaced due to the additional fault current supplied by the DG.

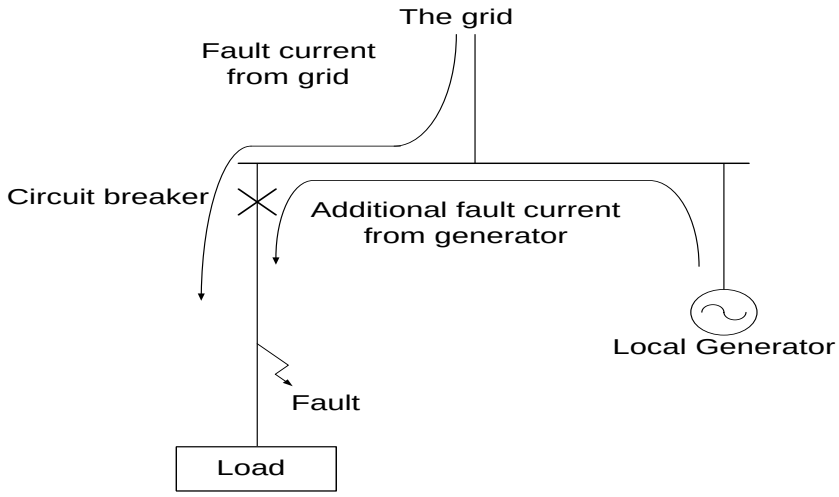

Fig. 3.15 Total fault current exceeds the limits of the circuit breaker [54]

In a DG-embedded power system, the addition of DGs to the power distribution network can cause the voltage at the PCC to rise to undesired levels. The ANSI (84.1-1995, Range A) prescribes a ± 10 % band around the nominal voltage of 120 V as the acceptable voltage range. The connection between a PV DG and the grid is represented by the equivalent circuit shown in Fig. 3.16.

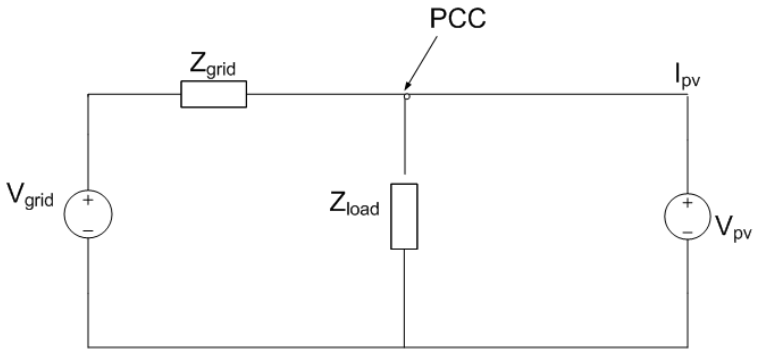

Fig. 3.16 Equivalent circuit of the PV-grid connection

The voltage at the PCC is given by:

$$V_{PCC} = \frac{Z_{load}}{Z_{grid}+Z_{load}}\left(V_{grid} + Z_{grid}I_{PV}\right) \tag{3.31}$$

Using eq. (3.14), the PV current limit that is necessary to hold the voltage at the PCC below a preset value (usually a nominal fraction of the grid voltage, nV_{grid}) is given as [77]:

$$I_{PV} \leq V_{grid}\left[\frac{n}{Z_{load}} + \frac{n-1}{Z_{grid}}\right] \tag{3.32}$$

The voltage profile relative to the transmission distance on a power system without DG is shown in Fig. 3.17. It is seen that the voltage profile keeps dropping as the power travels farther from the substation, and may eventually drop below acceptable limits (120V ± 10%) if no compensation is employed. Fig. 3.18 shows the case where a PV DG is present at the far end of the transmission line. Here, the voltage profile actually rises as the distance from the substation increases due to the contribution from the PV DG. The voltage can rise above acceptable limits if the power output of the PV exceeds the load absorption plus the line losses. This can occur when there is light load demand and the PV output is high (e.g. sunny day during the winter).

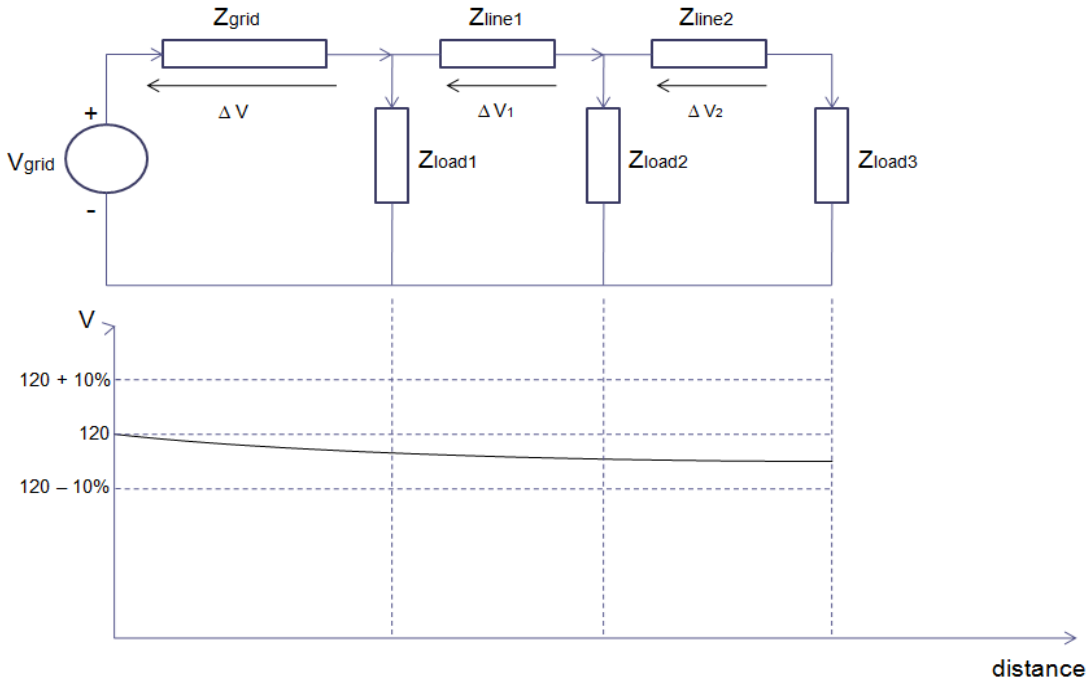

Fig. 3.17 Voltage profile relative to distance with no DG

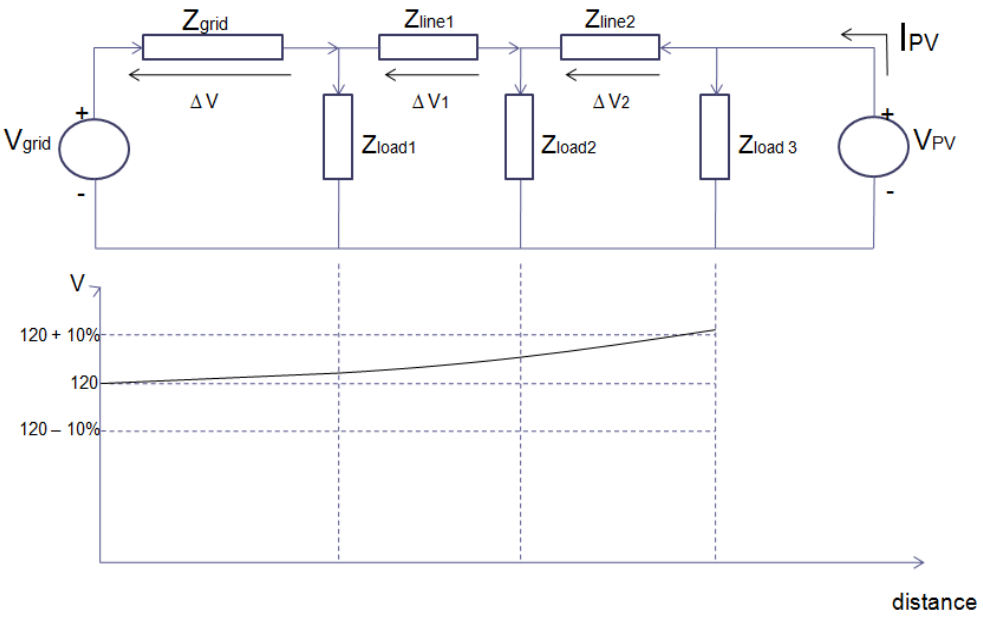

Fig. 3.18 Voltage profile relative to distance with DG

In order to limit the voltage rise experienced as a result of adding DGs to the power distribution network, a voltage feedback technique that limits the output of the DG based on the voltage at the PCC can be employed as an alternative to disconnecting the DG completely due to unacceptable voltage rise. A voltage feedback technique that accomplishes this task is presented in detail in Chapter 5.

4. ANALYTICAL APPROACH TO VOLTAGE INSTABILITY

The source side of the power system stability dynamic has been examined in the previous chapter, but it is well known that loads are the main driver of voltage instability. Induction motors are the typical loads found in the industrial sector, and the impact of these motor loads on the power system stability is investigated in this chapter. The voltage-power characteristic of induction motor loads is used to define the loadability limit for an industrial power system and bifurcation theory is applied to determine the short-term and long-term margins to voltage instability. Bifurcation theory deals with the emergence of sudden changes in system response due to smooth variations in system parameters - an effect which is similar to voltage instability or collapse. The system components are implemented in Matlab and the voltage stability scenarios are investigated for both the short-term and long-term cases.

4.1 Voltage Instability Mechanism

Voltage instability occurs when the power system is unable to maintain steady voltages at all buses. This stems from the attempt of load dynamics to restore power consumption beyond the capability of the power system [54]. A power system subjected

to a disturbance may be unable to return to a state of equilibrium once the maximum transferrable power limit has been reached and the operation of automatic load restoration devices push the system towards voltage instability. In this state, the load restoration mechanism leads to a reduction in power consumed rather than the expected increase in power consumption; this is a definite indication of voltage instability [78]. The load is the main driver of this form of instability. Consider the one-line diagram of a power system including an interconnected industrial microgrid shown in Fig. 4.1, where the total load of all the induction motors in the microgrid is represented with a single motor at the PCC bus, and other loads are represented with a static load.

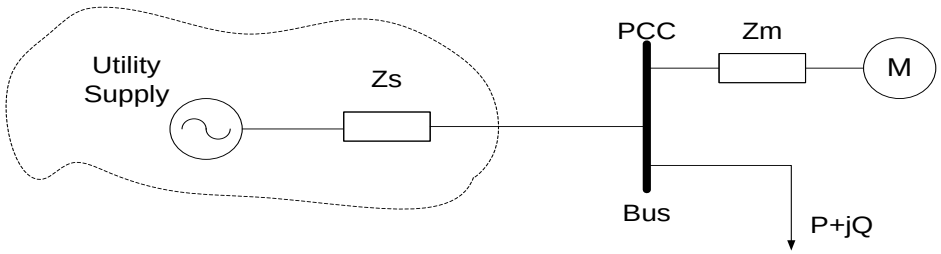

Fig. 4.1 One line diagram of the industrial microgrid

As shown earlier in Section 3.1, the real and reactive powers absorbed by the load is

$$P = -\frac{EV}{X}\sin\theta \qquad \text{[W]} \tag{4.1}$$

$$Q = -\frac{V^2}{X} + \frac{EV}{X}\cos\theta \qquad \text{[VAR]} \tag{4.2}$$

Eqs. (4.1) and (4.2) represent the load flow equations of the simplified microgrid shown in Fig. 4.1 where *X* is the Thevenin equivalent impedance. Solving the load flow equations for the condition to have at least one solution results in [54]:

$$-P^2 - \frac{E^2}{X}Q + \left(\frac{E^2}{2X}\right)^2 \geq 0 \tag{4.3}$$

The maximum power transfer limits for the real and reactive powers can be determined by setting *Q* and *P* to zero in eq. (4.3) respectively,

For *Q* = 0,

$$P \leq \frac{E^2}{2X} \tag{4.4}$$

For *P* = 0,

$$Q \leq \frac{E^2}{4X} \tag{4.5}$$

where $\frac{E^2}{X}$ is equal to the short-circuit power at the load.

From eqs. (4.4) and (4.5) above, the maximum real power that can be consumed at the load is half the short-circuit power while the maximum reactive power that can be consumed is a fourth of the short-circuit power. Therefore, for a system operating at or near peak load conditions, a sudden rise in reactive power demand (e.g. due to voltage sag) is accompanied by an increase in the real power consumption. Under the stressed conditions of peak load demand, there is usually insufficient power transfer capability

available in the power system which can lead to critical loads being dropped in order to maintain the overall system voltage stability. The difficulty in transferring large amounts of reactive power on the power transmission system is highlighted by eq. (4.5).

4.2 Voltage Sag Effects on Induction Motor Loads

Induction motors comprise a significant part of the load distribution for most industrial areas and they have a significant effect on the power system voltage stability. The load characteristic of the induction motor is the reason why it plays such a critical role in voltage stability. Those characteristics include the tendency to quickly restore loads (typically < 1s) and operating with a low power factor with a high reactive demand. It is also prone to stalling when the load is increased or the voltage level is not sufficiently high [79].

The steady-state equivalent circuit of the induction motor is shown in Fig. 4.2:

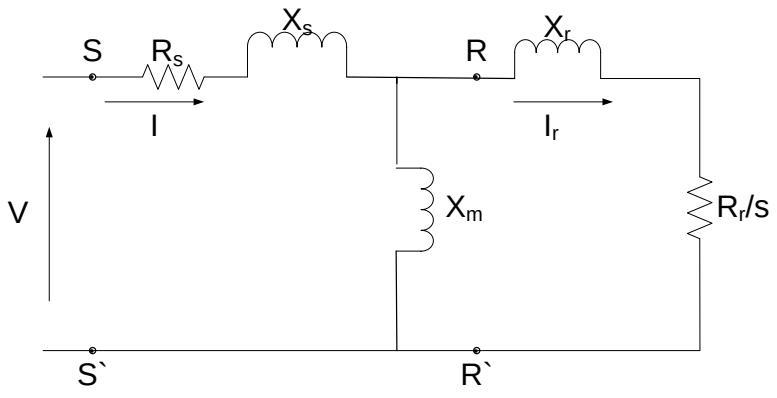

Fig. 4.2 Equivalent circuit of an induction motor

where R_S, X_S, R_R, X_R, and X_M are the stator, rotor and magnetizing resistances and reactances respectively. The motor slip, S, is related to the difference in speed between the rotor and the magnetic field generated by the stator:

$$S = \frac{\omega_0 - \theta_r}{\omega_0} \tag{4.6}$$

where ω_0 is the nominal angular frequency and ϑ_r is the rotor speed.

The equivalent circuit of the induction motor can be simplified further into a Thevenin circuit as shown in Fig. 4.3:

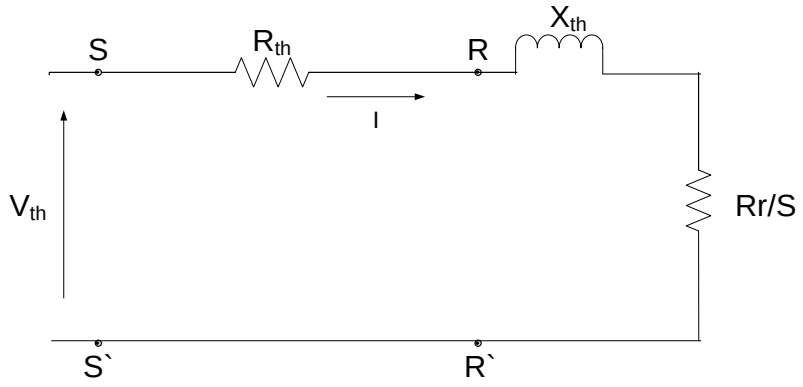

Fig. 4.3 Thevenin equivalent circuit of the induction motor

The Thevenin voltage when considered from the rotor terminals RR' is

$$V_{th} = \frac{X_m V}{\sqrt{R_S^2 + (X_S + X_m)^2}} \tag{4.7}$$

$$R_{th} + jX_{th} = \frac{jX_m(R_S + jX_S)}{R_S + j(X_S + X_m)} + jX_r \tag{4.8}$$

The current drawn by the motor in terms of the stator and electrical impedances when considered from the stator terminals SS' is

$$I = \frac{V}{(R_s+R_e)+j(R_e+X_e)} \tag{4.9}$$

where,

$$R_e + jX_e = \frac{jX_m\left(\frac{R_r}{s}+jX_r\right)}{\frac{R_r}{s}+j(X_m+X_r)} \tag{4.10}$$

The rotor and stator in an induction machine are separated by an air-gap that allows the free rotation of the rotor. The air-gap power, P_g, depends on the motor parameters and the slip for any given terminal voltage. The per unit air-gap power is equal to the developed electrical torque, T_e, of the motor.

The air-gap power in the induction motor is equal to the power absorbed by the resistance $\frac{R_r}{s}$ and can be expressed as [80]:

$$P_{ag} = \frac{R_r}{s} I_r^2 \tag{4.11}$$

The electrical torque developed in the Thevenin equivalent circuit is given as a function of the voltage V_{th} and slip by

$$T_e = \frac{V_{th}^2 \frac{R_r}{s}}{\left(R_{th}+\frac{R_r}{s}\right)^2+(X_{th}+X_r)^2} \tag{4.12}$$

The differential equation of the rotor motor in terms of slip is [80]:

$$\frac{ds}{dt} = \frac{1}{2H}(T_m - T_e) \tag{4.13}$$

where *H* is the inertia constant and T_m is the mechanical torque.

The torque equilibrium condition occurs when $T_e = T_m$. The real and reactive power absorbed by the induction motor at steady-state (equilibrium condition) is given as functions of voltage and slip by [54]

$$P = \frac{(R_s+R_e)V^2}{(R_s+R_e)^2+(X_s+X_e)^2} \tag{4.14}$$

$$Q = \frac{(X_s+X_e)V^2}{(R_s+R_e)^2+(X_s+X_e)^2} \tag{4.15}$$

The slip-torque characteristic for the induction motor is shown in Fig. 4.4:

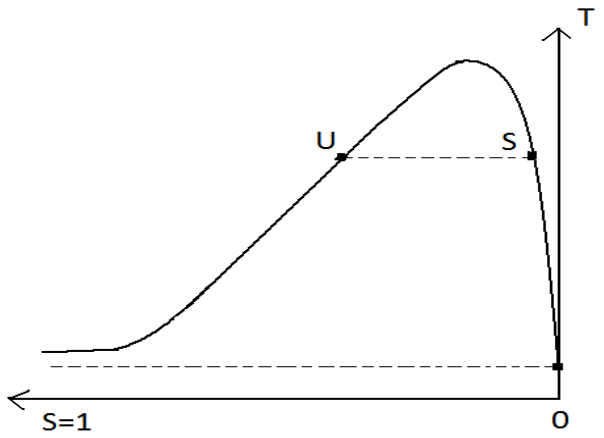

Fig. 4.4 Slip-torque characteristic for an induction motor

The three types of induction motor models - the constant torque model, the quadratic torque model, and the composite torque model – that are typically found in the industrial sector and exhibit different steady-state behaviors under different torques are used in this study and are briefly presented next. Some industrial motors exhibit the constant torque characteristic although the majority of industrial motors are more closely represented by the quadratic and composite torque models [81, 82].

In the constant torque model, the mechanical torque is parallel to the *s*-axis. The motor stalls when the mechanical torque exceeds the maximum available electrical torque. *PV* and *QV* curves can be used to express the relationship between the consumed power and the terminal voltage and they are typically used to assess the voltage stability of power systems. The constant mechanical torque is given as [82]:

$$T_m = T_0 = k \tag{4.16}$$

The *PV* and *QV* curves for a constant torque model using eqs. (4.1) and (4.2) are shown in Fig. 4.5.

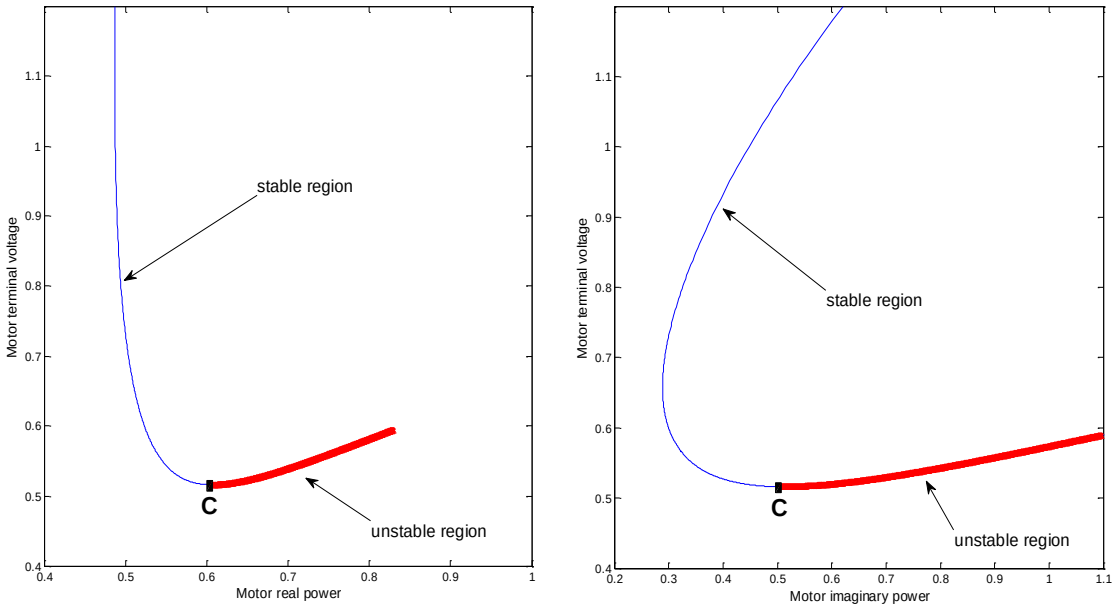

Fig. 4.5 *PV* and *QV* curves for constant torque model

For any operating point for which the mechanical torque is less than the maximum electrical torque, there are two operating points: the higher point on the curve corresponds to the normal operating condition, characterized by higher voltage and lower current while the lower point characterized by lower voltage and higher current represents an abnormal operating condition. The operating points to the left of point C are stable and the real power consumption is almost constant. The stalling point is C, while the operating points to the right of the stalling point are unstable. The reactive power characteristic shows that the reactive power consumption increases rapidly as the operating point moves towards the stalling point.

The quadratic torque model is sometimes used when the constant torque model is insufficient to represent the motor. The quadratic mechanical torque characteristic is given by [82]:

$$T_m = T_{syn}(1 - s)^2 \tag{4.17}$$

where T_{syn} is the synchronous speed torque (i.e., when s = 0).

The *PV* and *QV* curves for the quadratic model are shown in Fig. 4.6. The stable operating points are to the right of the stalling point in the real power curve while the stable operating points lie in the upper regions of the reactive power curve.

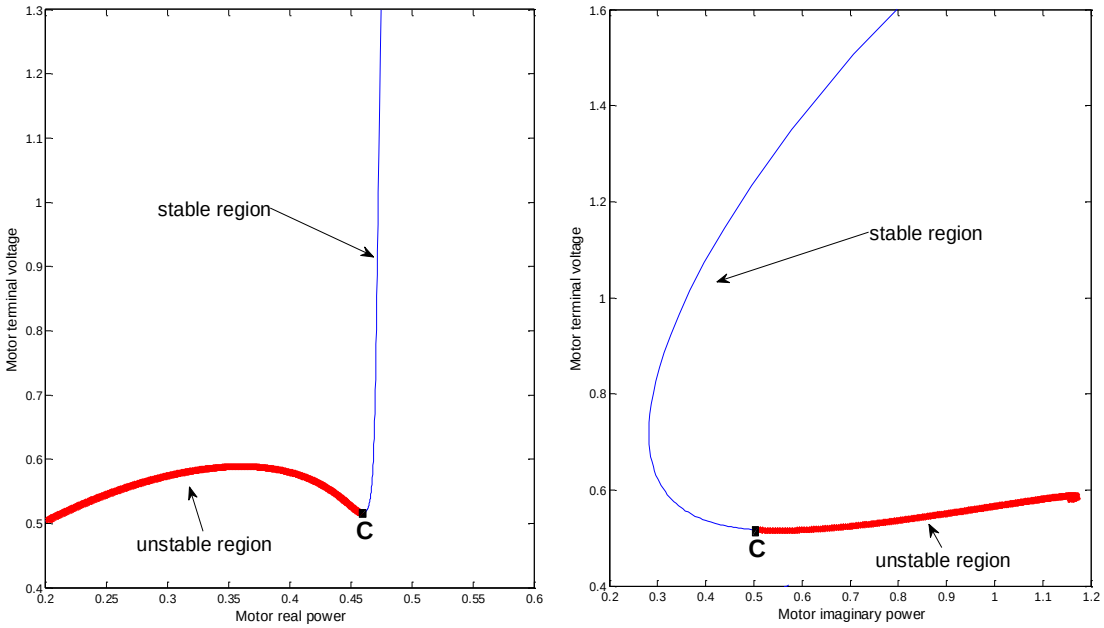

Fig. 4.6 *PV* and *QV* curves for the quadratic torque model

The composite torque model is a combination of the constant torque model and the quadratic model. It takes into account the static torque due to friction. The composite torque characteristic is given by [82]:

$$T_m = T_0 + T_s s + T_2 \tag{4.18}$$

where T_s is the static torque.

The composite torque model is useful when the combination of the various motor loads exhibit different characteristics. A single induction load model can be used to represent the cumulative effect of all the motors in an industrial facility, which may include several tens or even hundreds of small, medium, and large sized motors that exhibit similar characteristics. The cumulative load characteristic is the expression of the active and reactive powers of all the loads as a function of voltage and load demand. The exponential load model is given as [54]:

$$P = cP_0 \left(\frac{V}{V_0}\right)^a \tag{4.19}$$

$$Q = cQ_0 \left(\frac{V}{V_0}\right)^b \tag{4.20}$$

where P_0 and Q_0 is the real and reactive consumed power respectively at the nominal voltage V_0, while a and b are the load power sensitivities to voltage, and c is the cumulative load demand.

The equations in (4.19) and (4.20) are the general representations of the exponential load model. The load power sensitivities *a* and *b* represent the relationship of the load voltage to the real and reactive powers respectively. When the power consumed is constant and independent of voltage, as in the case of a constant power load model, the load power sensitivities to voltage is zero and thus $a = b = 0$. For a constant current load model, the consumed power is proportional to the voltage and $a = b = 1$. In a constant impedance load model, the consumed power is proportional to the square of the load voltage and $a = b = 2$. A table of the load power sensitivities for some industrial loads is shown in Table 4.1.

TABLE 4.1 Load power sensitivities for common industrial loads

Load component	*a*	*B*
Central air conditioners	0.09	2.5
Fluorescent lights	0.96	7.4
Industrial motors	0.07	0.5
Industrial pumps	1.4	1.4
Transformers (unloaded)	3.4	11.5

The two types of generalized load model typically used are the multiplicative load model given in eqs. (4.19) and (4.20) and the additive load model given in eqs. (4.21) and (4.22). In the multiplicative model, the load state variable multiplies the load

characteristic while the load state variable is added to the load characteristic in the additive load model [54].

$$P = P_0 \left[\left(\frac{V}{V_0} \right)^a + c \right] \tag{4.21}$$

$$Q = Q_0 \left[\left(\frac{V}{V_0} \right)^b + c \right] \tag{4.22}$$

The multiplicative constant impedance load model, with $a = b > 1$, is used in this study as it captures the effect of self-restoring loads that are the main drivers of voltage instability. The network and load characteristic for the multiplicative constant impedance load model is shown in Fig. 4.7. The network characteristic is the projection of all the possible operating points of the cumulative demand on to the *PV* and *QV* planes respectively.

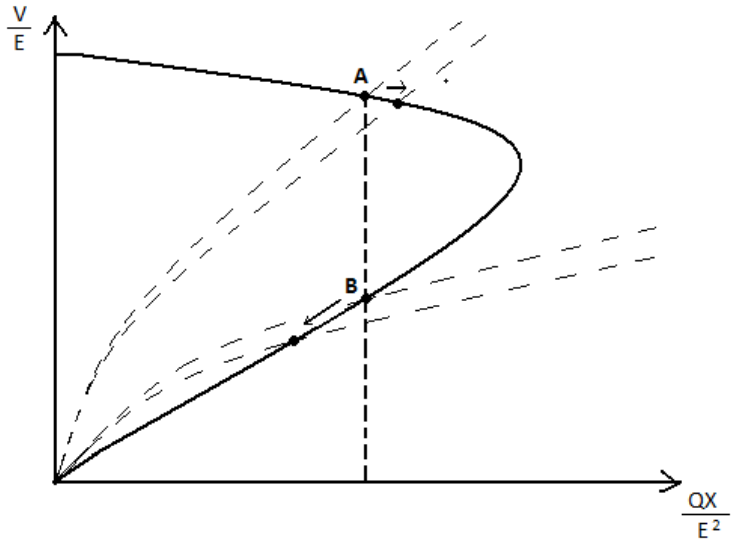

Fig. 4.7 Network characteristic and load *QV* curves

Consider that the motor load in Fig. 4.1 is represented by the constant impedance model and it is now operating in steady-state. During normal operation, a small increase in the load demand should result in some voltage drop along with increased load power as shown at point A in Fig. 4.7. However, if the operating point is at point B, then a small increase in load demand results in a drop in voltage as well as a drop in load power. For loads with self-restoration devices operating at point B, the tendency to increase load demand to meet a specific power consumption will keep the operating point in the unstable region and likely lead to voltage instability. The dashed vertical line in the steady-state characteristic of the constant impedance load model shown in Fig. 4.7 represents the operating point at equilibrium. Voltage instability occurs when changes in the system parameters (such as voltage sags or faults) cause the load equilibrium point to shift to the right or the network characteristic to shrink until the load equilibrium point no longer intersects the network characteristic. For microgrid operation, it is necessary to ensure that the load equilibrium point will always intersect the network characteristic in order to avoid detrimental voltage effects on the wider power system.

4.3 Bifurcation Analysis

Voltage instability results mainly from the inability of a stressed power system to meet the reactive power demand required to maintain the desired voltage levels at all buses in the system [38]. The power system can experience two types of voltage instabilities –

voltage collapse and unstable voltage oscillation. The power system experiences voltage collapse if it is unable to maintain acceptable steady-state voltages after a disturbance event [37]. Unstable voltage oscillation usually results from the interaction of controllers with power system equipment.

Voltage instability occurs on multiple timescales, and can be classified into short-term and long-term instabilities. Short-term voltage stability refers to the small-signal and transient stabilities, including the stability of the dynamics of induction motors and controllers. Long-term voltage stability refers to the long-term dynamics, including dynamic stabilities due to generator excitation limit and load increase.

The dynamics and changes in operating condition of the power system can be represented by differential and algebraic equations respectively. The dynamics that result due to changes in operating condition can be decomposed into slow and fast dynamics based on the time-scale of interest. The corresponding state variables can similarly be decomposed into slow and fast variables [83].

Any power system can be described by the set of differential-algebraic equations (DAE) shown in eqs. (4.23) and (4.24).

$$\dot{\boldsymbol{x}} = \boldsymbol{f}(\boldsymbol{x}, \boldsymbol{y}) \tag{4.23}$$

$$\boldsymbol{0} = \boldsymbol{g}(\boldsymbol{x}, \boldsymbol{y}) \tag{4.24}$$

The differential equation in eq. (4.23) can be decomposed to separate the slow state variables X_s from the fast state variables X_f, resulting in eqs. (4.25) and (4.26) respectively.

$$\dot{\boldsymbol{x}}_{\boldsymbol{s}} = \boldsymbol{f}_{\boldsymbol{s}}(\boldsymbol{x}_{\boldsymbol{s}}, \boldsymbol{x}_{\boldsymbol{f}}, \boldsymbol{y}) \tag{4.25}$$

$$\alpha\dot{\boldsymbol{x}}_{\boldsymbol{f}} = \boldsymbol{f}_{\boldsymbol{f}}(\boldsymbol{x}_{\boldsymbol{s}}, \boldsymbol{x}_{\boldsymbol{f}}, \boldsymbol{y}) \tag{4.26}$$

where α is generally a very small number.

When α approaches zero, the differential equation of the fast state vector in eq. (4.26) can be approximated by the algebraic equation shown in eq. (4.27). In this case, eqs. (4.28) and (4.29) complete the approximation of the power system described by eqs. (4.23) and (4.24).

$$\dot{\boldsymbol{x}}_{\boldsymbol{s}} = \boldsymbol{f}_{\boldsymbol{s}}(\boldsymbol{x}_{\boldsymbol{s}}, \boldsymbol{x}_{\boldsymbol{f}}, \boldsymbol{y}) \tag{4.27}$$

$$\mathbf{0} = \boldsymbol{f}_{\boldsymbol{f}}(\boldsymbol{x}_{\boldsymbol{s}}, \boldsymbol{x}_{\boldsymbol{f}}, \boldsymbol{y}) \tag{4.28}$$

$$\mathbf{0} = \boldsymbol{g}(\boldsymbol{x}_{\boldsymbol{s}}, \boldsymbol{x}_{\boldsymbol{f}}, \boldsymbol{y}) \tag{4.29}$$

The non-linear nature of power system means that non-linear analysis techniques such as bifurcation analysis are required for power system voltage stability studies. Bifurcation theory deals with the emergence of sudden changes in system response due to the slow variation of smooth continuous system parameters [84]. With timescale decomposition applied to the power system to separate slow and fast variables,

bifurcation analysis describes the qualitative changes of stability with smooth parameter variations [83].

Using timescale decomposition, the DAE of the power system can be represented by eqs. (4.27 – 4.29). If the slow variables X_s are considered as parameters, the power system voltage stability analysis can be performed using the system dynamics represented by the set of parameter dependent DAE shown in eqs. (4.30) and (4.31) [83].

$$\dot{\boldsymbol{x}} = \boldsymbol{f}(\boldsymbol{x}, \boldsymbol{y}, \boldsymbol{p}) \tag{4.30}$$

$$0 = \boldsymbol{g}(\boldsymbol{x}, \boldsymbol{y}, \boldsymbol{p}) \tag{4.31}$$

where ***x*** is a vector of state variables, ***y*** is a vector of algebraic variables, and ***p*** is a vector of parameters.

Solving the DAE shown in eqs. (4.30) and (4.31) for a power system is non-trivial. In order to simplify the analysis, the algebraic vector ***y*** can be eliminated from eq. (4.30) by solving for ***y*** in terms of the state vector ***x*** and parameter vector ***p*** in eq. (4.31) which results in the reduced differential equation below:

$$\dot{\boldsymbol{x}} = \boldsymbol{F}(\boldsymbol{x}, \boldsymbol{p}) \tag{4.32}$$

The equilibrium points for a system described by eqs. (4.30) and (4.31) are given as

$$\boldsymbol{0} = \boldsymbol{F}(\boldsymbol{x}, \boldsymbol{p}) \tag{4.33}$$

Depending on the size of the power system and the order of the differential equations, eliminating the algebraic variables from the set of DAE can be a complex task. In such cases, linearization is applied to obtain a localized approximation of the dynamic properties around an equilibrium point [83]. The non-linear system described by eqs. (4.30) and (4.31) can be approximated around each equilibrium point by the linearized model shown in eq. (4.34).

$$\begin{bmatrix} \Delta\dot{\boldsymbol{x}} \\ \mathbf{0} \end{bmatrix} = \boldsymbol{J} \cdot \begin{bmatrix} \Delta\boldsymbol{x} \\ \Delta\boldsymbol{y} \end{bmatrix} \tag{4.34}$$

where $\boldsymbol{J}$ is the unreduced Jacobian of the DAE system:

$$\boldsymbol{J} = \begin{bmatrix} \boldsymbol{f_x} & \boldsymbol{f_y} \\ \boldsymbol{g_x} & \boldsymbol{g_y} \end{bmatrix} = \begin{bmatrix} \frac{\partial f}{\partial x} & \frac{\partial f}{\partial y} \\ \frac{\partial g}{\partial x} & \frac{\partial g}{\partial y} \end{bmatrix} \tag{4.35}$$

If $\boldsymbol{g_y}$ is assumed to be nonsingular, $\boldsymbol{\Delta y}$ can be eliminated from eq. (4.34) to obtain the reduced model:

$$\Delta\dot{\boldsymbol{x}} = \left[\boldsymbol{f_x} - \boldsymbol{f_y}\boldsymbol{g_y^{-1}}\boldsymbol{g_x}\right]\Delta\boldsymbol{x} \tag{4.36}$$

The state matrix $\boldsymbol{A}$ of the linearized system is obtained as:

$$\boldsymbol{A} = \left[\boldsymbol{f_x} - \boldsymbol{f_y}\boldsymbol{g_y^{-1}}\boldsymbol{g_x}\right] \tag{4.37}$$

In power system studies, the state matrix $\boldsymbol{A}$ is often called the reduced Jacobian $\boldsymbol{J_r}$. The system equilibrium points can be continuously solved for the smooth slowly varying parameter $\boldsymbol{p}$. The dynamic properties of the system can be analyzed for each

equilibrium point using the reduced Jacobian $\boldsymbol{J}_r$. At the bifurcation points, the qualitative structure of the power system described by eqs. (4.30) and (4.31) undergoes sudden changes through small perturbations of the parameters [84].

The two types of bifurcations that are expected for a power system described by a single family of ODEs are the saddle-node bifurcations (SNB) and Hopf Bifurcations. The SNB is the point where two equilibrium points (or two branches of equilibria) coalesce and then disappear. At the bifurcation, one of the equilibrium points has a real positive and the other a real negative eigen value and the state Jacobian becomes singular with a zero eigen value [85]. Hopf bifurcation deals with oscillatory instability at the bifurcation point.

The network and load characteristic for a power system is shown in Fig. 4.8. Assuming the load has a constant power characteristic, the reactive power consumption increases from Q_1 to Q_2 due to an increase in the load. The system equilibrium points occur at the intersection of the load and network curves. The equilibrium points for the load at Q_1 occur at *S* and *U*, with the upper point *S* the stable equilibrium while point *U* is the unstable equilibrium. When the load is increased to Q_2, the stable and unstable equilibrium points meet at point *C*. This indicates the occurrence of an SNB, and the voltage at point *C* is the voltage stability limit.

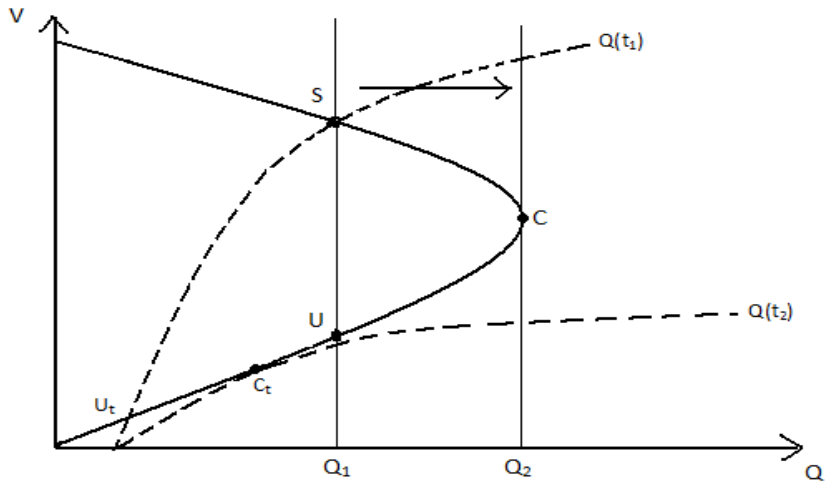

Fig. 4.8 Network *QV* curve indicating SNB [86]

The dotted lines in Fig. 4.8 correspond to the transient load characteristics that describe the dynamics of fast variables. The transient load curve at the stable equilibrium point is $Q(t_1)$ and it intersects the network curve at points S and U_t. Depending on the time constant of the fast dynamics, the transient load curve may shift to $Q(t_2)$ where the two equilibrium points meet at C_t. The system thus experiences SNB during the transient period at the voltage stability limit corresponding to C_t.

The Hopf bifurcation is the point where there is an emergence of oscillatory instability, and at such point, a pair of complex eigen values of the Jacobian cross the imaginary axis in the complex plane [87]. At the Hopf bifurcation a power system at steady-state typically starts to oscillate. The stability of the system initially at equilibrium is lost due to its interaction with the limit cycle in the vicinity of the Hopf bifurcation.

The network and load characteristics for a power system are shown in Fig. 4.9. The eigen values of the reduced Jacobian matrix for each point on the load QV curve is calculated, and when the imaginary parts of a pair of complex eigen values become positive, the system experiences Hopf bifurcation. This occurs at point S_{hb} in Fig. 4.9 when the load increases from Q_1 to Q_2. The voltage at S_{hb} is the voltage stability limit. Similarly, the transient load characteristic can induce Hopf bifurcation when the transient load curve leaves the region of attraction of point S_{hb} and tends towards the unstable equilibrium *U*.

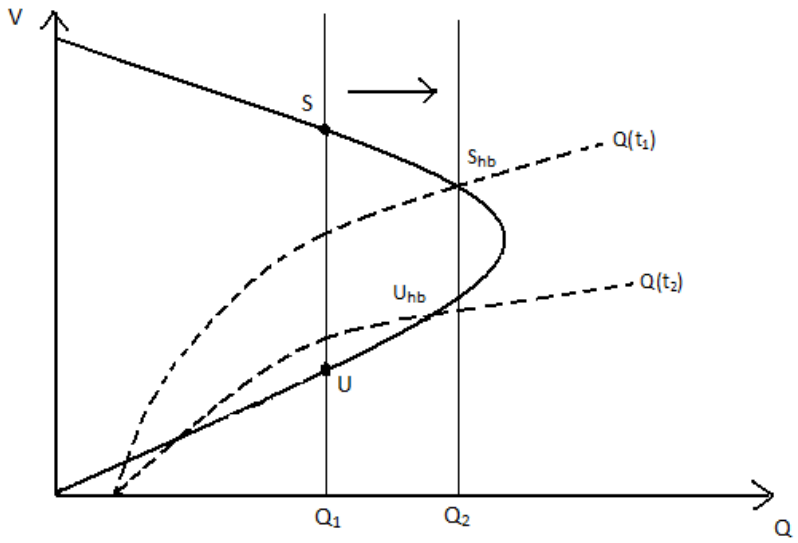

Fig. 4.9 Network *QV* curve indicating Hopf bifurcation [86]

The SNB and Hopf bifurcation sets form the boundary of the stable operating region of the microgrid. The system loses its equilibrium point when the operating point crosses that boundary [88].

The DAE model of the power system is used to describe the dynamics of the power system for voltage stability analysis.

$$\dot{\boldsymbol{x}} = \boldsymbol{f}(\boldsymbol{x}, \boldsymbol{p}) \tag{4.38}$$

$$\mathbf{0} = \boldsymbol{g}(\boldsymbol{x}, \boldsymbol{p}) \tag{4.39}$$

where ***x*** is the vector of dynamic state variables that typically describe time-dependent generator voltages and ***p*** is the vector of parameters that define a specific system configuration and operating condition.

For every value of ***p***, the system equilibrium points are given by the solution of eq. (4.39). The algebraic equations in eq. 4.39 are the power flow equations representing the real and reactive power balances at the load buses, and it defines an equilibrium manifold in the state and parameter dimensional space [88]. Bifurcation may occur at any point along the path of the smooth parameter variations. Bifurcation occurs at the loadability limit of a power system resulting in voltage instability.

Loads are the main driver of voltage instability and the loadability limit for a power system is defined as the point where the load characteristic becomes tangent to the network characteristic. Bifurcation analysis can be applied to determine the loadability limit induced bifurcation of a microgrid, provided the load and network models are fairly well described. For the generalized exponential load model, the consumed real and reactive powers that define the load characteristic are [54]:

$$-\frac{EV}{X}\sin\theta = cP_0\left(\frac{V}{V_0}\right)^2 \tag{4.40}$$

$$-\frac{V^2}{X}+\frac{EV}{X}\cos\theta = cQ_0\left(\frac{V}{V_0}\right)^2 \tag{4.41}$$

Dividing the power equation by V to get the load current results in

$$-\frac{E}{X}\sin\theta = cP_0\left(\frac{V}{V_0^2}\right) \tag{4.42}$$

$$-\frac{V}{X}+\frac{E}{X}\cos\theta = cQ_0\left(\frac{V}{V_0^2}\right) \tag{4.43}$$

Solving eqs. (4.42) and (4.43) results in a single solution V for every value of the cumulative load c, and therefore there is no loadability limit resulting from the bifurcation of the load operating point for a microgrid consisting of mainly exponential-type loads ($a = b > 1$). Instead the loadability limit for such microgrid is bounded by the permissible voltage rise (or drop) at the PCC bus. In the case where the loads are less sensitive to voltage than constant current ($a = b < 1$), there is a maximum value of c that corresponds to the maximum loadability, c_m, where there are two solutions for $c < c_m$ and no solutions for $c > c_m$.

For a power system described by

$$\boldsymbol{\varphi}(\boldsymbol{y}, \boldsymbol{c}) = \mathbf{0} \tag{4.44}$$

where $\boldsymbol{\varphi}$ corresponds to the steady-state network equations when both the short-term and long-term dynamics are considered constant and $\boldsymbol{c}$ corresponds to the load demand.

The Jacobian $\boldsymbol{\varphi_y}$ of the steady-state equations is singular at the loadability limit, L_m.

$$\det \boldsymbol{\varphi_y} = 0 \tag{4.45}$$

The steady-state equations from eqs. (4.40) and (4.41) for the exponential load model are given in terms of the load current as

$$-\frac{E}{X}\sin\theta + cP_0\left(\frac{V}{V_0^2}\right) = 0$$

$$-\frac{V}{X} + \frac{E}{X}\cos\theta + cQ_0\left(\frac{V}{V_0^2}\right) = 0$$

When the nominal operating voltage is assumed to be 1 p.u., i.e. V_0 = 1 p.u., the Jacobian of the system is

$$\varphi_y = \begin{bmatrix} \frac{EV}{X}\cos\theta & cP_0(2V)\frac{E}{X}\sin\theta \\ \frac{EV}{X}\sin\theta & cQ_0(2V) + \frac{2V}{X} - \frac{E}{X}\cos\theta \end{bmatrix} \tag{4.46}$$

The corresponding singularity condition of φ_y is

$$E + cP_0(2V)\sin\theta - (cQ_0(2V) + 2V)\cos\theta \tag{4.47}$$

or

$$E + cP_0(2V)\sin\theta - 2V(1 + cQ_0)\cos\theta \tag{4.48}$$

The singularity condition above along with an initial given combination of P_0 and Q_0 determine the maximum loadability c_m and the corresponding V and ϑ. From these values, the load power consumption P and Q for c_m can be calculated. The difference in the actual load power consumption to the power consumption at c_m is the loadability margin. When the real or reactive power consumption by the load exceeds the corresponding real or reactive power consumption at c_m, corrective action must be taken to restore the load operating to a stable operating point.

Consider the study system of Fig. 4.10 consisting of the utility power supply and an industrial microgrid with a local PV source. The utility power supply is assumed to be a synchronous generator with over-excitation limiters (OXL) and automatic voltage regulators (AVR), the local DG is a photovoltaic generator, and the load is assumed to be a three-phase induction motor load.

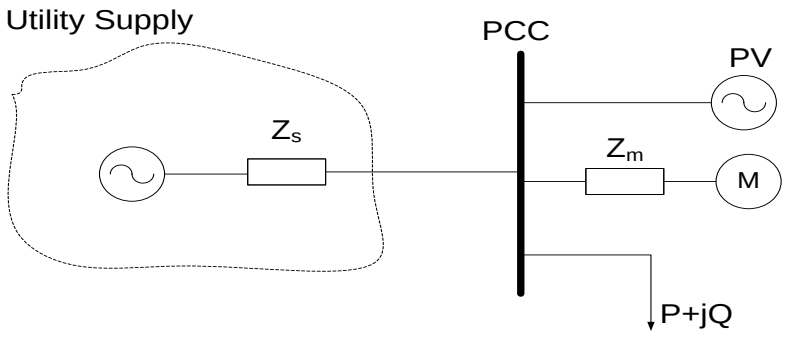

Fig. 4.10 Study system including local PV generator

The system can be represented by the sets of differential equations below:

$$\frac{dF_q}{ds} = \frac{1}{T_{oc}}\left[F_f - F_q - (\omega L_d - \omega L'_d) i_d\right] \tag{4.49}$$

$$\frac{dF_f}{ds} = \frac{G}{T}\left(V_0 - V_g\right) - F_f \tag{4.50}$$

$$\frac{ds}{dt} = \frac{1}{2H}\left(T_m - T_e\right) \tag{4.51}$$

$$\frac{dP_{pv}}{dV_{pv}} = I_{pv} + V_{pv}\left(\frac{\partial I_{pv}}{\partial V_{pv}}\right) \tag{4.52}$$

where F_q and F_f are the transient reactance emf and field voltage emf of the generator respectively. T_{oc} is the open-circuit transient time constant, L_d is the winding self inductance, L'_d is the transient self winding inductance and id is the current produced by the generator. *G* and *T* are characteristics of the OXL and AVR of the generator while V_0 and V_g are the reference voltage of the AVR and the terminal voltage of the generator respectively.

The loadability limit, L_m, determined by the SNB and Hopf bifurcation surface, is defined in terms of the real and reactive power demands of the system. The bifurcation conditions for an industrial microgrid are examined separately for the short-term and long-term models since the dynamics of the power system evolve over different timescales.

4.3.1 Short-Term Voltage Instability

The approximate short-term dynamic model is given by:

$$\dot{\boldsymbol{x}} = \boldsymbol{f}(\boldsymbol{x}, \boldsymbol{y}, \boldsymbol{p}) \tag{4.53}$$

$$\boldsymbol{0} = \boldsymbol{g}(\boldsymbol{x}, \boldsymbol{y}, \boldsymbol{p}) \tag{4.54}$$

Here, *y* is the vector of state variables describing the microgrid load bus voltages and angles. As shown earlier, a necessary condition for the loadability limit of the microgrid, assuming the state variables are fixed, is the singularity of g_y. For a microgrid consisting primarily of induction motors fitting the exponential load model ($a = b > 1$), as is usually the case industrial microgrids, then there is a single solution for every value of the cumulative load demand in eq. (4.43) and there is no loadability limit. In this case, one can apply the implicit function theorem to eq. (4.53) [84] to get:

$$\dot{x} = f(x, p) \tag{4.55}$$

The equilibrium conditions of eq. (4.53) for a fixed *p* are

$$f(x, y, p) = 0 \tag{4.56}$$

$$g(x, y, p) = 0 \tag{4.57}$$

At the equilibrium, the unreduced Jacobian is

$$J = \begin{bmatrix} f_x & f_y \\ g_x & g_y \end{bmatrix} \tag{4.58}$$

Recalling that the necessary condition for SNB is the singularity of the state Jacobian, the singularity of the unreduced Jacobian is the condition that induces the SNB of the short-term dynamics. This coincides with the necessary condition for the loadability limit when the system is in steady-state.

The short-term model considers the dynamics of fast-acting devices only, and assumes that the slowly varying parameters are in steady-state. Some power system components whose dynamics involve in the short-term time scale include synchronous generators, automatic voltage regulators (AVRs), induction motors, HVDC components and static VAR compensators (SVCs).

Short-term voltage instability can result from voltage sags due to the starting or reacceleration of motors. During startup, the motor impedance consists of the winding resistance in series with the inductive reactance, but the resistance is usually neglected since it is much smaller than the reactance. Before the motor is energized, the rotor is at a standstill and there is no counter-emf. However, as the rotors start to accelerate, a counter-emf builds, effectively reducing the voltage across the motor windings and thus limiting the current as shown in Fig. 4.12. As a result, the starting current is much smaller than the running current and can typically be up to 5 or 6 times larger in magnitude [71].

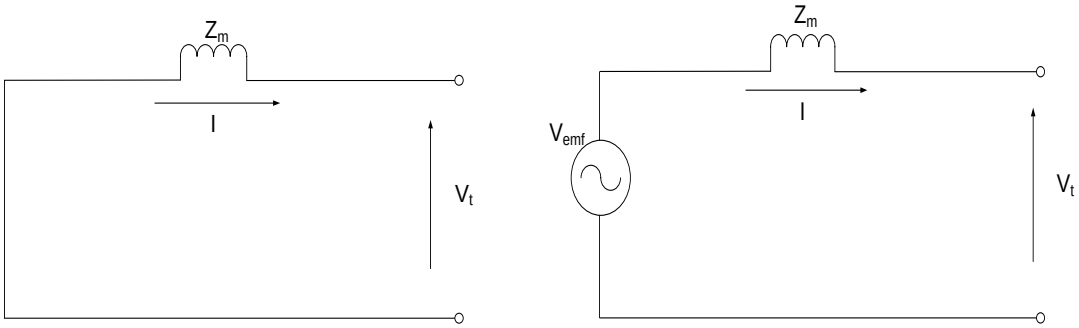

(a) (b)

Fig. 4.11 Equivalent circuit of a) starting motor and b) running motor

$$I = \frac{V_t - V_{emf}}{Z_M} \tag{4.59}$$

A similar effect occurs when there is a fault condition on the power system. At the onset of a fault, the protective devices (relays, circuit breakers, etc) in the power system operate to isolate the fault. This causes the voltage in the affected areas where the circuit breakers have tripped to approach zero. The induction motors start to slow down but do not stop immediately due to their mechanical inertia. The time constant for a loaded motor can be up to 10 seconds, so if power is not restored to the motor terminals quickly enough, the motors have to be allowed to slow down significantly before reaccelerating to prevent "*out-of-phase*" reclosing.

When a three-phase fault occurs, the loss of power causes the voltage at the motor terminals to drop. This causes as imbalance between the magnetic flux in the air gap and the stator voltage. The flux decay can take up to several seconds, and during the decay, the induction motor feeds into the fault, temporarily keeping the voltage at the

terminals up but disappears after a few seconds if no power is restored. As the motor slows down, it consumes more reactive power with a larger current in an attempt to balance the electrical and mechanical torque leading to a further decrease in system voltage. On voltage recovery, the flux in the air gap builds up again, causing a large inrush current which acts against voltage recovery. The motor reaccelerates to its pre-fault operating point if the system is strong enough to withstand the high inrush current and subsequent voltage depression – in a system-wide manner. Otherwise the system voltage may collapse if the voltage depression passes a critical level and is unable to recover [37]. The relationship between the short-circuit power of the system and the voltage drop is shown in Fig. 4.12 for the microgrid in Fig. 4.1:

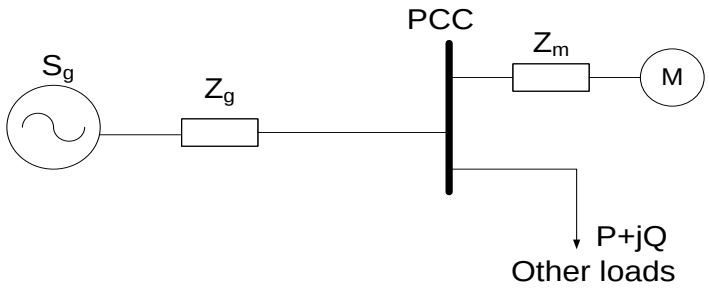

Fig. 4.12 One-line diagram of the voltage drop effect of a starting motor

where S_g is the short circuit power of the grid, Z_g is the grid impedance at the connected bus, and Z_m is the motor impedance.

The voltage drop at the PCC bus for other connected loads is:

$$V_{drop} = \frac{Z_m}{Z_g + Z_m} \tag{4.60}$$

Considering the motor apparent power S_m and a grid short-circuit power S_g, the grid impedance is:

$$Z_g = \frac{V^2}{S_g} \tag{4.61}$$

The motor impedance during starting is:

$$Z_m = \frac{V^2}{aS_m} \tag{4.62}$$

where a is the ratio of the starting current to the running current.

The voltage drop is:

$$V_{drop} = \frac{S_g}{S_g + aS_m} \tag{4.63}$$

If V_{drop} passes a critical point, the voltage instability may lead to a total voltage collapse.

The network characteristic and load curve for the microgrid shown in Fig. 4.1 before a disturbance event on the power system is shown in Fig. 4.13, where the loads are mainly exponential type loads such as induction motor loads. After a short voltage sag event, the increased current drawn by reaccelerating motors appears to the power system as an increase in load demand as shown in Fig. 4.14 with a shift in the load curve away from the network characteristic. If the voltage sag or momentary interruption is of sufficient duration to cause the motors to slow down significantly, more current is drawn upon restarting the motors which appears as an even greater increase in load

demand until the load demand no longer intersects the network characteristic as shown in Fig. 4.15. The microgrid experiences short-term voltage instability when the load curve passes the network bifurcation surface. A local PV generator is used to extend the network curve as shown in Fig. 4.16 so that the load curve now intersects the network characteristic and voltage stability is restored.

The maximum size of the local PV generator is determined by the difference between the initial P_0 and Q_0 and the P and Q values at the maximum loadability limit c_m.

$$\max\ P_{pv} = P_{c_m} - P_0 \tag{4.64}$$

and

$$\max\ Q_{pv} = Q_{c_m} - Q_0 \tag{4.65}$$

Any values of the local PV generator greater than max P_{pv} and Q_{pv} will likely lead to overvoltages at the PCC during light loading, resulting in the utility disconnection of the PV generator and the subsequent reduction in the voltage stability margin.

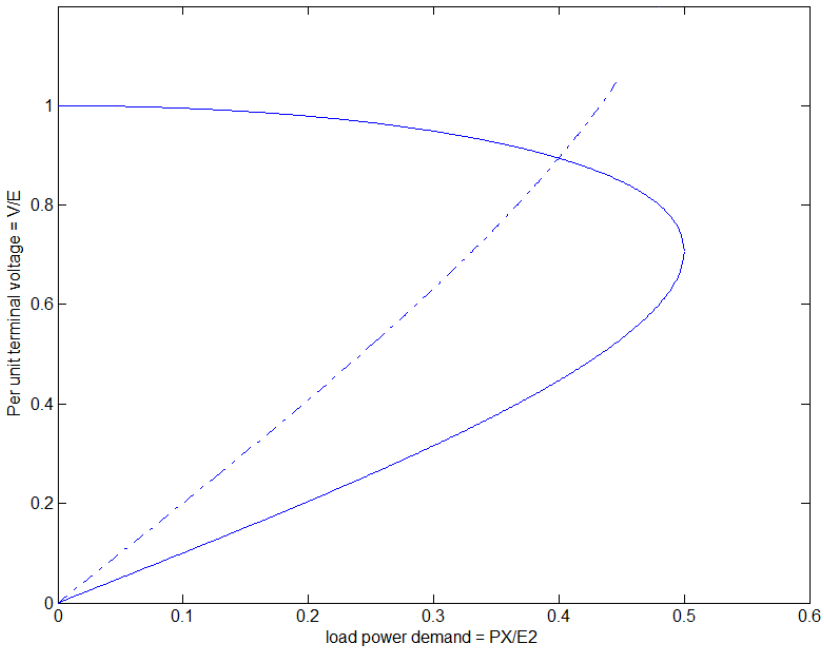

Fig. 4.13 Network and load curves before voltage sag event

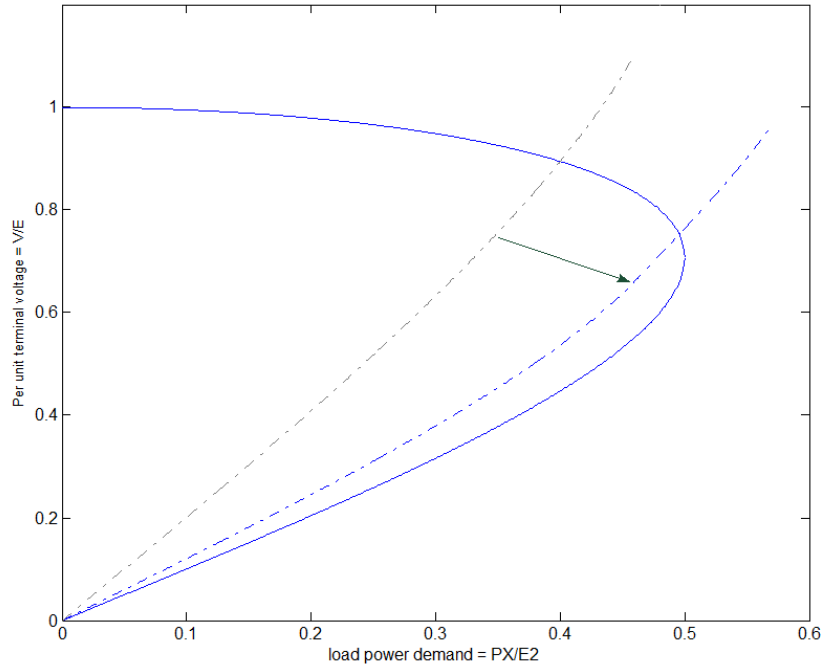

Fig. 4.14 Shift in load curve after voltage sag event

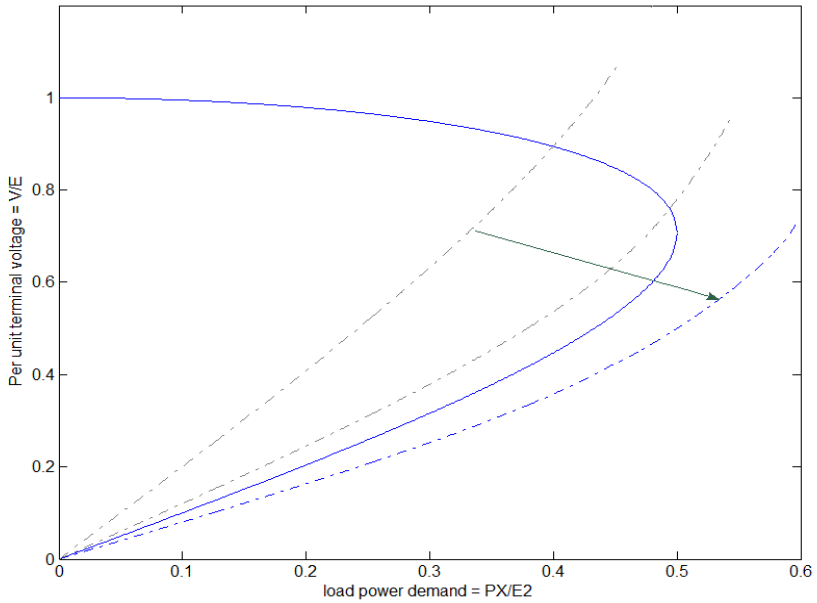

Fig. 4.15 Shift in load curve away from network characteristic

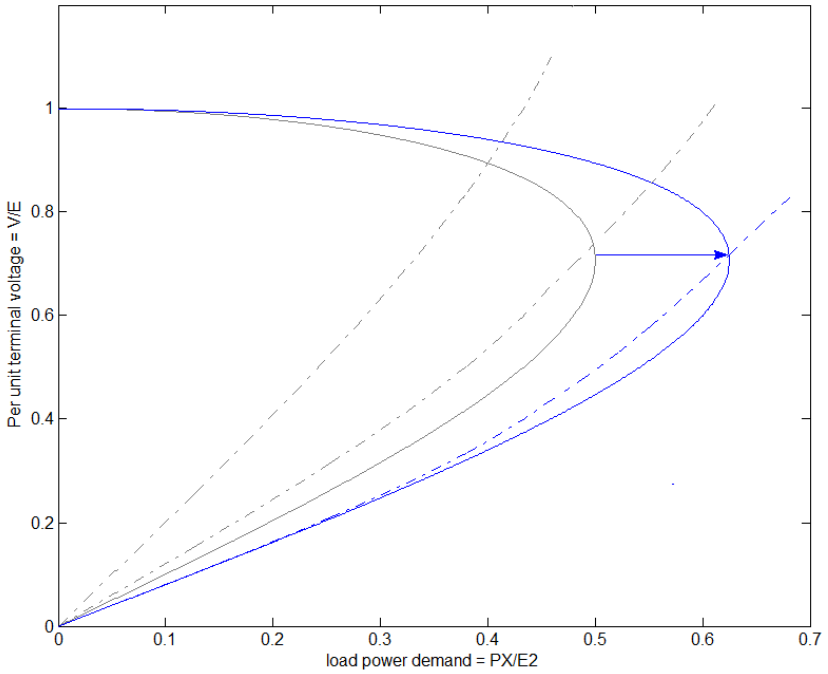

Fig. 4.16 Increase in network curve using local generator

4.3.2 Long-Term Voltage Instability

The approximate long-term dynamic model is given by:

$$\dot{c} = h(x, y, c, p) \tag{4.66}$$

$$0 = f(x, y, c, p) \tag{4.67}$$

$$0 = g(x, y, c, p) \tag{4.68}$$

The unreduced Jacobian for a fixed *p* is

$$J = \begin{bmatrix} h_c & h_x & h_y \\ f_c & f_x & f_y \\ g_c & g_x & g_y \end{bmatrix} \tag{4.69}$$

Assuming the Jacobian of the short-term dynamics, $\begin{bmatrix} f_x & f_y \\ g_x & g_y \end{bmatrix}$, is non-singular, the implicit function theorem can be applied to give the reduced long-term equations:

$$\dot{c} = H(c, p) \tag{4.70}$$

The equilibrium condition is thus,

$$H(c, p) = 0 \tag{4.71}$$

Eq. (4.71) is equivalent to $h(x, y, c, p) = 0$, since the Jacobian of the short-term dynamics has been assumed to be non-singular. As in the case of the short-term dynamics, the necessary condition for SNB of the long-term dynamics is the singularity

of the unreduced long-term Jacobian, which similarly coincides with the loadability limit of the long-term dynamics.

The long-term stability model is based on the assumption that the short-term dynamics are at equilibrium and only the effects of slow-acting devices are considered. The dynamics of certain power system components such as controllers and protective devices evolve in the long-term time scale, and the components are usually designed to operate after the short-term dynamics have died out, to minimize the interactions between time scales.

Long-term voltage instability can result when a sustained fault condition occurs on the power system causing it to operate with a reduced capacity over an extended period. The loss of one or more transmission lines between the source and the load will cause the power system to operate with a reduced capacity until the line is restored. Assuming the load demand remains the same during the outage period, the power system can experience voltage instability.

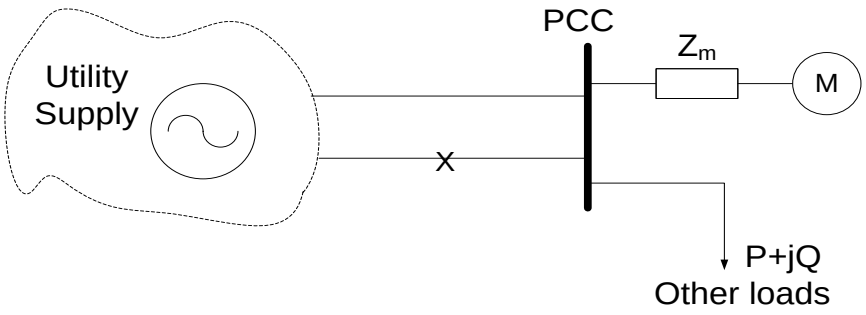

Fig. 4.17 Transmission line outage between source and load

If there is a sustained outage on one of the transmission lines between the source and the load in Fig. 4.17, the maximum power transfer capacity between the source and the load is effectively reduced. Voltage instability occurs when the load demand at the PCC bus exceeds the capacity of the remaining line to transfer sufficient real and reactive power from the source to the load.

The network characteristic and load curve for the power system before an outage of one of the transmission lines is shown in Fig. 4.18. When one of the transmission lines trips, the reduced maximum power transfer capacity is manifested as a shrink in the network characteristic wherein the maximum power transfer capacity is effectively halved. The post-disturbance network characteristic is shown in Fig. 4.19 where the load curve no longer intersects the network characteristic and the microgrid experiences long-term voltage instability. A local PV generator is applied in Fig. 4.20 to extend the network characteristic until it intersects the load curve again and voltage stability is restored.

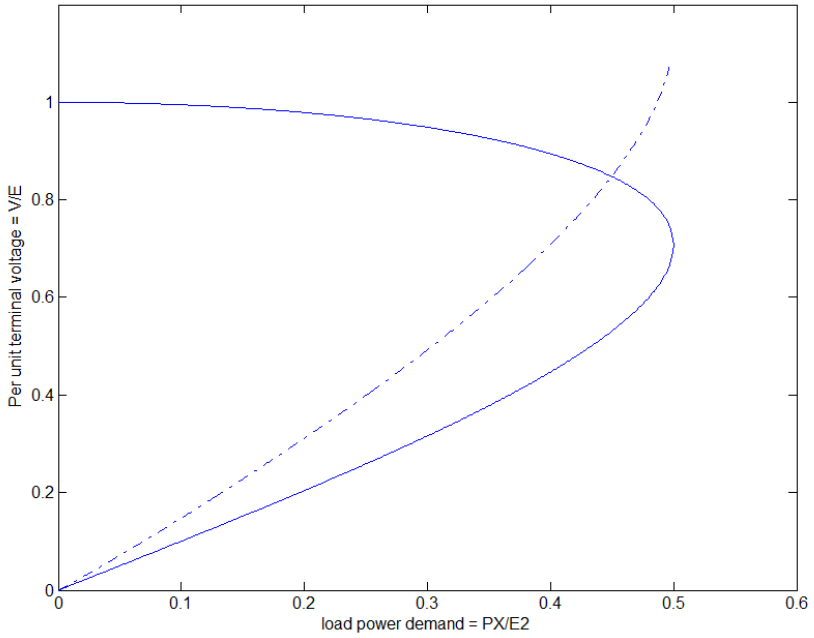

Fig. 4.18 Pre-disturbance network PV characteristic and load curve

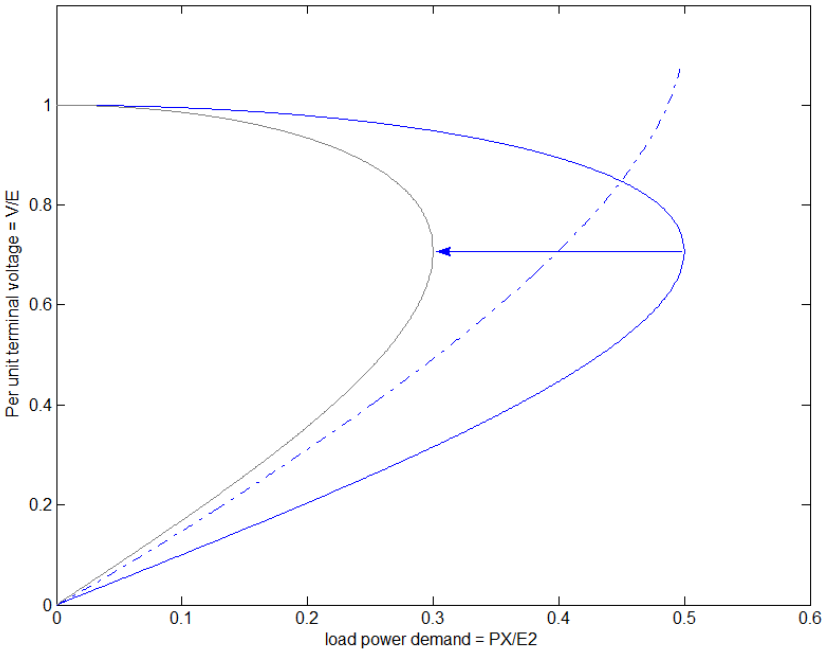

Fig. 4.19 Shift in post-disturbance network characteristic

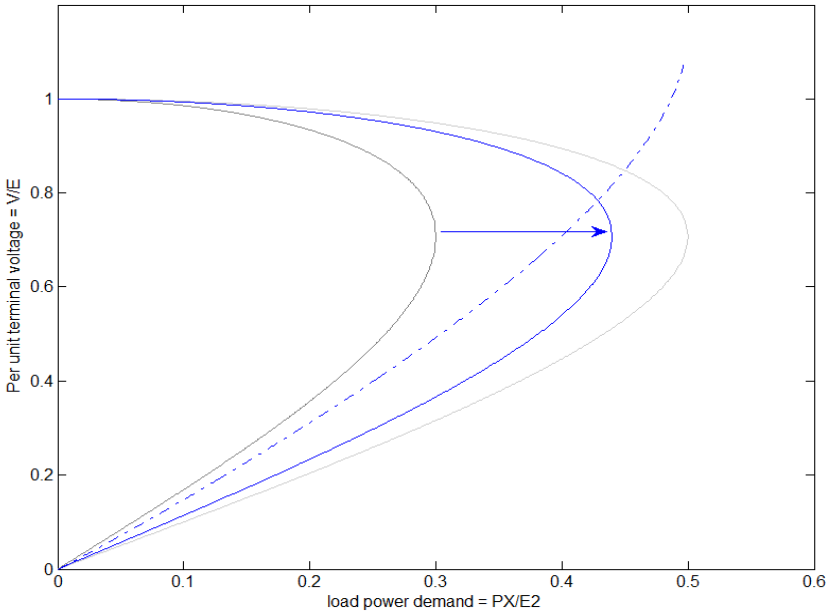

Fig. 4.20 Extension of network characteristic to intersect load curve

The post-disturbance network *PV* initially does not intersect the load characteristic and the system experiences voltage instability. The voltage instability can lead to a wider system collapse if remedial action is not quickly taken. As a result of this, power system designers and operators have to perform a voltage-power network analysis to determine the loadability limits with and without the microgrid prior to deploying the DG resources in the distribution system.

4.4 Restoration of the Load Equilibrium Point

In a practical system, not all the parameters (such as impedance and dynamic load power) that define the system operation are readily available and determining the Jacobian of such system becomes challenging. In such cases, a simpler yet effective

manner to determine the margins to voltage stability is to use the direction of the instantaneous real and reactive power consumption at the load buses. The direction and rate of change of operating point voltage to a small perturbation in either the real or reactive power can provide enough information as to the region where the power system is operating. Again, considering the study system of Fig. 4.10, the active and reactive power supply from the synchronous generator under normal operating conditions is determined from the power flow analysis using the initial settings of the OXL and AVRs. The active and reactive power contribution from the PV source and the load demand is similarly determined using widely available power flow analysis software.

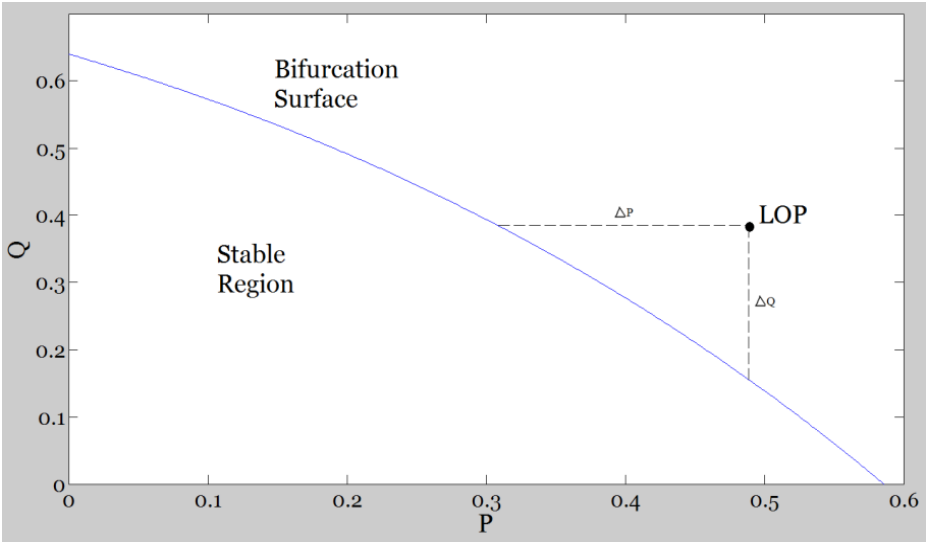

Fig. 4.21 LOP relative to bifurcation surface

The power space of the load operating point following a disturbance in the study system can be used to determine the required *P* or *Q* to maintain voltage stability as shown in

Fig 4.21. If the load operating point (LOP) falls outside the feasible region following the disturbance then corrective action is required to return the operating point to the feasible region on the left side of the bifurcation surface. The feasible operating point can be restored either by increasing the active power, ΔP, or increasing the reactive compensation, ΔQ, at the bus, although since increasing the active power will tend to raise the voltage at the PCC beyond acceptable limits, the latter option is preferable. The Euclidean distance, ΔQ, to the bifurcation surface is then calculated to determine the amount of reactive compensation required to restore the load equilibrium point.

5. VOLTAGE STABILITY ENHANCEMENT USING REACTIVE POWER CONTROL

This chapter investigates the dynamic voltage impact when converter-interfaced DGs are connected to the power system. Converter-interfaced DGs are typically operated at unity power factor and are disconnected from the rest of the power system upon a fault occurrence. The basic DG controller is used to study the voltage response at the PCC to fault occurrences in DG-embedded power systems. A novel real-time dynamic reactive power controller (DPRC) that controls the converter-interfaced DG to output real or reactive power depending on the short-term and long-tem voltage stability margins is proposed. The maximum and minimum real and reactive power support permissible from the DG is determined from the bifurcation analysis and is used as the limiting factors in controlling the real and reactive power contribution from the PV source. The first stage of the controller regulates the voltage output based on instantaneous power theory to prevent overvoltage at the point-of-common coupling (PCC) while the second stage regulates the reactive power supply by means of power factor and reactive current droop control. The DRPC is implemented in PSCAD and the voltage response is compared to the operation of the basic controller. The advantage of dynamic control is demonstrated as the controller is able to respond to voltage variations in real-time and maintain the output of the grid-tied DG within acceptable limits.

5.1 Microgrid Controller Modeling

This section focuses on operation of the DRPC to maintain the power system voltage stability. The DRPC is implemented in the industrial microgrid shown in Fig. 5.1. The industrial microgrid consists of:

- The PV source is connected to the PCC via the DRPC and an inverter. The PV source has an MPPT and is initially set to generate real power only.
- The total load is represented with one aggregate load with real and reactive power demand. They are modeled as constant impedance and constant power loads.
- The reactive power is initially supplied by the grid via the PCC. The DRPC is later used to control the PV source to supply both real and reactive power to balance the reactive power shortfall from the grid.
- The power imbalance scenarios are simulated first by changing the active and reactive power demand of the load to indicate a gradual increase in load, then by applying a three-phase fault on the grid side to indicate a short duration system disturbance.

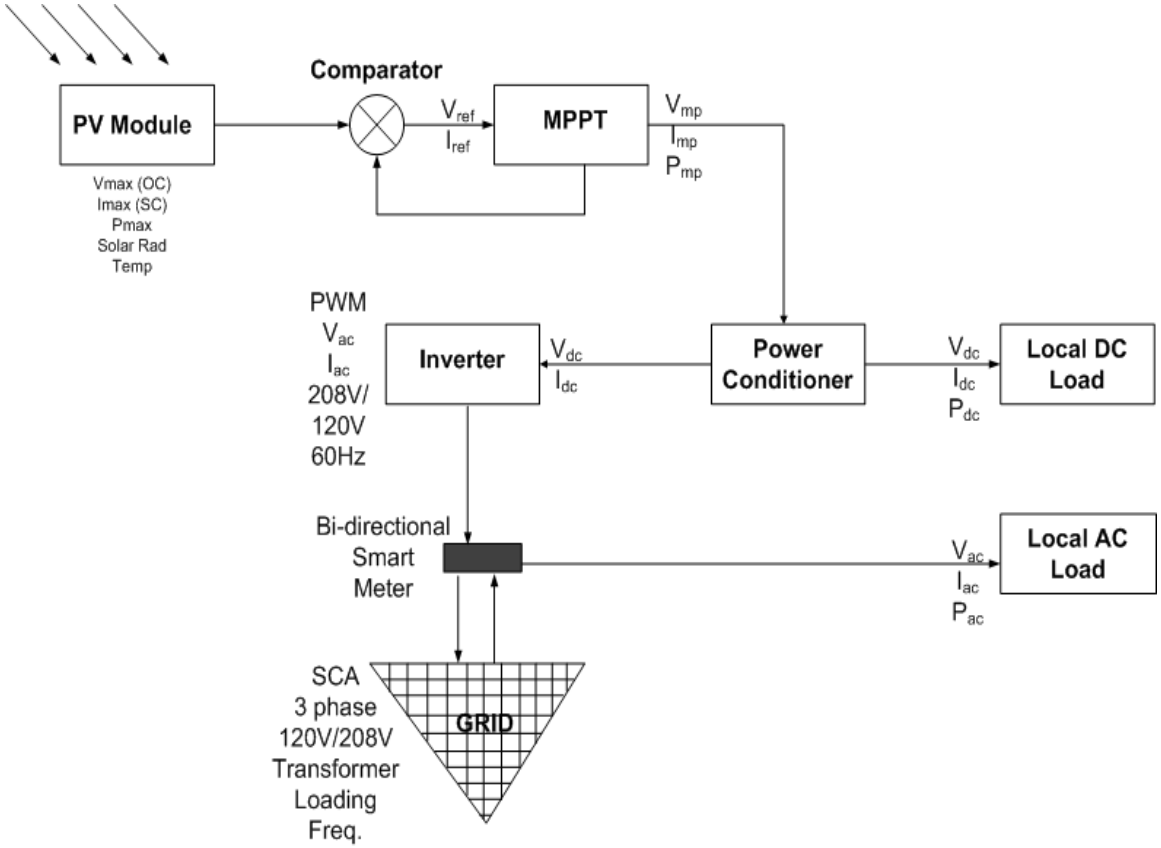

Fig. 5.1 Block diagram showing layout of PV microgrid

The grid supply serves as the voltage and current reference for the industrial microgrid and supplies both real and reactive power. The grid is modeled as a constant voltage source shown in Fig. 5.2, where E_s is the constant voltage with a fixed frequency, and Z_s is the source impedance. The PV is modeled as a controlled current source operated by the MPPT to supply the maximum possible real power. It is disconnected from the system if the voltage at the PCC exceeds 110% of the nominal voltage. The representation of the PV source is shown in Fig. 5.3, where the V_{pv} and I_{pv} are the terminal voltage and output current of the PV after the MPPT.

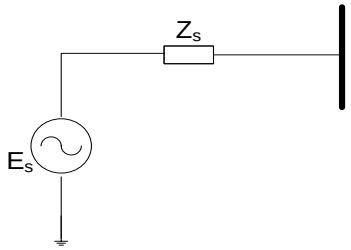

Fig. 5.2 Constant voltage source model

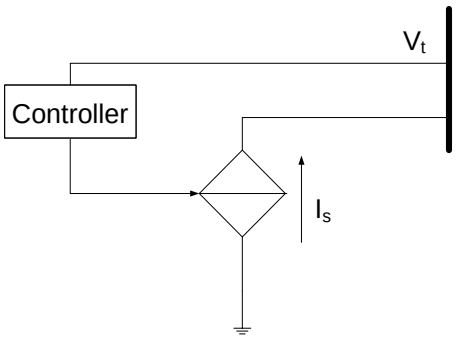

Fig. 5.3 Controlled current source model

5.2 Dynamic Voltage Control of Grid-Tied DG

A photovoltaic (PV) system is well suited to support the voltage stability of the grid by utilizing the reactive power capacity of the PV, instead of the current practice of operating most DGs at unity power factor. The commonly used basic controller is first examined then a two-stage reactive power control method that enables the PV to produce active and/or reactive power when needed is presented. The first stage employs a closed loop voltage control method to ensure that the voltage at the point-of-common coupling (PCC) is maintained within a specified range, while the second

stage controls the active and reactive power output of the PV inverter by adjusting the transformed real and reactive currents of the instantaneous power at the PCC based on the power factor measurement of the instantaneous voltage and reference current. The reactive power control method is implemented in PSCAD and the voltage stability enhancement of the PV system is demonstrated.

5.2.1 Voltage Control using Basic Controller

The role of the central generators is to maintain the power balance in the entire system and supply any deficient real and reactive power demand of the microgrid. The grid supply represented by the constant voltage source (Fig. 5.2) must supply the required active and reactive power requirements of the microgrid within the maximum power transfer limits of the power system, which is inversely proportional to the source impedance Z_s (Section 4.1). The PV source represented by the controlled current source (Fig. 5.3) supplies active power to the microgrid within the acceptable voltage limits at the PCC. The basic functionality of the controller is shown in Fig. 5.4.

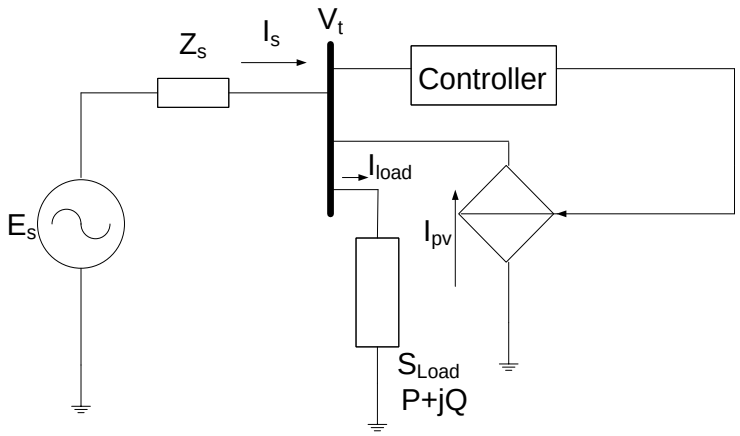

Fig. 5.4 Implementation of the basic controller at the PCC

The basic controller implemented in Fig. 5.4 contains the two generating sources – constant voltage source with reference voltage E_s and a controlled current source supplying a varying current I_{pv} - and a complex load consuming real and reactive powers P_{load} and Q_{load} respectively. Under normal operation, the voltage at the PCC is the combination of the grid voltage E_s and the PV output voltage V_{pv}.

When the microgrid experiences a disturbance, the power balance should be restored by controllers at the central grid generators by increasing the real or reactive power supply to the microgrid. This reactive power control is done automatically by the central generators that provide the voltage and frequency reference for the power system (Section 3.1). For example, if the reactive power load consumption Q_{load} increases, the grid supply E_s is increased accordingly. The controlled current source representing the PV continues to supply the maximum real power possible P_{vp}, provided the voltage at the PCC is still within the preset limits. If on the other hand, the increase in the grid

voltage E_s causes the voltage at the PCC to exceed the preset limit, then the PV is disconnected so that the necessary reactive power can be supplied without exceeding the voltage limit. The PV is reconnected after the reactive power flow in the system returns to the pre-disturbance state or reaches a new equilibrium state where the combination of the grid voltage and PV output voltage at the PCC is within acceptable limits.

The basic controller is implemented in PSCAD and is shown in Fig. 5.5. The controller is used in a PV microgrid system connected to the utility mains. The system consists of a PV source connected via an MPPT and inverter to the local bus, to which the mains supply and local induction motor loads are also connected. The induction motor loads are represented by the quadratic torque model. The grid voltage is initially set to 1 p.u., the PV is able to supply a maximum of 200 KW and the cumulative induction motor load is 350 HP, representing the normal steady-state operating condition of the microgrid. The system experiences a three-phase to ground fault on the primary side of the grid supply but close to the microgrid power system, the fault occurring after 1.5s and lasting for 0.75s. During the fault occurrence (representing the stressed conditions of the microgrid), the PV system is disconnected from the local bus, as is typically the case. The simulations are performed with a time step of 50μs and a run time of 3.0s.

The rotor speed, mechanical torque and electrical torque of the cumulative induction motor load are shown in Figs. 5.6 – 5.8. At the onset of the fault, the PV system is disconnected from the local bus and the voltage at the PCC sags as a result of the

ground fault. This leads to an immediate decrease in the motor speed, and the consequent jump in the reactive power demand – due to the action of the motor self-restoring devices. The increased reactive power demand leads to a further decrease in system voltage as described in Chapter 4. At 2.25s, when the fault is cleared, there is a steep increase in the mechanical torque of the motor, and the higher reactive power demand even after the fault is cleared can lead to severe voltage instability under peak demand conditions as a result of the mismatch between the reactive power demand and available supply. The overall startup time for the induction motor loads is increased as a result of the voltage sag.

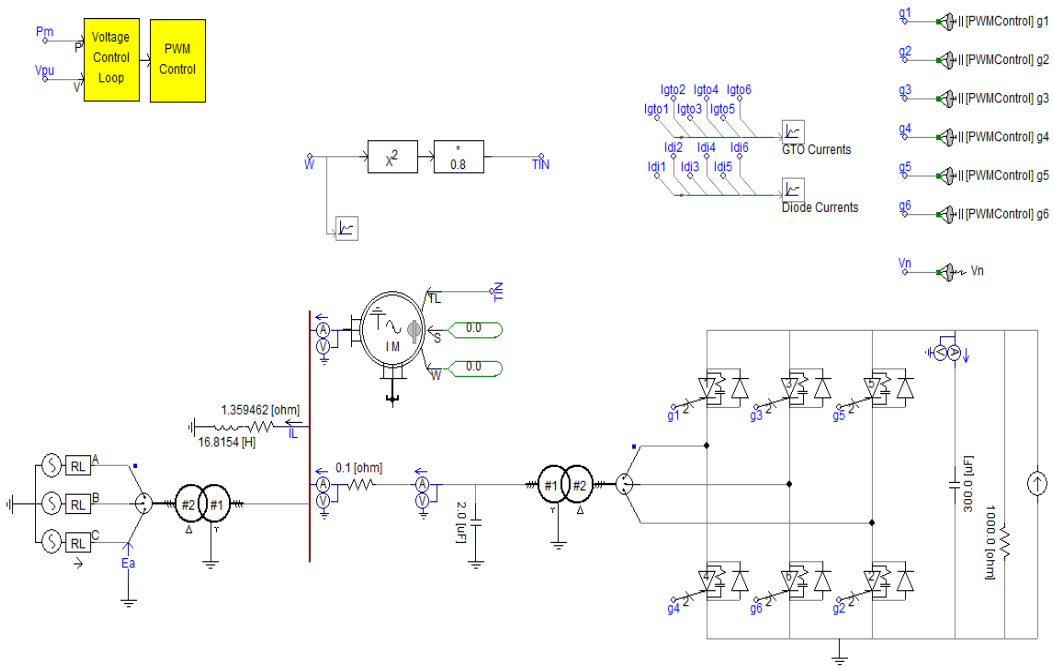

Fig. 5.5 PSCAD implementation of basic controller

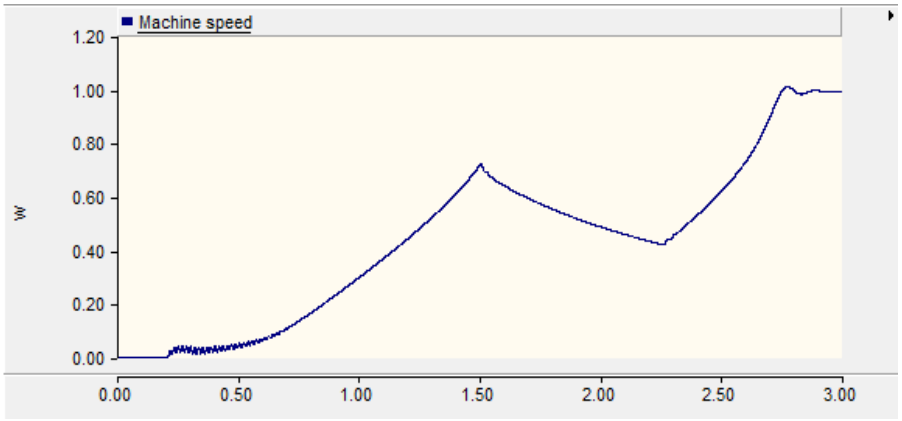

Fig. 5.6 Rotor speed of induction motor with basic controller

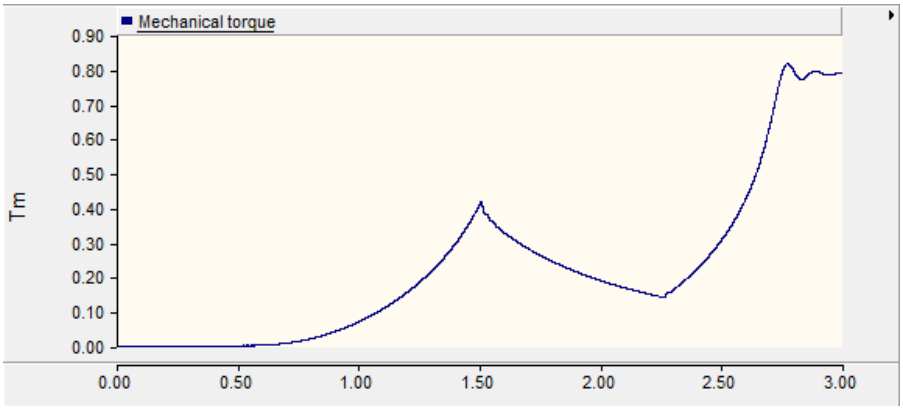

Fig. 5.7 Mechanical torque of induction motor with basic controller

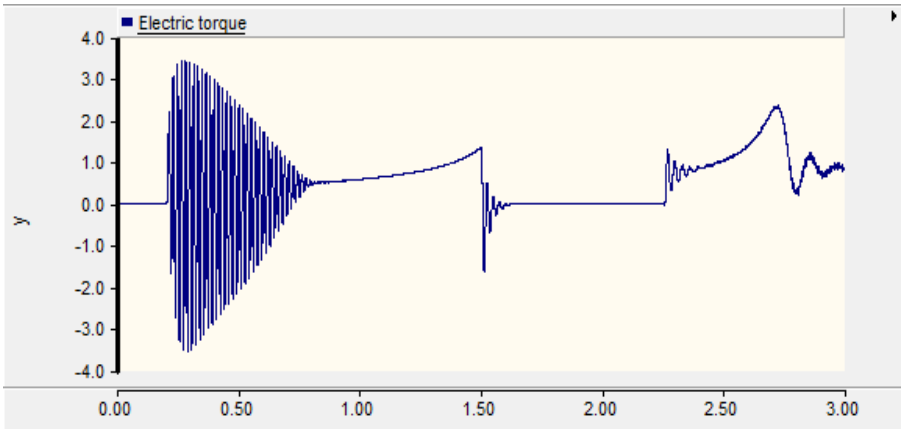

Fig. 5.8 Electrical torque of induction motor with basic controller

5.2.2 Real-Time Dynamic Reactive Power Controller

A novel dynamic reactive power controller (DPRC) that operates the PV source in a manner that ensures the PV remains online through system disturbances is proposed in place of the basic controller that disconnects the PV source during a fault occurrence or when the voltage rises at the PCC rises above acceptable levels. The DRPC operates the PV inverter using a two-stage voltage vs. reactive current droop control method. The first stage implements the voltage control by means of a closed-loop control method where the measured grid voltage (V_g) at the PCC is compared with a preset upper and lower limit range set by the operator, and if V_g is found out of range and with a lagging power factor, the reactive power output of the inverter is increased. Alternatively, if V_g is out of range but with a leading power factor, the real power output of the inverter is lowered. The reference real and reactive currents are determined as follows:

The instantaneous voltage and current at the inverter-grid interface is measured as [89]

$$V_a(t) = \sqrt{2}V \sin \omega t \tag{5.1}$$

$$i_a(t) = \sqrt{2}I \sin(\omega t - \theta) \tag{5.2}$$

and the instantaneous power,

$$P_a(t) = V_a(t)I_a(t) \tag{5.3}$$

$$P_a(t) = V_a I_a \cos\theta\,(1 - \cos 2\omega t) - V_a I_a \sin\theta \sin 2\omega t \tag{5.4}$$

$$P_a(t) = P_a(1 - \cos 2\omega t) - Q_a \sin 2\omega t \tag{5.5}$$

The current in terms of $\sin \omega t$ and $\cos \omega t$ is

$$i_a(t) = \sqrt{2} I_a \sin(\omega t - \sin \theta \cos \omega t) \tag{5.6}$$

From eq. (5.6), the real and reactive components of the current using coordinate transform are respectively

$$i_d = \left(\sqrt{2} I_a \cos \varphi\right) \sin \omega t \tag{5.7}$$

$$i_q = \left(\sqrt{2} I_a \sin \varphi\right) \cos \omega t \tag{5.8}$$

where i_d is in phase with $V_a(t)$ and i_q is perpendicular to $V_a(t)$ and $I = i_d + i_q$. If the coordinate transform is applied to the voltage:

$$\begin{bmatrix} V_d \\ V_q \\ V_0 \end{bmatrix} = \frac{2}{3} \cdot \begin{bmatrix} 1 & -1/2 & -1/2 \\ 0 & \sqrt{3}/2 & -\sqrt{3}/2 \\ 1/\sqrt{2} & 1/\sqrt{2} & 1/\sqrt{2} \end{bmatrix} \cdot \begin{bmatrix} V_a \\ V_b \\ V_c \end{bmatrix} \tag{5.9}$$

The instantaneous power is expressed as

$$P_a(t) = v_a\left(i_d + i_q\right) = v_a i_d + v_a i_q = p(t) + q(t) \tag{5.10}$$

The three-phase instantaneous power is obtained as

$$P_{3\varphi} = v_a i_a + v_b i_b + v_c i_c = v_d i_d + v_q i_q + v_0 i_0$$

$$P_{3\varphi} = P_d + P_q + P_0 = P + P_0$$

where P_o is the instantaneous zero-sequence power.

$$p = v_d i_d + v_q i_q = 3VI\cos\theta = P_{3\varphi} \tag{5.11}$$

$$q = v_{d'} i_{d'} + v_{q'} i_{q'} = 3VI\sin\theta = Q_{3\varphi} \tag{5.12}$$

The instantaneous real and reactive power represented in matrix form is

$$\begin{bmatrix} P \\ Q \end{bmatrix} = \begin{bmatrix} V_d & V_q \\ -V_q & V_d \end{bmatrix} \cdot \begin{bmatrix} i_d \\ i_q \end{bmatrix} \tag{5.13}$$

and the reference current

$$\begin{bmatrix} i_d \\ i_q \end{bmatrix} = \frac{1}{V_d^2 + V_q^2} \begin{bmatrix} V_d & -V_q \\ V_q & V_d \end{bmatrix} \begin{bmatrix} p \\ q \end{bmatrix} \tag{5.14}$$

The control algorithm for the DRPC using the derived real and reactive reference current is shown in Fig. 5.9. The limits for the real and reactive power output are set based on the *max* and *min ΔP* and *ΔQ* calculated from the bifurcation stability analysis in Chapter 4. If the voltage at the PCC is capacitive and the load operating point is close to the stability margin, then option 1 of reducing the PV DC voltage via direct MPPT control is preferred.

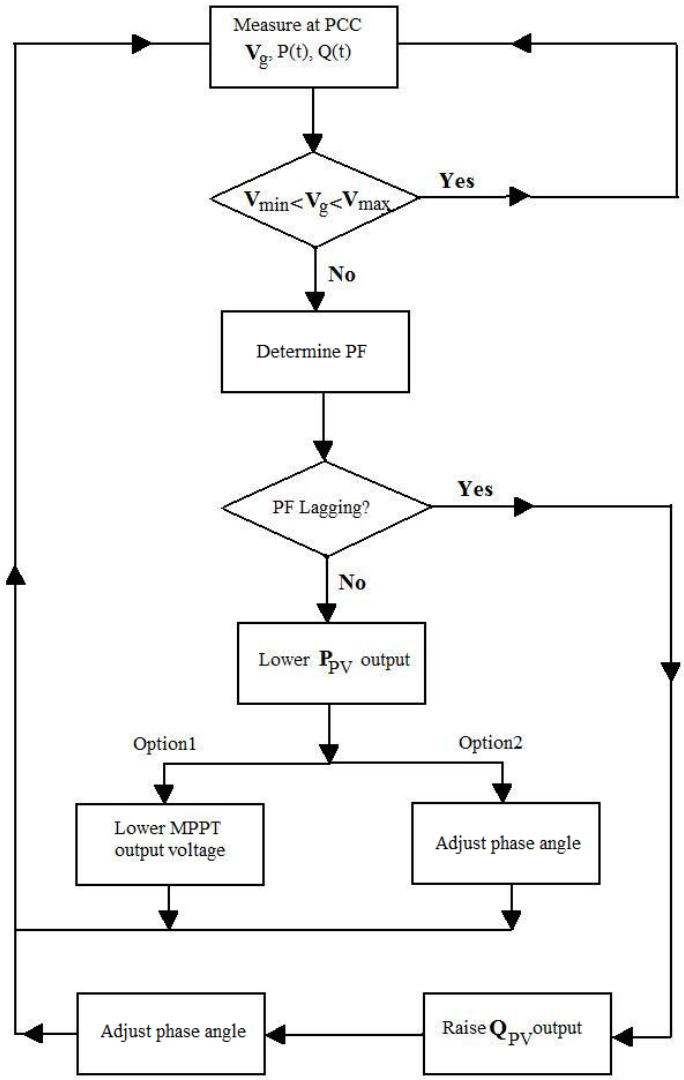

Fig. 5.9 Control algorithm for real-time DRPC

The real and reactive components (i_d *and* i_q) of the current and voltage are derived from the measured instantaneous power at the PCC using instantaneous power theory and coordinate transform.

The output voltage of the PV inverter is controlled by adjusting the transformed real and reactive currents based on the power factor measurement of the instantaneous voltage

and reference current. In the case of undervoltage at the PCC, the transformed reactive current, i_q, is increased while the transformed real current, i_d, is kept the same to output more inductive reactive power from the PV. In the case of overvoltage, i_d is decreased while i_q is kept the same to reduce the output voltage from the PV. The adjusted i_d and/or i_q are transformed back to the *abc* reference frame and used for the inverter PWM control.

The inverter output voltage is synchronized to the grid voltage and frequency using a PI controller. The measured i_d and i_q currents are compared to the set reference i_d and i_q currents, and the current control error is fed into the PI controller and comparator, where the PWM modulation gain k_p is generated. The utility frequency, $\omega_u = 2\pi f_u$, sensed by a phase-lock loop (PLL) circuit, is combined with the PWM modulation gain and angle to generate the inverter output voltage, $k_p V_{inv}\sin(\omega_u t + \alpha)$. The desired magnitude of the inverter voltage is realized by adjusting the set reference i_d and i_q currents based on the droop, ϑ, of the voltage vs. reactive power at the PCC shown as in Fig. 5.10. The overall control scheme and PI controller are shown in Figs. 5.11 and 5.12.

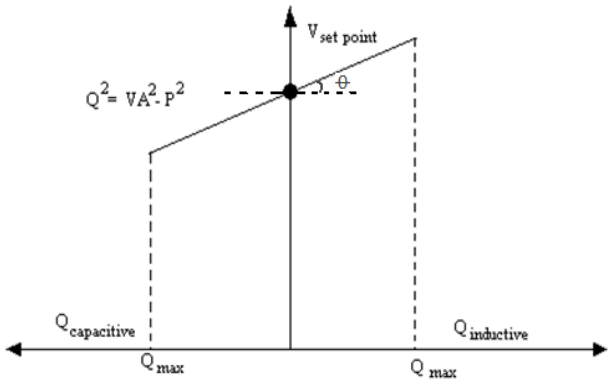

Fig. 5.10 Voltage set point vs. reactive power droop

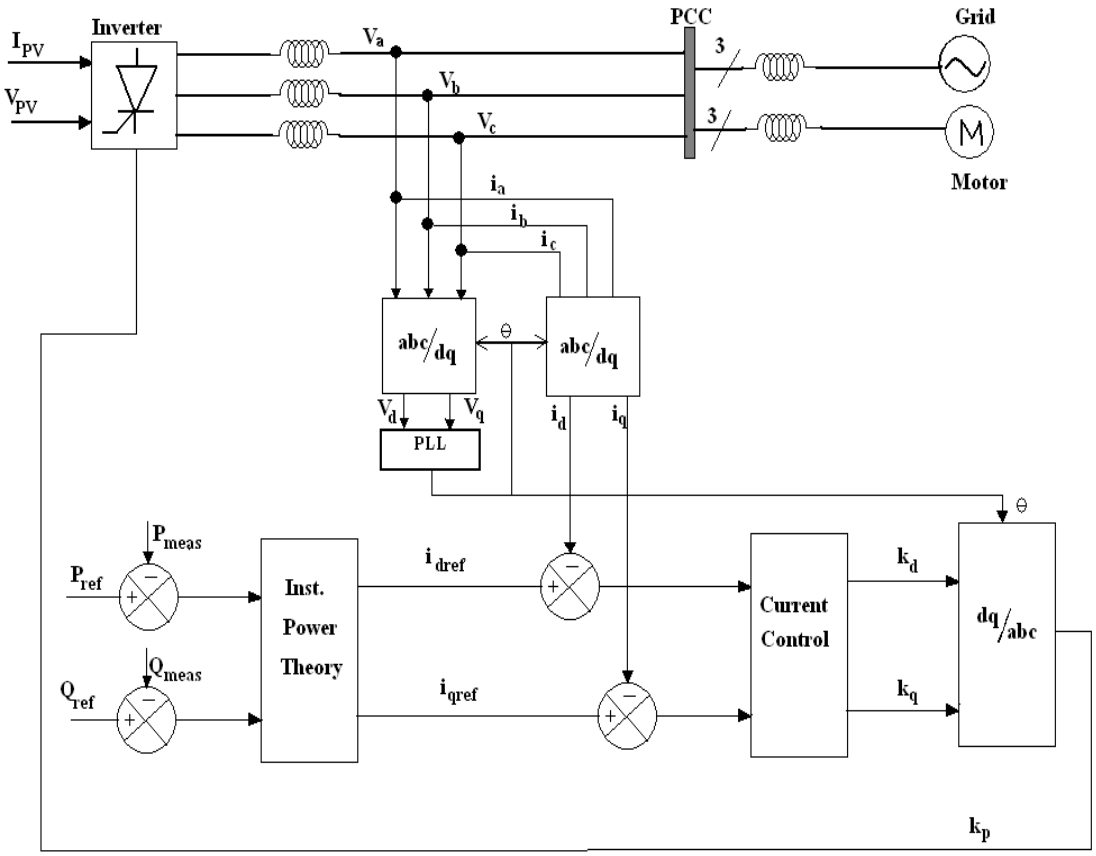

Fig. 5.11 Overall inverter control scheme

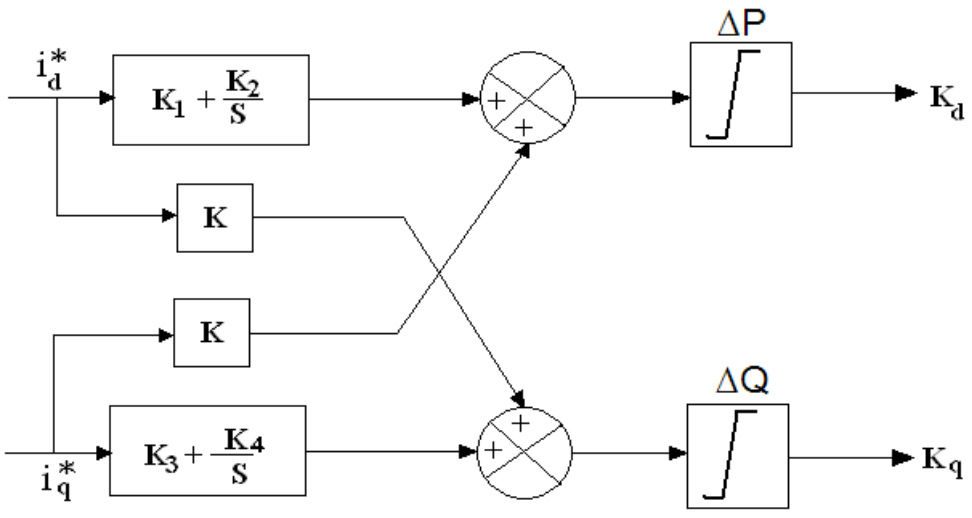

Fig. 5.12 Current controller

5.3 Simulations and Results

The DRPC is implemented in PSCAD and is shown in Fig. 5.13. The independent real and reactive power tracking capability of the DRPC is tested in a two-bus system, containing a PV source connected to an infinite reactive load bus. The measured *P* and Q responses are shown in Figs. 5.14 and 5.15, where the reactive power set point is adjusted in response to a system disturbance at 1.5s, while the active power set point remains nearly constant. The terminal voltage at the inverter output is shown in Fig. 5.16. The dynamic responses show the quick tracking capability of the DRPC.

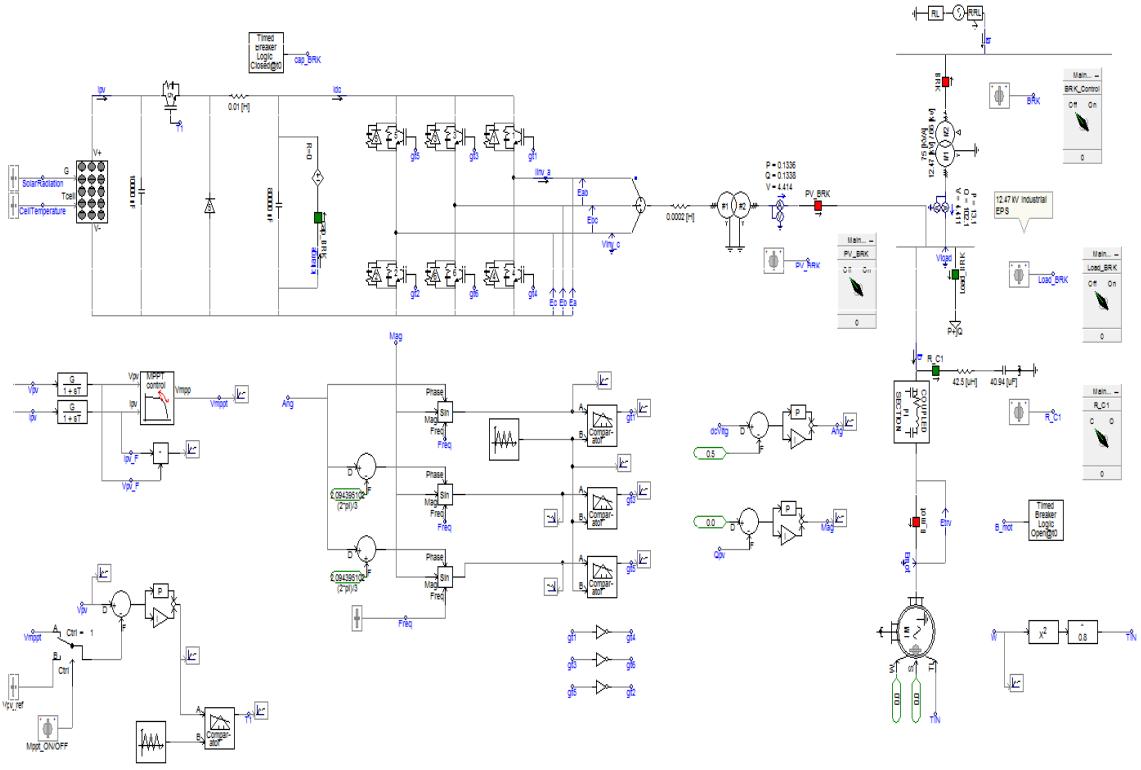

Fig. 5.13 PSCAD implementation of PV microgrid utilizing DRPC

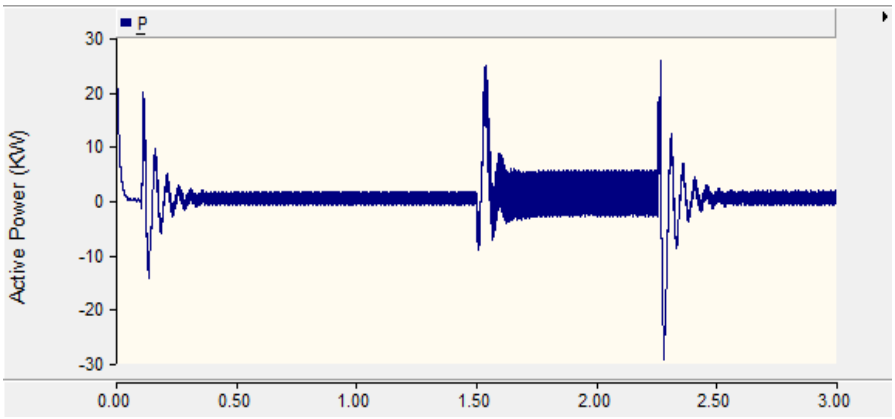

Fig. 5.14 Real power response of DRPC

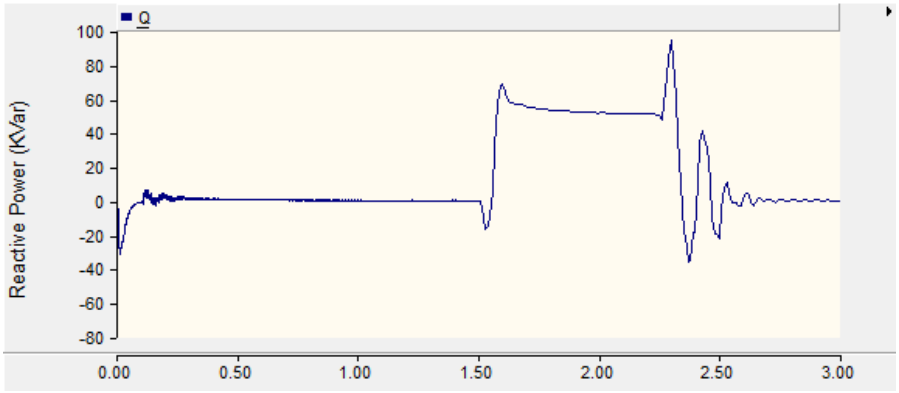

Fig. 5.15 Reactive power response of DRPC

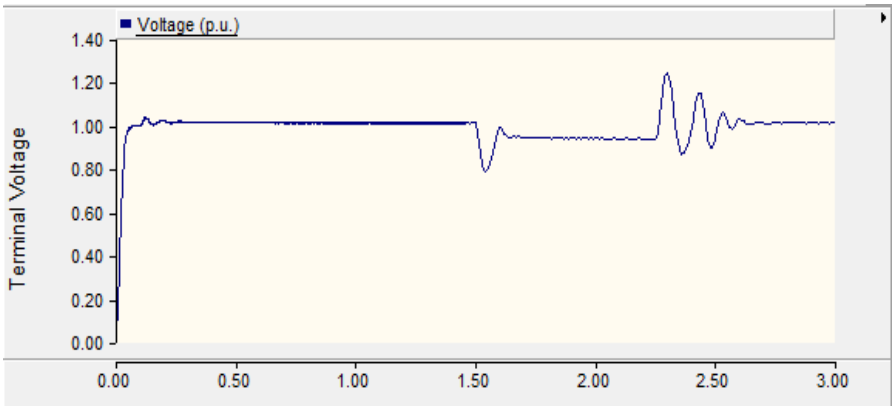

Fig. 5.16 Inverter output terminal voltage

The DRPC is implemented in the same system as was done for the basic controller. The grid voltage is initially set to 1 p.u., while the PV is now able to supply up to +100 KVar and a maximum of 150 KW. The cumulative induction motor load remains the same at 350 HP, representing the normal steady-state operating condition of the microgrid. The system experiences a disturbance at 1.5s in the form of a three-phase to ground fault that causes momentary voltage sag lasting for 0.75s. During the fault occurrence (representing the stressed conditions of the microgrid), the PV system remains connected to the local load bus via the DRPC. The simulations are performed with a time step of 50μs and a run time of 3.0s.

The rotor speed, mechanical torque and electrical torque of the cumulative induction motor load are shown in Figs. 5.17 – 5.19. At the onset of the fault, the DRPC is able to supply the increased reactive power demand of the motor before the rotor speed decrease significantly as shown in Fig. 5.17. The mechanical and electrical torques of the motor are maintained during the fault as shown in Figs. 5.18 and 5.19 respectively, allowing the motor to fully start. The system voltage is therefore less stressed during and immediately after the fault is cleared. This approach eliminates the need for load shedding or staggered motor start during peak demand conditions on the grid.

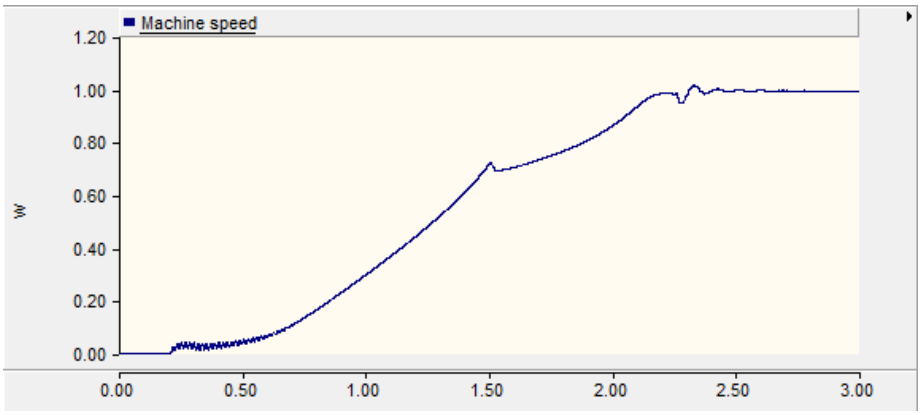

Fig. 5.17 Rotor speed of induction motor with DRPC

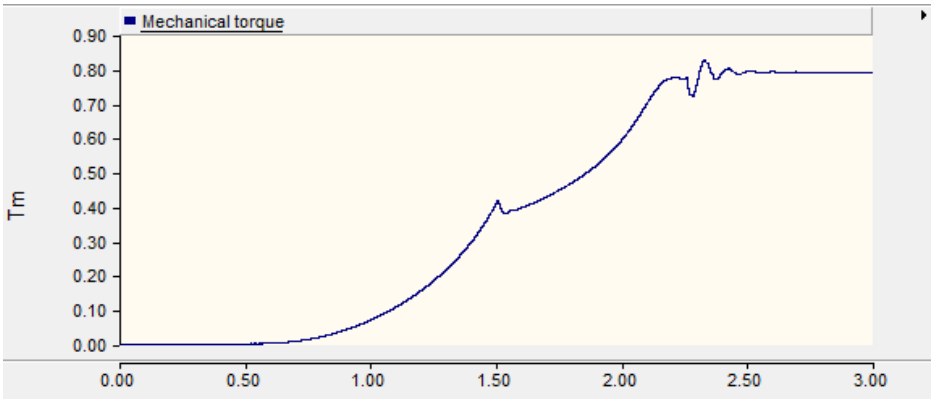

Fig. 5.18 Mechanical torque of induction motor with DRPC

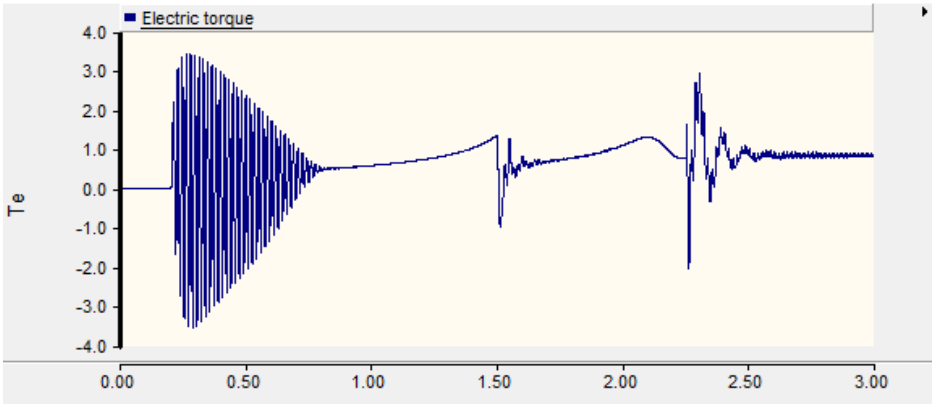

Fig. 5.19 Electrical torque of induction motor with DRPC

6. CASE STUDY FOR TAMPA LOWRY PARK ZOO MICROGRID

The effect of dynamic reactive power compensation is first investigated in an IEEE 13-bus test feeder system and then for an industrial microgrid using data from an actual PV installation in Tampa, FL. The PV microgrid is operated primarily as a peak load shaving DG source but can be modified to incorporate the DRPC to support the local area voltage stability. The system is simulated in EDSA to determine the power flow and thus the steady-state voltage stability of the industrial microgrid and nearby buses with and without the DRPC in operation. The scenarios investigated include the case where there is no DG present in the power system, the case where DG is present but is used to supply real power only to the load bus, and finally, the case where DG is present and is used to supply both real and reactive power to the load bus. The chapter concludes by analyzing the impact of the application of the DRPC control method on the steady-state (long-term) load voltage stability in the presence of voltage sags and momentary interruptions.

6.1 Description of the Study Systems

The widely-used IEEE 13-bus test feeder system is implemented in EDSA to determine the power flows when active loads consisting of mainly induction motors are added to the power system. The IEEE 13-bus test system is used in order to allow for easy comparisons of the test results with other voltage control mechanisms and various load configurations. A section of the Tampa Electric (TECO) distribution network is then approximated to a 13-bus power system and is used to illustrate the voltage stability enhancement application of DGs operated to independently regulate the real and reactive power outputs using data from a real-life system. The power flow analyses in this chapter are performed as the steady-state complement to the dynamic analysis performed in Chapter 5.

6.2 IEEE 13-Bus Test Feeder System

The IEEE 13-bus test feeder system is a commonly used test system in power system planning and analysis. The benefit of using this test system is to validate the power flow simulations using tests results that are widely available in literature making the research useful for comparison purposes. Although the 13-bus system is relatively small, the voltage impact on a reasonably-sized distribution area can still be adequately captured. The one-line diagram of the IEEE 13-bus system containing three DG sources is shown in Fig. 6.1 and the load demand at each bus is presented in Table 6.1.

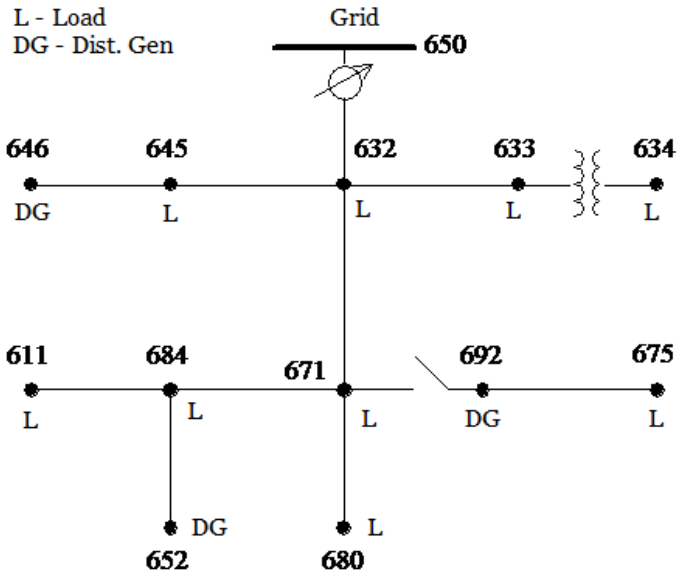

Fig. 6.1 One-line diagram of IEEE 13-bus test feeder system

TABLE 6.1 Modified IEEE 13-bus test feeder characteristics

Bus	KW	KVAR
634	400	290
645	170	125
646	230	132
652	128	86
671	1155	660
675	843	462
611	170	80
632	200	116
633	100	60
680	200	120

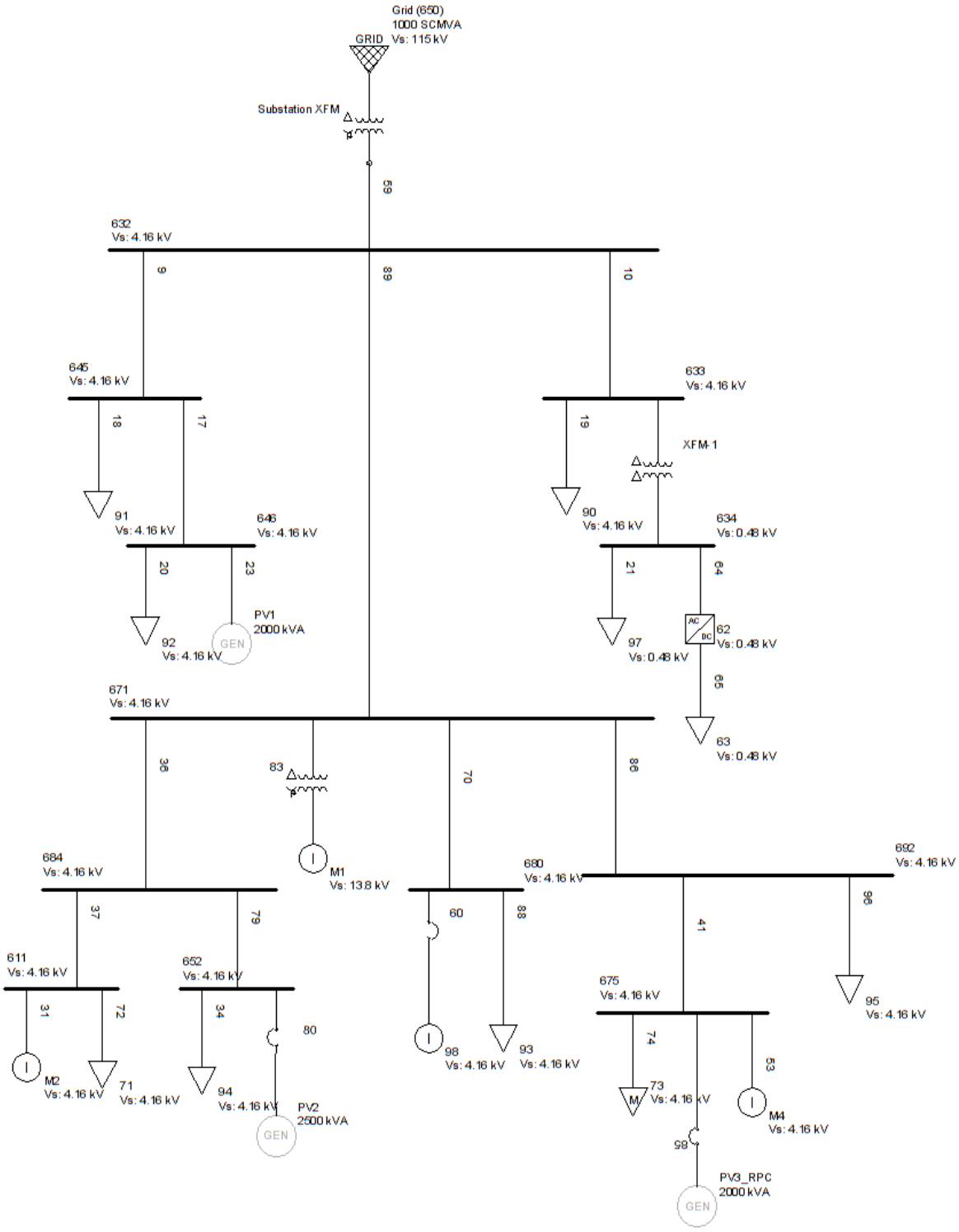

Fig. 6.2 IEEE 13-bus test feeder system with no active DG sources

The basic parameters are taken from [90] with slight modifications made at some buses. The scenario of most interest is the case of peak load demand when there is little reserve capacity left on the system. As such, there are no swing buses and every generator is set with a reactive power limit. The generators are modeled in EDSA library using the Park (dq) transformation parameters of the synchronous generator.

6.2.1 Voltage Impact without DG Sources

The IEEE 13-bus test feeder system implemented in EDSA is shown in Fig. 6.2. Initially, the 13-bus system contains no DG sources (DG sources initially switched off in EDSA) with only the main grid supplying the power, and all the other buses represented as load buses. The motor loads at buses 611, 671, 675, and 680 indicate large industrial induction motors (M1 – M4) and all other loads indicate fixed loads. All the induction motors are assumed to be initially off while all the fixed loads are on. The induction motor loads are all started at the same time indicating a post-fault scenario where all the induction motors have previously come to a stop or slowed down significantly. The pre-start, during starting, and post-start voltages for some buses are presented in Table 6.2 and Fig. 6.3. It is seen that the voltages at all the buses shown have unacceptably low voltages during the starting process, mainly as a result of insufficient reactive power supply from the grid.

TABLE 6.2 Bus voltages with no active DG sources

Bus	Pre-Start Voltage (p.u.)	During-Start Voltage (p.u.)	Post-Start Voltage (p.u.)
671 (M1)	0.8665	0.3672	0.7683
611 (M2)	0.8664	0.3670	0.7681
680 (M3)	0.8663	0.3659	0.7675
675 (M4)	0.8593	0.3497	0.7601
652	0.8666	0.3675	0.7694

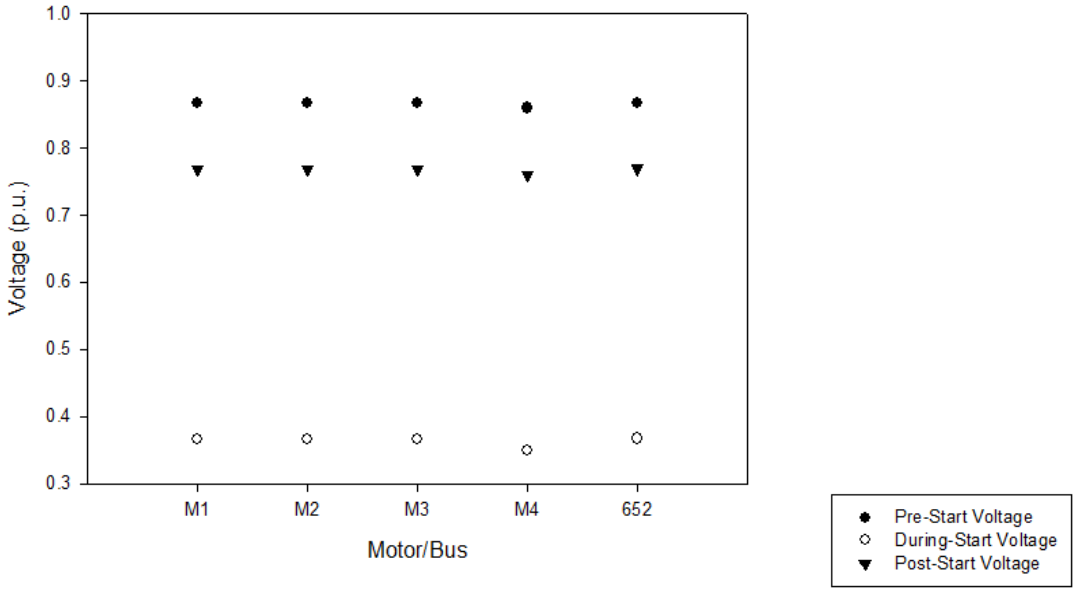

Fig. 6.3 Bus voltages with no DG present

6.2.2 Voltage Impact with DG Present

The simulations are repeated with DG sources added at buses 646 and 675. The DG sources output active power only indicating DG operation at unity power factor. The

pre-start, during, and post-start voltages at the motor load buses are shown in Table 6.3. Here, the voltage profile at buses 671, and 680 showed some slight improvement, while buses 611 and 652 remain unaffected by the DG sources. The voltage profile at buses 646 and 675 show significant improvement and the voltage levels during motor starting falls within acceptable limits.

TABLE 6.3 Bus voltages with partial DG sources

Bus	Pre-Start Voltage (p.u.)	During-Start Voltage (p.u.)	Post-Start Voltage (p.u.)
611	0.8668	0.3689	0.7695
671	0.8865	0.3692	0.7912
675	0.9042	0.5974	0.8481
680	0.8795	0.3690	0.7902
646	0.9086	0.6153	0.8603
652	0.8665	0.3671	0.7692

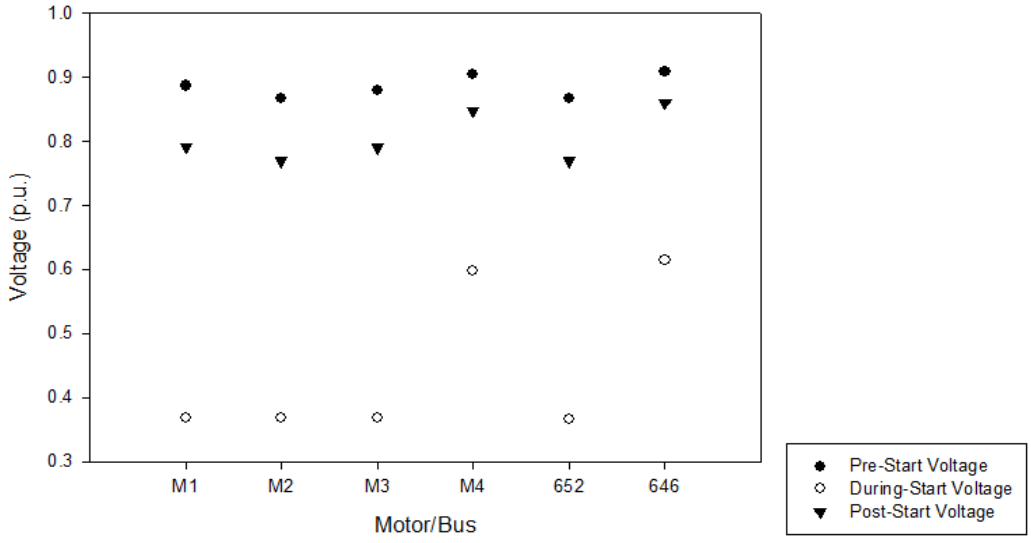

Fig. 6.4 Bus voltages with two DGs on

A third larger DG operating at unity power factor is added at bus 652 and the voltage profiles at nearby buses are shown in Table 6.4 and Fig. 6.5. With the third DG in operation at bus 652 and DGs at buses 646 and 675 still connected, the voltage levels at bus 684 exceed acceptable limits and thus the DG at bus 652 has to be taken offline. However, this causes the voltage of the motors at buses 611 and 684 to be unacceptably low during motor start which affects the power quality experienced by users at nearby buses.

TABLE 6.4 Bus voltages with all DG sources active

Bus	Pre-Start Voltage (p.u.)	During-Start Voltage (p.u.)	Post-Start Voltage (p.u.)
692	0.8926	0.5770	0.8332
675	0.8992	0.5846	0.8370
684	1.1012	0.6898	1.0286
652	1.1014	0.6905	1.0295

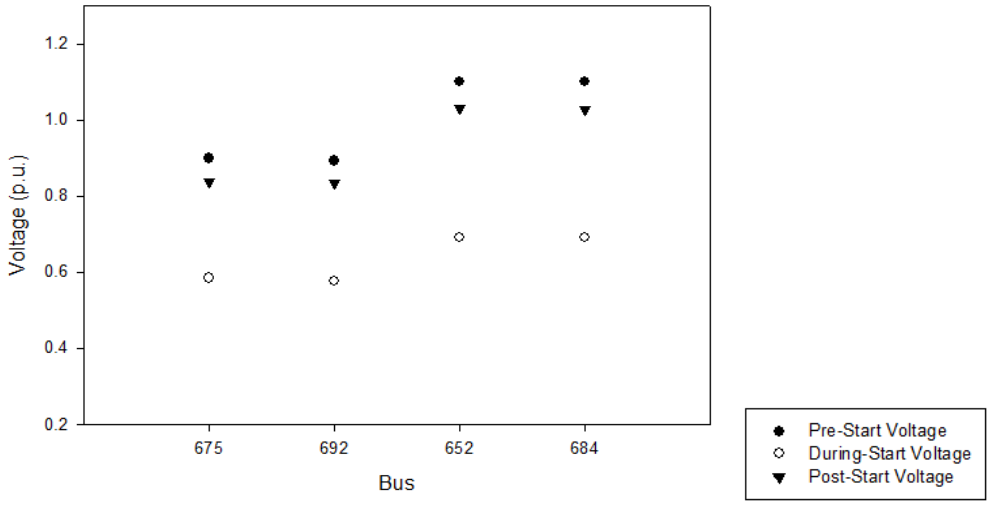

Fig. 6.5 Bus voltages with all DGs on

6.3 Reactive Power Compensation in TLPZ Microgrid

The simulations are performed on a second system that models a section of the Tampa Electric (TECO) distribution area containing the Tampa Lowry Park Zoo (TPLZ) to illustrate the application of the compensation method in a real-life system. The results of the voltage impact analysis are useful for the utility's design and planning prior to deployment of DG resources in the field by determining the optimal location and size of the DG in the distribution network. The one-line diagram of the system implemented in EDSA is shown in Fig. 6.6.

6.3.1 Weather and Load Data

The peak load demand profile for the study area is directly related to the weather conditions, particularly HVAC use in the summer as described in Chapter 2. The steady-state voltage stability simulations are performed for the scenarios where the PV source is generating power and system is experiencing high loading as a result of extensive A/C use. The weather data consisting of the average monthly solar radiation, temperature and sunlight hours for the Tampa area location of the microgrid over a six-month summer period is shown in Table 6.5. The average monthly solar radiation is normalized for the average daily sunlight hours, i.e. the near-zero solar radiation outside the sunlight hours are excluded from the average monthly solar radiation. The load data comprising the maximum real and reactive power demands for the microgrid

distribution area over the same period is shown in Table 6.6 (negative values indicate power generation).

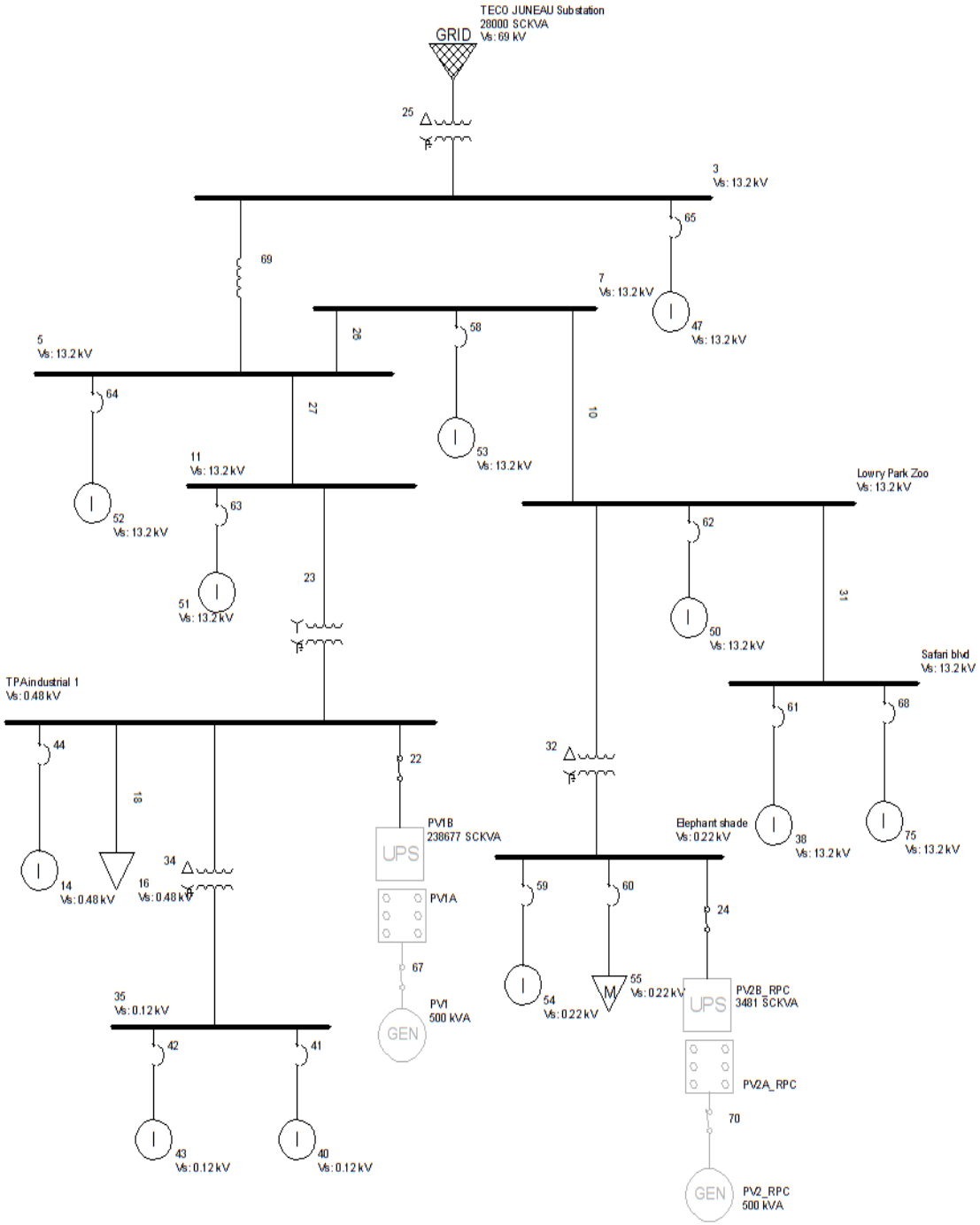

Fig. 6.6 TLPZ microgrid distribution network

Table 6.5 Available solar radiation and sunlight hours

Month	Solar rad. [W/m^2]	Temp. [°F]	Sunlight hours
April	630	65	10
May	527	72	11
June	478	74	11.5
July	450	73	11.8
August	466	75	11.6
September	464	76	11.2

TABLE 6.6 Load data for TLPZ distribution area

Bus	KW	KVAR
Lowry Park Zoo	31	18
Safari blvd	12	8
Elephant Shade	13	7
TPA industrial 1	45	32
PV1B	-15	0
PV2B_RPC	-13	-9

The annual monthly peak load demand data for the area provided by the local electric power utility shows the peak load demand occurs around April – May. During this period, the reactive power reserve in the wider power system during peak demand is minimal and it may become necessary to introduce measures such as shunt compensation or even load shedding to maintain the load equilibrium point [48, 49].

6.3.2 PV Experimental Data

The minimum and maximum monthly average PV output collected over a one-year period is used to represent the limit cases where the PV generates the least and greatest amount of energy respectively over the course of a month. The monthly average PV output for December and May represent the least and greatest amount of PV energy respectively as shown in Fig. 6.7.

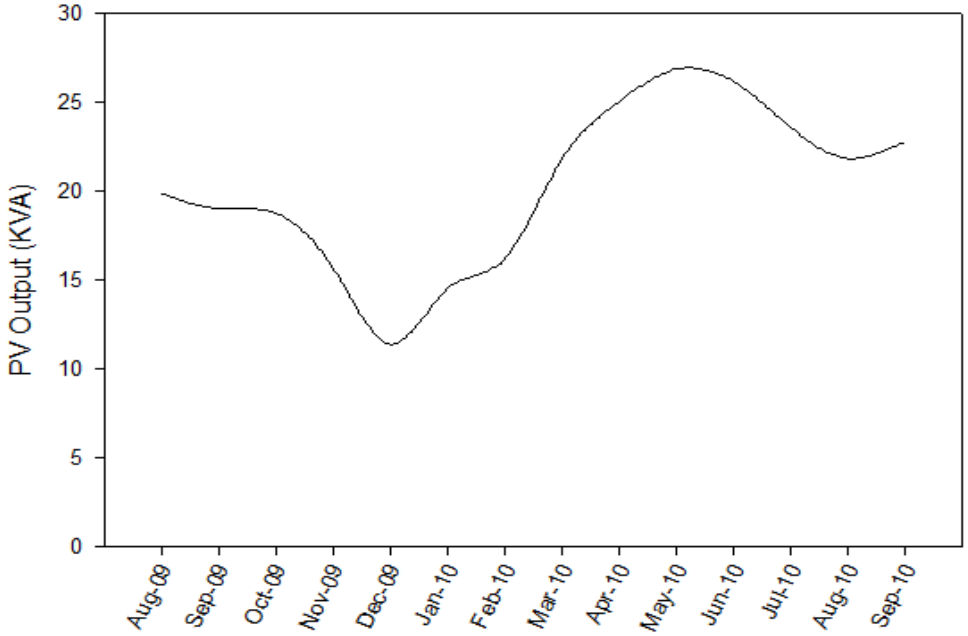

Fig. 6.7 Annual monthly minimum and maximum PV output data

The PV field data is used to schedule the PV output generation in the EDSA simulations, indicating periods when the PV source is available to support the voltage at the PCC.

6.4 Simulations and Results

The PV system is represented in EDSA with a programmable UPS model connected to a generator source. The UPS model is suitable to model the PV with DRPC since the active and reactive power generation can be scheduled to coincide with the sunlight periods when the PV is generating power. The UPS is programmed using the field data from Tables 6.5 and 6.6. The industrial power system is initially simulated with only the main grid supplying power, i.e. the PV sources are switched off. The motor start simulation scenario is repeated for large industrial motors at the some buses. The results are presented in Table 6.7 and Fig 6.8 for the pre-start, during-start, and post-start voltages. It is seen that the motors at buses 'TPA Industrial 1' and 'Elephant Shade' have unacceptably low-voltages while the motors are starting. As previously explained, this can lead to wider voltage instability if the power system experiences voltage sags or momentary interruptions while the motors are starting.

TABLE 6.7 TLPZ bus voltages with no PV source

Bus	Pre-Start Voltage (p.u)	During-Start Voltage (p.u.)	Post-Start Voltage (p.u.)
Safari Blvd	0.8993	0.5497	0.8301
Elephant Shade	0.8666	0.3673	0.7684
TPA Industrial 1	0.8593	0.3493	0.7601
Lowry Park Zoo	0.8728	0.5425	0.8120

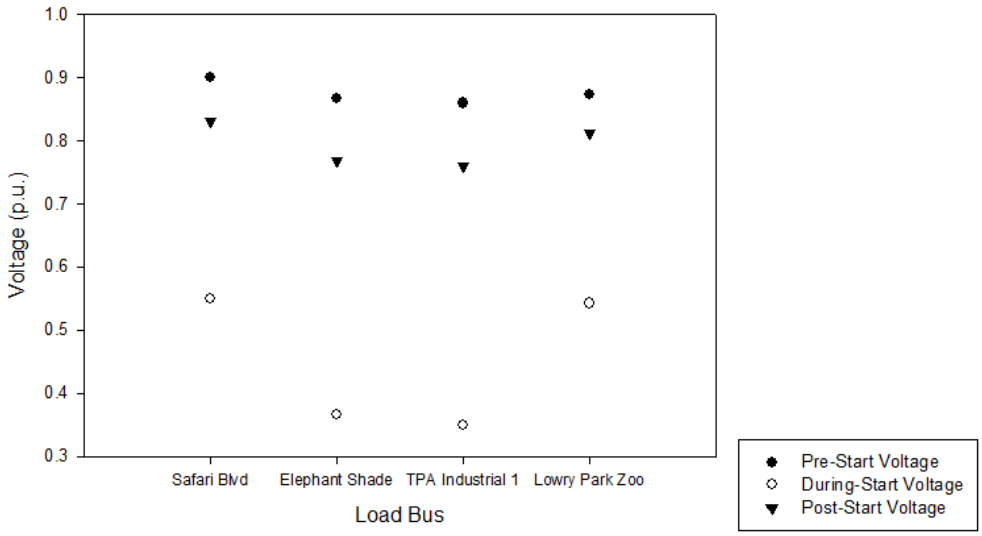

Fig. 6.8 Bus voltages with no PV source

The simulations are repeated with the PV source at bus 'Elephant Shade' switched on. The results for the voltage profile at buses 'Elephant Shade', 'Safari Blvd' and 'Lowry Park Zoo' are presented in Table 6.8. The during-start voltage improves significantly when the PV source supplies reactive power to the load buses during motor starts. The system is thus able to better withstand a voltage sag or momentary interruption without a significant slowdown in motor speed. The second PV source at bus 'TPA Industrial 1' shown in Fig. 6.3 further improves the voltage profile at nearby buses thus achieving the desired voltage correction by injecting the necessary reactive power at the load bus.

TABLE 6.8 TLPZ bus voltages with PV sources switched on

Bus	Pre-Start Voltage (p.u.)	During-Start Voltage (p.u.)	Post-Start Voltage (p.u.)
Elephant Shade	0.9202	0.6219	0.8632
Safari Blvd	0.9189	0.6199	0.8618
TPA Industrial 1	0.9194	0.6205	0.8623
Lowry Park Zoo	0.9185	0.6193	0.8613

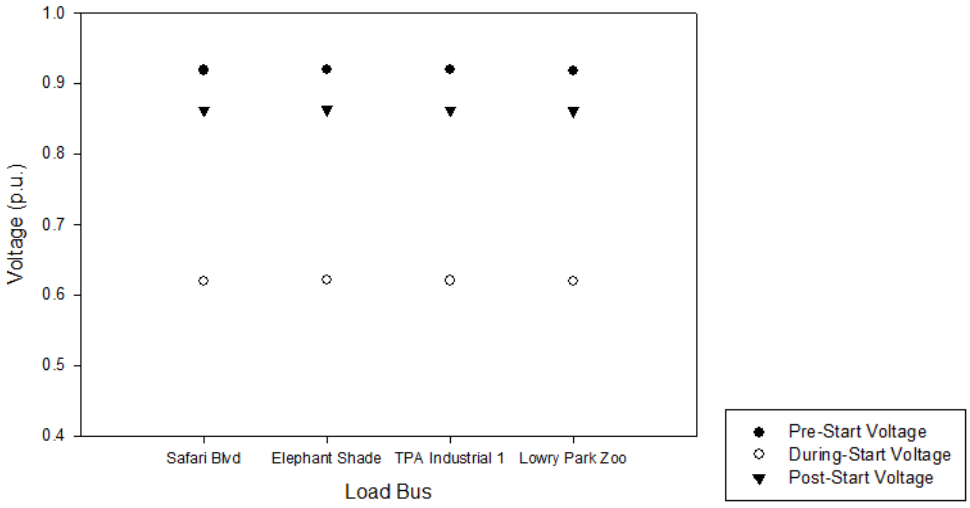

Fig. 6.9 Bus voltages with PV sources on

7. CONCLUSIONS AND FUTURE WORK

The work has been focused on the following three issues related to distribution systems with a high penetration of distributed generation: voltage stability, loadability limit influence and dynamic reactive power control. An analytical method to determine the voltage impact of DG sources at different locations in the power system based on the size of the DG and adjacent loads, as well as remedial action if necessary, is presented. The theory has been applied to a case study of the Tampa Lowry Park Zoo industrial power system.

7.1 Conclusions

The impacts of adverse power quality issues on industrial loads have been presented and different methods to classify the stability margin of an area EPS have been illustrated with some simple examples. The four existing methods for voltage sag mitigation – synchronous generator excitation control, shunt capacitor application, use of FACTS devices, and LTC transformer adjustment – have been compared, and it is found that synchronous generator excitation control is more suitable for voltage regulation of large radial transmission systems than for DG-embedded distribution

systems. A new method for voltage sag mitigation based on dynamic reactive power control of DGs has been presented. The method mitigates the transient impacts of static on/off switching of passive reactive power compensation devices. The method also improves the utilization factor of DGs that are already deployed in the power distribution system by regulating the DGs to generate both active and reactive power simultaneously. Utilities are thus able to achieve savings and minimize losses by optimally deploying more flexible DGs into the distribution system instead of peaker plants with low utilization factors. The method uses the same parameters that are used to determine the voltage stability margin of any EPS excluding the contribution from peaker plants or DGs. The maximum potential savings realizable is directly correlated with the distance from the bifurcation point of the EPS with the exclusion of the peaker plants. The impact of the method is greater on the short-term voltage stability, but for relatively small systems, it can also improve the long-term voltage stability by increasing the loadability limit of the power system.

The problem related to overvoltages at the PCC due to the presence of DGs in the power distribution system has been examined. Simple expressions to determine the potential voltage rise at the PCC as a result of DG current injection have been derived. For photovoltaic sources, the PV current limit that is necessary to hold the voltage at the PCC below a preset limit is determined based on the maximum capacity of the PV and the distance from the substation. For PV sources operating at unity power factor in industrial areas with a high concentration of induction motors, the local bus voltage rise is found to be higher than for PV sources operating with a lagging power factor. This

represents a limiting factor in the maximum capacity of the PV plant. The network and load characteristic of the power system are visualized using *PV* and *QV* curves, which make it possible to study the corresponding effects of load shedding or varying either the active power or the reactive power injection. This provides the utility a suitable platform for design and planning practices.

7.2 Further Work

The application of the reactive power control method can be developed further by including a central controller to autonomously regulate the power in multiple DG units. The use of neural networks to train large autonomous systems can be useful for the utility to balance the power flow in the power distribution system from the substation. It will be interesting to investigate the interaction between the slow acting mechanical devices of the synchronous generator and the fast acting devices of the power electronics controllers when the system has to simultaneously respond to disturbances occurring at more than one location.

REFERENCES

[1] Y. M. Atwa, E. F. El- Saadany, M. M. A. Salama, and R. Seethapathy, "Optimal renewable resources mix for distribution system energy loss minimization," *IEEE Transactions on Power Systems*, Vol. 25, No. 1, Feb 2010.

[2] C. S. Chen, M. S. Kang, J. C. Hwang, and C. W. Huang, "Synthesis of power system load profiles by class load study," *International Journal of Electrical Power and Energy Systems*, Vol. 22, No. 5, pp. 325-330, June 2000.

[3] A. J. Hoffman, "Peak demand control in commercial buildings with target peak adjustment based on load forecasting," *Proc. IEEE International Conference on Control Applications*, Vol.2, pp 1292 - 1296, 1998.

[4] S. Rahman, J. Jockell, and S. Lahour, "Analysis of the value of photovoltaics for demand side management," *IEEE Photovoltaics Specialists Conference*, Vol. 2, pp. 809 - 814, 1990.

[5] R. Wai and W. Wang, "Grid-connected photovoltaic generation systems," *IEEE Transactions on Circuits and Systems – 1: Regular Papers*, Vol. 55, No. 3, April 2008.

[6] S. J. Huang and F. S. Pai, "Design and operation of grid-connected photovoltaic system with power-factor control and active islanding detection," *Proc. IEE Gen. Trans. Distrib.,* Vol. 148, No. 3, pp. 243 – 250.

[7] G. Petrone, G. Spagnuolo, Teodorescu, M. Veerachar, M. Vitelli, "Reliability issues in photovoltaic power processing systems," *IEEE Transactions on Industrial Electronics,* Vol. 55, No. 7, July 2008.

[8] Y. Ueda, K. Kurokawa, T. Tanabe, K. Kitamura, S. Hiroyuki, "Analysis results of output power loss due to the grid voltage rise in grid-connected photovoltaic power generation systems," *IEEE Transactions on Industrial Electronics*, Vol. 55, No. 7, July 2008.

[9] A. Martinez, H. Calleja, "A simple, high quality output PV system aimed at peak demand reduction," *IEEE International Power Electronics Congress*, Mexico, 2000.

[10] J. C. Chow, R. Fischl, and H. Yan, "On the evaluation of voltage collapse criteria," *IEEE Transactions on power Systems*, Vol. 5, No. 2, May 1990.

[11] N. Hosseinzadeh, "Power system blackouts: lessons learned," *Proc. of the Australasian Universities Power Engineering Conference*, 2005.

[12] A. Domijan, "Power Con 2003- Special theme: blackout," *Proc. of the Ninth IASTED International conference*, Dec 2003.

[13] A. Domijan, F. Torres, and C. Alvarez, "Microgrids: a look into the power delivery system of the future," *Proc. of the International Conference on Power and Energy Systems*, Jan 2007.

[14] R. C. Dugan and T.E. Mc Dermott, "Operating conflicts for distributed generation on distributed systems," *Rural Electric Power Conference*, 2001.

[15] S. Conti, S. Raiti, G. Ting, and U. Vagliasindi, "Study of the impact of PV generation on voltage profile in LV distribution networks," *IEEE Power Tech Proc.*, 2001.

[16] T. S. Basso and R. DeBlasio, "1547 series of standards: Interconnection issues," *IEEE Transactions on Power Electronics*, Vol. 19, No. 5, pp. 1159 - 1162, 2004.

[17] S. Chaitusancy, A. Yokoyama, "Contribution of distributed generation to voltage regulation under stochastic attribute of renewable energy resources," *International Conference on Power System Technology*, 2006.

[18] E. Liu and J. Bebic, "Distribution system voltage performance analysis for high-penetration photovoltaics," *National Renewable Energy Laboratory Report*, Feb 2008.

[19] Y. Baghzouz, "Voltage regulation and overcurrent protection issues in distribution feeders with distributed generation – a case study," *Proc. of 38th Hawaii International Conference on System Sciences*, 2005.

[20] G. Chicco, Giaccone, F. Spertino, G. Graditi, "Experimental methods to evaluate the impact of a photovoltaic system at the point-of-common coupling in low voltage networks," *International Symposium on Power Electronics, Electrical Drives, Automation and Motion*, 2006.

[21] Y. Tachwali, H. Refai, and J. E. Fagan, "Minimizing HVAC energy consumption using a wireless sensor network," *33rd Annual Conference of the IEEE Industrial Electronics Society*, pp. 439 - 444, 2007.

[22] G. Crabtree, T. L. Jester, C. Fredric, J. Nickerson, V. Meemongokolkiat and A. Rohatgi, "Production viability of gallium doped mono-crystalline solar cells," *31st IEEE Photovoltaic Specialist Conference*, pp. 935 - 938, 2003.

[23] C. Sevik and C. Bulutay, “Gain and temporal response of AlGaN solar-blind avalanche photodiodes: An ensemble Monte Carlo analysis,” *Applied Physics Letters,* Vol. 83, No. 7, pp. 1382 - 1384, 2003.

[24] A. Omole, “Analysis, modeling and simulation of optimal power tracking of multiple-modules of paralleled solar cell systems,” *Thesis Submitted to Electrical Engineering Dept. at Florida State University,* Aug 2006.

[25] M. G. Villava, J. F. Gazoli, and E. R. Filho, “Comprehensive approach to modeling and simulation of photovoltaic arrays,” *IEEE Transactions on Power Electronics,* Vol. 25, No. 5, May 2009.

[26] T. Esram and P. L. Chapman, “Comparison of photovoltaic array maximum power point tracking techniques,” *IEEE Transactions on Energy Conversion,* Vol. 22, No. 2, pp. 435 - 449, 2007.

[27] T. Trupke, M. A. Green and P. Wurfel, “Improving solar cell efficiencies by down-conversion of high-energy photons,” *Journal of Applied Physics,* Vol. 92, No. 3, pp. 1668 - 1674, 2002.

[28] J. A. Gow and C. D. Manning, “Photovoltaic converter system suitable for use in small scale stand-alone or grid-connected applications,” *IEEE Proceedings on Electric Power Applications,* Vol. 82, No. 9, 1997.

[29] A. K. Newman and J. M. Liu, “Physical characteristics of band-gap engineered, photovoltaic detectors,” *Journal of Applied Physics,* Vol. 82, No. 9, 1997.

[30] E. Gholdston, J. Hartung, and J. Friefeld, “Current status, architecture, and future technologies for the international space station electric power system,” *IEEE Aerospace and Electronic Systems Magazine*, Vol. 11, No.2, pp. 25 – 30, 1996.

[31] B. Sahan, A. N. Vergara, N. Henze, A. Engler, and P. Zacharias, “ A single-stage PV module integrated converter based on a low-power current-source inverter,” *IEEE Transactions on Industrial Electronics,* Vol. 55, No. 7, pp. 2602 - 2609, 2008.

[32] J. M. Guerrero, J. Matas, L. Garcia de Vicuna, M. Castilla, and J. Mirer, “Decentralized control for parallel operation of distributed generation inverters using resistive output impedance,” *IEEE Transactions on Industrial Electronics,* Vol. 54, No. 2, pp. 994 - 1004, Apr 2007.

[33] P. G. Barbora, L. G. B. Rolin, E. H. Watanabe, and R. Hanitsch, “Control Strategy for grid-connected DC-AC converter with load power factor correction,” *IEEE Proc. on Gen., Trans., and Dist.,* Vol. 145, No. 5, pp. 487 - 491, 2002.

[34] N. Mohan, T. M. Undeland, and W. Robbins, *Power Electronics: Converters, Applications and Design,* Wiley & Sons, 2003.

[35] J. T. Bialasiewicz, "Renewable energy systems with photovoltaic power generators: Operation and modeling," *IEEE Transactions on Industrial Electronics*, Vol. 55, No. 7, pp. 2752 - 2758, 2008.

[36] Y. T. Tan, D. S. Krischen, and N. Jenkins, "A model of PV generation suitable for stability analysis*," IEEE Transactions on Energy Conversion*, Vol. 19, No. 4, Dec. 2004.

[37] P. Kundur, *Power System Stability and control,* McGraw-Hill Inc., New York, 1994.

[38] J. J. Grainger and W. D. Stevenson, *Power System Analysis*, McGraw-Hill Inc., New York, 1968.

[39] M. LaScala, G. Lorusso, R. Sbrizzai, M. Trovato, "A qualitative approach to the transient analysis of power systems*," IEEE Transactions on Power Systems*, Vol. 11, No. 4, pp. 1996 - 2002, 1996.

[40] J. A. Momoh, Y. V. Makarov, W. Mittelstadt, "A framework of voltage stability assessment in power system reliability analysis*," IEEE Transactions on Power Systems*, Vol. 14, No. 2, pp. 484 - 491, 1999.

[41] M. H. J. Bollen, *Understanding Power Quality Problems*, John Wiley and Sons Inc., New Jersey, 2000.

[42] K. H. La Commare and J. H. Eto, "Understanding the cost of power interruptions to US electricity customers," *Report No. LBNL-55718*, Berkeley, California: Lawrence Berkley National Laboratory, 2004.

[43] Z. Lidong and M. H. J. Bollen, "Characteristic of voltage dips (sags) in power systems," *IEEE Transactions on Power Delivery*, Vol. 15, No. 2, 2000.

[44] P. Heine and M. Lehtonen, "Voltage sag distributions caused by power system faults," *IEEE transactions on Power Systems*, Vol. 18, No. 4, pp. 1367 - 1373, 2003.

[45] Review of Florida's investor-owned electric utilities' service reliability on 2008, *Florida Public Service Commission*, Dec 2009.

[46] Z. F. Hussien, A. B. Ismail, W. C. Lee, A. M. Busrah, and M. F. M. Siam, "Voltage sag mitigation using NAS battery-based standby power supply," *International Conference on Power Electronics and Drives Systems*, Vol. 2, pp. 1317 – 1321, 2005.

[47] A. Wiszniewski, " New criteria of voltage stability margin for the purpose of load shedding," *IEEE transactions on Power Delivery*, Vol.22, No.3, pp 1367-1371, 2007

[48] A. Ghosh and D. Chatterjee, “Transient stability assessment of power systems containing series and shunt compensators,” *IEEE Transactions on Power Systems*, Vol. 22, No. 3, pp. 1210 – 1220, 2007.

[49] H. F. Wang, H. Li, and H. Chen, “Coordinated secondary voltage control to eliminate voltage violations in power system contingencies,” *IEEE Transactions on Power Systems*, Vol. 18, No. 2, pp. 588 – 595, 2003.

[50] L. Camilo, J. C. Cebrian, N. Kagan, and N. M. Matsuo, “Impact of distributed generation units on the sensitivity of customers to voltage sags,” *International Conference and Exhibition on Electricity Distribution*, pp. 1 - 4, 2005.

[51] B. Renders, K. De Gusseme, W. R. Ryckaert, K. Stockman, L. Vandevelde, M. H. J. Bollen,” Distributed generation for mitigating voltage dips in low-voltage distribution grids,” *IEEE Transactions on Power Delivery,* Vol. 23, No. 3, pp. 1581 - 1588, 2008.

[52] B. Renders, W. R. Ryckaert, K. De Gusseme, K. Stockman, and L. Vandevelde, “Improving the voltage dip immunity of converter-connected distributed generation units," Elsevier Renewable Energy, Vol. 33, No. 5, pp. 1011 - 1018, May 2008.

[53] E. G. Potamianakis and C. D. Vournas, “Short-term voltage instability: effects on synchronous and induction machines,” *IEEE Transactions on Power Systems*, Vol. 21, No. 791 – 798, 2006.

[54] T. V. Cutsem and C. Vournas, *Voltage Stability of Electric Power Systems*, Springer LLC, New York, 2008.

[55] IEEE Task Force on Excitation Limiters, “Recommended models for excitation limiting devices*,” IEEE Transactions on Energy Conversion*, 1996.

[56] M. Reza, “Stability analysis of transmission systems with high penetration of distribution generation,” *Dissertation submitted to the Delft University of Technology*, Dec 2006.

[57] U. R. Pthula, *Static and Dynamic Voltage Stability Analysis*, Lambert AG & Co., Saarbrücken, 2010.

[58] A. Sallam, M. Desouky, and H. Desouky, “Shunt capacitor effect on electrical distribution system reliability,” *IEEE Transactions on Power systems*, Vol. 43, No. 1, pp. 170 - 176, 1994.

[59] E. Zhou, “Application of static VAr compensators to increase power system damping,” *IEEE Transactions on Power Systems*, Vol. 8, No. 2, pp. 655 - 661, 1993.

[60] R. H. Liang and C. K. Cheng, " Dispatch of a main transformer ULTC and capacitors in a distribution system," *IEEE Power Engineering Review*, Vol. 21, No. 7, 2001

[61] S. Alepuz, S. Busquets-Monge, J. Bordonau, J. Gago, D. Gonzalez, J. Balcells, "Interfacing renewable energy sources to the utility grid using a three-level inverter," *IEEE Transactions on Industrial Electronics*, Vol. 53, No. 5, pp. 1504 – 1511, 2006.

[62] E. Paraskevadaki, S. Papathamassion, and M. Papadopoulos, "Benefits from DG power factor regulation in LV networks," *20th CIRED International Conference and Exhibition on Electricity Distribution* - Part 1, pp. 1 - 4, 2009.

[63] Y. A. Mohamed and E. F. El-Saadany, "A control method of grid-connected PWM voltage source inverters to mitigate fast voltage disturbances," *IEEE Transactions on Power Systems*, Vol. 24, No. 1, pp. 489 - 491, 2009.

[64] H. M. Ayres, W. Freitias, M. C. De Almedia and L. C. P. Da Silva, " Method for determining the maximum allowable penetration level of distributed generation without steady-state voltage violations," *IET Generation, Transmission and Distribution*, Vol. 4, No. 4, pp. 495 - 508, 2010

[65] L. Castaner and S. Silvestre, *Modeling Photovoltaic systems using PSpice*, Wiley Inc., Sussex, 2002.

[66] R. Benato and R. Caldon, "Distribution line carrier: analysis procedure and application to DG," *IEEE Transactions on Power Delivery*, Vol. 22, No. 1, 2007.

[67] P. Chiradeja," Benefit of distributed generation: A line loss reduction analysis," *IEEE/ PES Asia and Pacific Transmission and Distribution Conference*, 2005.

[68] P. Chiradeja and R. Ramakumar," An approach to quantify the technical benefits of distributed generation," IEEE Transactions on Energy Conversion, pp. 764 - 773, 2004.

[69] R. Brundlinger and B. Bletterie, "Unintentional islanding in distribution grids with a high penetration of inverter-based DG: Probability for islanding and protection methods," *IEEE Power Tech Conference*, 2005

[70] R. A. Walling and N. W. Miller, "Distributed generation islanding – implications on power system dynamic performance, "*IEEE Power Engineering Society Meeting*, Vol. 1, pp. 92 – 96, 2002.

[71] A. Woyte, R. Belmans, and J. Nijs, "Testing the islanding protection function of photovoltaic inverters," *IEEE Transactions on Energy Conversion*, Vol. 18, No. 1, pp. 157 – 162, Mar 2003.

[72] V. John, Y. Zhihong, and A. Kolwalkar, "Investigation of anti-islanding protection of power converter based distributed generators using frequency domain analysis," *IEEE Transactions on Power Systems*, Vol. 19, No. 5, 2004.

[73] G. Yalcinkaya, M.H.J. Bollen, and P.A. Crossley, "Characterization of voltage sags in industrial distribution systems," *IEEE Transactions on Industry Applications,* Vol. 34, No. 4, July/Aug 1998.

[74] M. H. J. Bollen, "The influence of motor reacceleration on voltage sags," *IEEE Transactions on Industrial Applications,* Vol. 31, pp. 667 – 674, July/Aug 1995.

[75] R. E. Fehr, "*Industrial Power Distribution,*" New Jersey: Prentice-Hall, 2002.

[76] S. A. M. Javadian, A. M. Nasrabadi, M. R. Haghiform, and J. Rezvantalab, "Determining fault's type and accurate location in distribution systems with DG using MLP neural networks," *International Conference on Clean Electrical Power*, pp. 284 - 289, 2009.

[77] A. Canova, L. Giaccone, F. Spertino, M. Tartaglia, "Electrical impact of photovoltaic plant in distributed network," *IEEE Transactions on Industry Applications*, Vol. 45, No. 1, Jan/Feb 2009

[78] B. H. Lee and K. Y. Lee, "Dynamic and static voltage stability enhancement of power systems," *IEEE transactions on Power Systems*, Vol. 8, No. 1, pp. 231 - 238, 1993.

[79] J. C. Das, "Effects of momentary voltage dips on the operation of induction and synchronous motors," IEEE Transactions on Industry Applications, Vol. 26, No. 4, pp. 711 – 718, 2004.

[80] A. Trzynadlowski, *Control of Induction Motors*, Academic Press, San Diego, 2001.

[81] IEEE Task Force on Load Representation for Dynamic Performance, "Standard load models for power flow and dynamic performance simulation," *IEEE transactions on Power Systems*, Vol. 10, No. 3, pp. 1302 – 1312, Aug 1995.

[82] C. W. Taylor*, Power System Voltage Stability*, McGraw-Hill, 1994.

[83] G. Tzong-Tih and R. A. Schlueter, "Identification of generic bifurcation and stability problems in power system differential- algebraic model," *IEEE Transactions on Power Systems*, pp. 1032 - 1044, 1994.

[84] R. Seydel, *Practical Bifurcation and Stability Analysis (Inter-disciplinary Applied Mathematics)*, Springer LLC, New York, 2010.

[85] I. Dobson and L. Lu, " New methods for computing a closest saddle node bifurcation and worst case load power margin for voltage collapse," *IEEE Transactions on Power Systems*, Vol. 8, No. 3, pp. 905 - 913, 1993.

[86] L. Qi, "AC system stability analysis and assessment for shipboard power systems," *A Dissertation submitted to the Electrical Engineering Dept., Texas A &M University*, Dec 2004.

[87] M. Jazaeri and M. Khatibi, "A study on Hopf bifurcations for power system stability analysis," *IEEE Electric Power Conference*, pp. 1 - 6, 2008.

[88] J. Xia and M. Xin, "Bifurcation analysis for power system voltage stability based on singular perturbation method," *International Conference on Electrical Machines and Systems*, pp. 1811 - 1814, 2007.

[89] G. C. Pyo, H. W. Kang, and S. I. Moon, "A new operation method for grid-connected PV system considering voltage regulation in distribution system," *IEEE Power and Energy Society General Meeting – Conversion and Delivery of Electrical Energy in the 21st Century*, Vol. 1, pp. 1 – 7, 2008.

[90] IEEE PES Distribution Test Feeder Working Group, "Distribution test feeders," *IEEE PES Distribution System Analysis Subcommittee*, Winter Power Meeting, 1991.

APPENDIX A: PICTURE OF LOWRY PARK ZOO PV INSTALLATION

Fig. A.1 Picture of PV installation at TLPZ